1978

Penetration resistance of soils in relation to penetrometer shape

Warakorn Mairaing
Iowa State University

INFORMATION TO USERS

This material was produced from a microfilm copy of the original document. While the most advanced technological means to photograph and reproduce this document have been used, the quality is heavily dependent upon the quality of the original submitted.

The following explanation of techniques is provided to help you understand markings or patterns which may appear on this reproduction.

1. The sign or "target" for pages apparently lacking from the document photographed is "Missing Page(s)". If it was possible to obtain the missing page(s) or section, they are spliced into the film along with adjacent pages. This may have necessitated cutting thru an image and duplicating adjacent pages to insure you complete continuity.

2. When an image on the film is obliterated with a large round black mark, it is an indication that the photographer suspected that the copy may have moved during exposure and thus cause a blurred image. You will find a good image of the page in the adjacent frame.

3. When a map, drawing or chart, etc., was part of the material being photographed the photographer followed a definite method in "sectioning" the material. It is customary to begin photoing at the upper left hand corner of a large sheet and to continue photoing from left to right in equal sections with a small overlap. If necessary, sectioning is continued again — beginning below the first row and continuing on until complete.

4. The majority of users indicate that the textual content is of greatest value, however, a somewhat higher quality reproduction could be made from "photographs" if essential to the understanding of the dissertation. Silver prints of "photographs" may be ordered at additional charge by writing the Order Department, giving the catalog number, title, author and specific pages you wish reproduced.

5. PLEASE NOTE: Some pages may have indistinct print. Filmed as received.

University Microfilms International
300 North Zeeb Road
Ann Arbor, Michigan 48106 USA
St. John's Road, Tyler's Green
High Wycombe, Bucks, England HP10 8HR

Penetration resistance of soils in relation to penetrometer shape

by

Warakorn Mairaing

A Dissertation Submitted to the

Graduate Faculty in Partial Fulfillment of

The Requirements for the Degree of

DOCTOR OF PHILOSOPHY

Department: Civil Engineering
Major: Soil Engineering

Approved:

Signature was redacted for privacy.

In Charge of Major Work

Signature was redacted for privacy.

For the Major Department

Signature was redacted for privacy.

For the Graduate College

Iowa State University

Ames, Iowa

1978

TABLE OF CONTENTS

LIST OF FIGURES

LIST OF TABLES

INTRODUCTION

Penetration testing is one of the most widely used methods to measure the comparative strength and compressibility of soils. The basic idea of the test is simply to measure the resisting force on a rod or plunger as it penetrates into soil media. The penetration test had been used for numerous soil engineering purposes such as for bearing capacity analysis, pile foundation design, pavement design, trafficability prediction, settlement analysis and even the investigation of lunar soil (35).

Although penetration testing is a simple and useful method the lack of sound theoretical analyses relative to soil cohesion and internal friction (c and ϕ) limits its versatility. Presently available analyses are either two-dimensional, i.e. for penetration of a long blade or follow along the lines of empirical correlations and dimensional analysis. Only recently have cone and wedge penetration resistances been expressed in terms of strength parameters (44).

The cone is the most popular penetrometer and shape, but spheres and flat-ended cylinder shafts are claimed to be more effective for specific uses (6, 2). Not only does the shape of the penetrometer vary, the geometry such as the apex angle of cone and the size of sphere differ from one design to another.

When a penetrometer is advanced into soil, stresses develop within the soil mass until stresses reach the soil's maximum strength,

when failure occurs. The developed failure pattern or slip-line field depends on the shape of the penetrometer as well as the soil properties. An analysis based on ideal plastic behavior is one way to predict soil penetration resistance from soil properties, but several important questions should be answered. First, does penetration induce near-plastic failure in the soil? If so, under what degree of penetration and what is the failure pattern? What influences do the shape and geometry of the penetrometer have on the failure mechanism? Are there other mechanisms involved in soil penetration? Does penetrometer shape relate to relative contributions of the soil c and ϕ to penetration resistance? If so, can the basic soil strength parameters c and ϕ be directly determined by penetration tests?

The emphasis of the present research is on shape and roughness of penetrometer. The primary objectives are as follows:

1. To develop mathematical expressions to predict the force resisting penetration, in terms of basic soil strength parameters for different shapes of penetrometers.

2. To test the theories by investigating the actual deformation mechanisms during penetration, relative to penetrometer shapes.

3. To modify the original expression as necessary or to search for better ways to predict penetration resistance, taking into account the actual mechanisms observed.

4. To investigate the possibility of directly evaluating soil strength parameters by penetration tests in the laboratory and the field.

5. To recommend penetrometer shapes and geometries that might give particular advantages for particular uses, or perhaps permit an approach to ideal plastic solutions.

The scope of the study is limited to cohesive soils and static loading conditions on the surface of the soil.

Another approach that could be used to analyze soil penetration is a limit analysis upper bound solution based on an assumed failure geometry and kinematic equilibrium (11). The present investigation follows a more classic and simpler approach for a lower bound solution based on boundary stress condition, yield criteria and static equilibrium. The upper and lower bound solutions may bracket the correct solution provided all assumptions are met, and approach one another as the assumed failure geometries are more realistic.

Finite element modeling also may be used to analyze soil penetration, but presupposes very small deformations that are not consistent with penetration tests unless the element positions are continuously modified and rearranged.

LITERATURE REVIEW

Probably the earliest soil penetration tester was the boot heel, used to investigate the terrain for the passage of horses or chariots. In 1846, Collin determined soil strength by pushing rods into the ground. He used a needle of 1.0 mm. in diameter, 1.0 kg. weight, to estimate the cohesion of different types of clay.

In 1917, the Geotechnical Commission of the Swedish State Railways standardized the method of sounding by pushing a screw point, 3.5 cm. diameter and 20.0 cm. long, with loading increments of 5, 15, 25, 50, 75 and 100 kg. (35). A pocket penetrometer developed by Godskenson having 60° cone tip, helical compression springs, scaling rod and wood handle, with total length of 12.0 cm., was used to measure resisting force of clay (17). The forces obtained from a spring scale were correlated to shearing resistance by means of experimentally derived formulas and graphs. The pocket penetrometer with similar features but having flat cylinder tip was introduced into this country in the 1950's, and is commercially available.

Later developments in deep soil penetration testing include the Dutch cone (4), which sounds the soil layers by measuring both the resisting force on the tip as a measure of soil strength, and the resisting force on a movable sleeve which follows the tip, as a measure of soil-to-steel friction.

Strength properties of surface soils have been determined for specific purposes by various kinds of penetrometers such as California

Bearing Ratio Test (CBR) which uses a flat cylindrical rod (30), the North Dakota Cone penetrometer (5), and the sphere penetrometer (6).

Numerous dynamic penetration tests have been devised and widely used. Most common is the Standard Penetration Test (ASTM Designation D 1586), which uses an open-ended sampler developed in 1927 by H. A. Mohr of the Gow Division of the Raymond Concrete Pile Co. (29). The alternative use of a solid drive cone offers the advantage of continuous drive-sounding, results usually being expressed in blows of a standard hammer dropping a standard distance to advance the sampler or cone one foot. Since these are dynamic tests, they are outside the scope of the present work.

The theory of static soil penetration testing is an adaptation of that used for metal indentation test for determining the hardness of metals, whereby a static load is applied through an indenter causing a permanent imprint on the metal surface. The amount of load and size of imprint relate to the hardness of the metal. The various shapes of indenters include spheres, cones, and pyramids.

Prandtl (31) first provided a two-dimensional solution for resisting force for a smooth wedge indenter on weightless plastic material. He also suggested the possible geometry of the failure zone, which generally consists of radial slip lines and passive wedges. Hill (20) later modified Prandtl's solution by taking into account the heaving surface of material next to the wedge, which therefore predicts a greater area of contact but a smaller pressure for the same depth of penetration.

Terzaghi (39) studied soil bearing capacity and adapted Prandtl's slip line geometry to represent general soil failure under a flat, rough footing. The semi-empirical formula for bearing capacity developed by Terzaghi also considers the effects of soil weight, surcharge of soil above the footing level, and the deviation of the actual soil properties from the theoretical model. The Terzaghi bearing capacity for strip footing can be represented by

$$q = cN_c + \gamma D_f N_q + \frac{\gamma B}{2} N_\gamma$$

where

c = cohesion

γ = unit weight of soil

D_f = depth of footing

B = footing width

N_c, N_q, N_γ = bearing capacity factors dependent only on ϕ.

The bearing capacity factors N_c and N_q later were re-evaluated by many researchers and have not substantially varied from Terzaghi's, but N_γ differs because of the difference in selecting a geometry for the soil wedge under footing. Whereas Prandtl and others assumed a base angle $45 + \phi/2$ for a growth footing, Terzaghi assumed a base angle ϕ, and Meyerhof (24) let the base angle vary to a most critical value. Meyerhof (27) also extended the Terzaghi theory of bearing capacity for wedge-shaped bases and cones and modified the bearing capacity factors. A theoretical analysis and numerical integration procedure were used.

Cheatham (9) did an analytical study of two-dimensional rock

penetration by a single bit tooth. The infinitely long strip-wedge was analyzed based on the principles of equilibrium and Coulomb's yield criterion, the rock being weightless. The analytical equations for two extremes of roughness are:

$$F = h\,\sigma_o \frac{(1 - \sin\phi)}{\cos\phi}\left[1 + \frac{\tan\beta}{\tan\phi}\,(1 + \sin\phi).e^{2\theta\tan\phi} - \frac{\tan\beta}{\tan\phi}\right]$$

for perfectly rough wedge surface, and

$$F = h\,\sigma_o \frac{\tan\beta}{\sin\phi}\left[(1 + \sin\phi)\,e^{2\beta\,\tan\phi} - (1 - \sin\phi)\right]$$

for perfectly smooth wedge surface, where

F = penetrating force on wedge per unit length

h = depth of penetration

β = half wedge angle (radian)

ϕ = angle of internal friction of rock (degree)

σ_o = unconfined compressive strength of material = $2c\,\frac{\cos\phi}{1-\sin\phi}$

$\theta = \beta + \frac{\pi}{4} + \frac{\phi\,\pi}{360}$ (radian).

The method for analyzing a dulled tip also was demonstrated.

Gnirk and Cheatham (16) then studied the effects of wedge angle and confining pressure on penetrating force. The theoretical equations are similar as above but σ_o is replaced by σ_p which is ultimate strength of the rock at a particular confining pressure p. The confining pressure and wedge angle were varied from 5000 - 15,000 psi

and 30° to 105° respectively. They found that force-displacement curves are approximately linear with confining pressure, and between the analytically predicted values for perfectly rough and smooth wedge surfaces.

Cheatham (10) presented the theoretical analysis for two-dimensional wedge penetration for intermediate friction on the wedge surface, but the solution is in a complicated form difficult to use in practice.

Butt (6) studied surface soil bearing capacity using a spherical penetration device. He applied dimensional analysis and found that the size of sphere should have no effect on the force per contact area. Experimental data for various sizes of spheres showed linear curves for clays, which agreed with the analysis. (For sands, tests were non-linear.) The relation between spherical penetration values (which is the penetration force over contact area) and C.B.R. value, plate bearing test, unconfined compressive strength, and penetrating force on wedge had strong systematic correlations. A possible use of spherical penetration devices for pavement design was also mentioned.

Richardson (34) studied spherical penetrations deeper in soil using a steel sphere to simulate stones which are pushed aside by plowing blades. He found that with increasing penetration the force rises towards a maximum limiting value. The empirical equation used to describe the resisting force is,

$$F = A + B.e^{-k(L/R)}$$

where L/R = dimensionless depth of penetration measured in sphere radii

A,B and k = adjustable parameters

Dexter and Tanner (13) extended Richardson's work by studying the effect of the speed on penetration, the surface friction and the size of the sphere. They concluded that a) a higher speed of penetration normally increases the maximum limiting force except in sandy loam, b) the roughness of sphere surface increases the maximum forces, c) the maximum force increases linearly to the square of radius.

Yong, Chen and Sylvester-Williams (45) studied the mechanics of cone and wedge penetration and the relation to soil-wheel interaction. They mentioned that the energy transferred to soil from a vehicle wheel is dissipated in two forms;

a) deformation energy losses relating to subsoil distortion and volume change and,

b) interfacial energy losses due to slip effects and high soil distortions at the contacting surface.

The experimental results on sand ($c = 0$) and clay ($\phi = 0$) show good agreement with the prediction. An increase of 10 percent in penetrating force was observed in clay for every order of increase in strain rate, but strain rate had no significant effect on sand.

Yong and Chen (44) used the technique of limit analysis to analyze cone penetration for granular and cohesive soils. The analysis showed that stress discontinuities occur in the deforming stress zone

when cone apex angles reach about 60° or more. The experimental results for cones with varying apex angle were found to match predicted values.

Butterfield and Andrawes (7) investigated the behavior of plane strain penetration of a 60° wedge in sand prepared at different porosities. Pressure cells were installed to measure stress distribution along the wedge cross section. The data showed a continuous exponential curve of force versus deformation for loose sand, and a stepped curve for dense sand. Sequential photographs were viewed as simulated stress-pairs to detect formation and jump of discrete stiplines in the dense sand, which may explain the stepped curve.

Wang and Lehnhoff (41) applied the finite element method to rock penetration by a blunt point, wedge, and cylindrical bits. The results for a blunt point were in reasonable agreement with experiment data on limestone. The program simulates plane strain and nonlinear material properties.

Baligh and Scott (1) studied the deep penetration in clay by wedges of different angles. Their theoretical analysis assumed rigid-plastic stress-strain relations of the soil, and they concluded: 1) The cutting mechanism assumed by theory was found to take place for sharp wedges, but the wider the wedge angle the more the discrepancy between theory and experiment, and 2) a blunt wedge having a half angle of 45° or more mobilized a rigid region in clay that moved with the wedge such that the deformation involved compression of soil around the wedge.

Handy, Pitt, Engle and Klockow (18) measured the penetration of 60° angle wedges that form the teeth for an in situ rock strength tester. On neat cement, siltstone and coal they found that the experimental data fell between theoretical smooth and rough equations described by Cheatham.

THEORETICAL ANALYSIS

Theoretical Background

Failure theory

The strength of geological materials; i.e., soil and rock, has been described by many failure theories. The one most widely used by engineers and used in this analysis is that of the French military engineer and scientist C. A. Coulomb, who in the 18th Century proposed that shearing strength resisting sliding along a failure plane consists of two components, cohesion and friction. For a given material the cohesion, which involves physicochemical interaction between microparticles, is normally constant, whereas the frictional resistance depends on the stress acting normal to the failure plane. The direct shear test, as shown on Figure 1, is a simple example to demonstrate Coulomb's Theory. A soil sample, Figure 1(a), subjected to a normal force N, requires a shearing force F to initiate sliding along a shear plane. The typical relations between shearing force and horizontal deformation at various values of normal forces are shown on Figure 1(b). If maximum shearing stresses (shearing forces F_1, F_2, and F_3 per unit area) are plotted versus normal stresses, there generally developes a straight line relation, Figure 1(c), which may be expressed as;

$$\tau = c + \sigma \tan \phi \qquad (1)$$

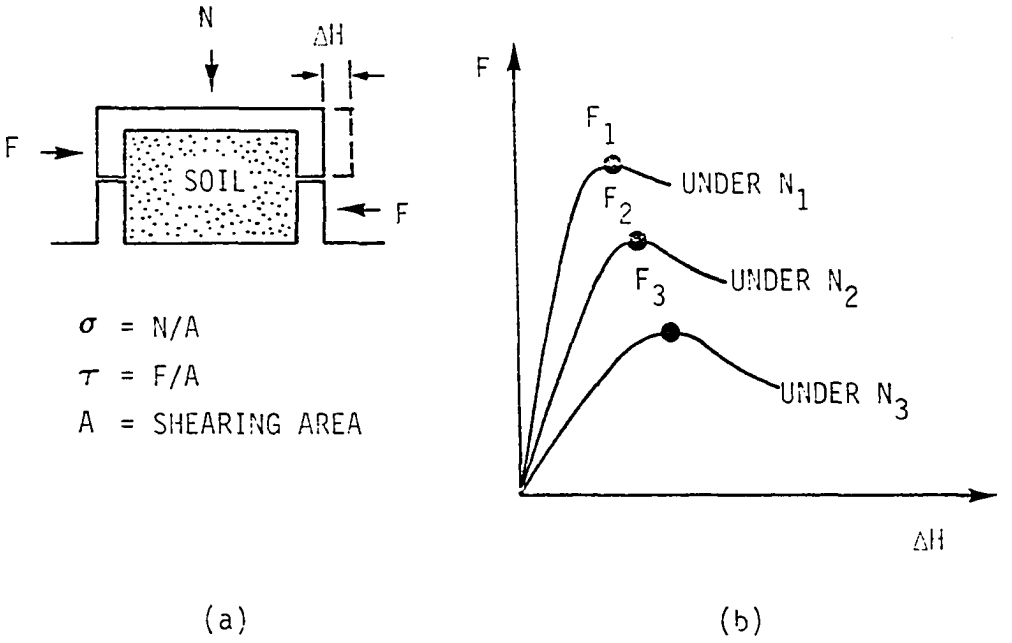

(a) (b)

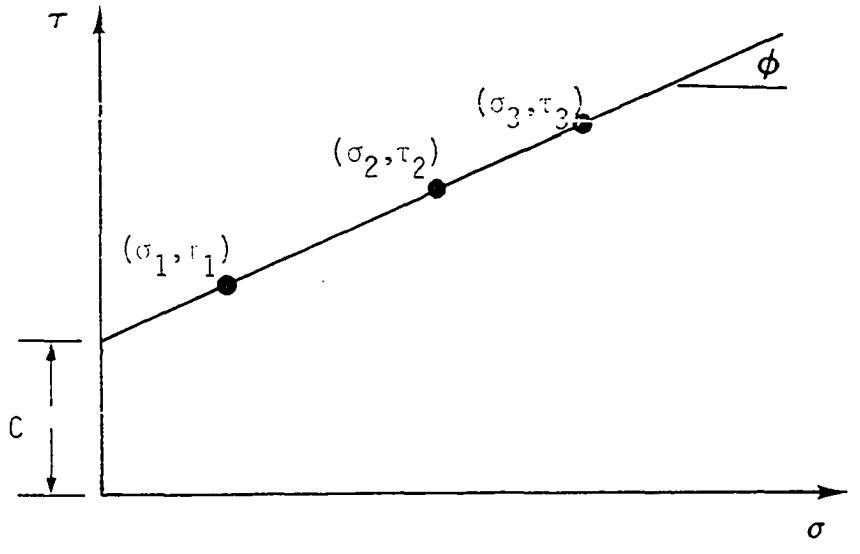

(c)

Figure 1. Soil strength and Coulomb's failure envelope

where

τ = shear strength

c = cohesion

σ = normal stress

ϕ = angle of internal friction.

Stress system and Mohr's diagram

Otto Mohr (1882) developed a very useful way to graphically represent the state of stresses acting on a material element. He showed that any known equilibrium stress system on an element can be represented by a circle on $\sigma - \tau$ coordinates, from which the stresses on any other planes become known. Mohr circles often are used to represent a failure stress condition, in which case there are important relations to Coulomb's failure envelope. These are summarized by Lambe and Whitman (22) as:

1. If the Mohr circle for a given state of stress lies entirely below the failure envelope for a soil, then the soil will be stable for that state of stress.

2. If the Mohr circle is just tangent to the envelope, then the full strength of soil has been reached on some plane through the soil. The plane is called a "failure plane" and the shear stresses on that plane are "failure shearing stresses".

3. It is not possible to have within a soil a state of stress whose Mohr circle crosses the envelope for that soil.

Thus if a soil element, Figure 2(a), is subjected to principal

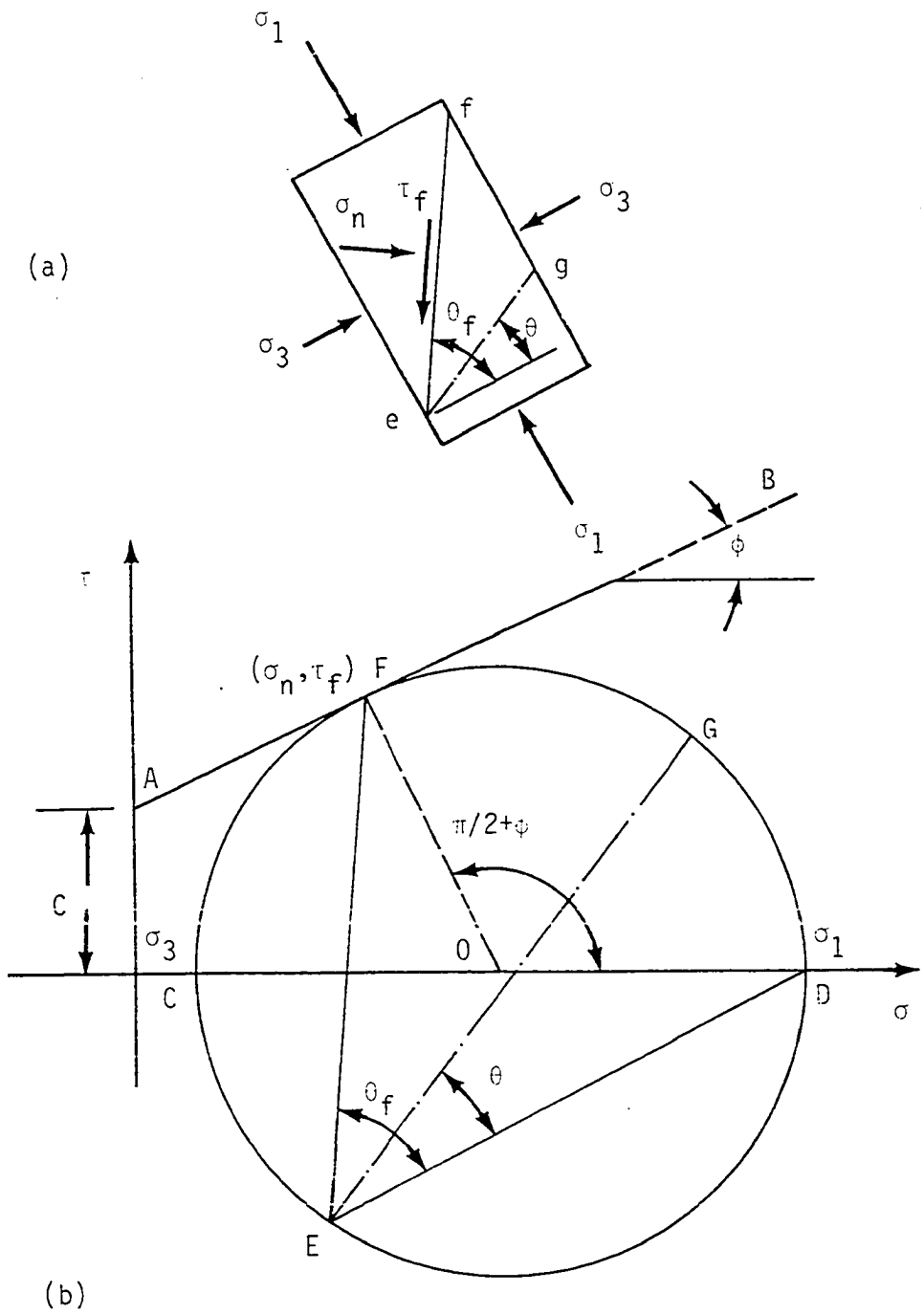

Figure 2. Stress system and Mohr's diagram

stresses σ_1 and σ_3 which initiate a failure condition, σ_1 and σ_3 can be represented by the Mohr circle of Figure 2(b). The stresses on any plane can be determined by drawing a line DE parallel to the plane on which σ_1 acts (or line CE may be drawn parallel to the plane of σ_3). Point E is called the "Origin of Planes", which has the following properties; a line from E to any point on Mohr circle is parallel to the plane on which the acting stresses are given by the coordinates of that point. For example, the coordinates of G give the values of stresses on plane e-g, Figure 2(a), which make θ angle to plane of σ_1. The same way point E, which is the intersect of Mohr circle and failure envelope, has the coordinate of failure shear stress and normal stress and line EF is parallel to failure plane e-f.

Wedge Penetration

When a wedge penetrates into a semi-infinite soil mass, plastic failure and permanent deformation occur. The slip-line field proposed by Prandtl (31) consists of a soil driving wedge adjacent to and mobilized by the penetrating wedge, then joining to a logarithmic-spiral[1],

---

[1]Logarithmic-spiral, later called log spiral: The equation of a log spiral is

$$r = r_o e^{\theta \tan \phi}$$

where r_o = initial radius

θ = rotation angle from initial radius (radians)

ϕ = angle from the normal of log spiral to the radius, which can be shown to equal the soil angle of internal friction.

and a soil passive wedge on the surface as shown on Figure 3.

The shape of the driving wedge depends on the roughness of the penetrating wedge surface. In the case of a perfectly rough surface[2], $\phi_s \geq \phi$ no driving wedge is formed because full shear strength can develop on the penetrating wedge surface, and the log spiral shear lines are extended from the wedge surface, Figure 4. For a perfectly smooth surface, $\phi_s = 0$, Figure 5, no shear stress can be transmitted from the wedge to the soil, and the penetrating wedge surface becomes a major principal plane. The driving wedge of soil is fully formed between the wedge surface and the log spiral. In the case of an intermediate rough surface, $0 < \phi_s < \phi$, Figure 6, part of the shear stress can be transmitted to adjacent soil so that the driving wedge is partially formed. The apex angle α on the driving wedge is constant regardless of values of ϕ_s, to provide continuity of slip lines from the driving wedge to the log spiral.

Intermediate rough wedge penetration

Since the size of the soil driving wedge depends on roughness of the penetrating wedge, assumptions concerning the geometry of the driving wedge, Figure 7, can be drawn as follows:

1. Angle ψ is proportional to the ratio of $\frac{\phi_s}{\phi}$, so that when $\phi_s = 0$ (perfectly smooth) then $\psi = \frac{\pi}{4} + \frac{\phi}{2}$, but when $\phi_s = \phi$ (perfectly rough) angle $\psi = 0$. Then ψ can be expressed as,

$$\psi = (1 - \frac{\phi_s}{\phi})(\frac{\pi}{4} + \frac{\phi}{2}) \qquad (2)$$

---

[2] ϕ_s = angle of friction of soil and wedge surface.

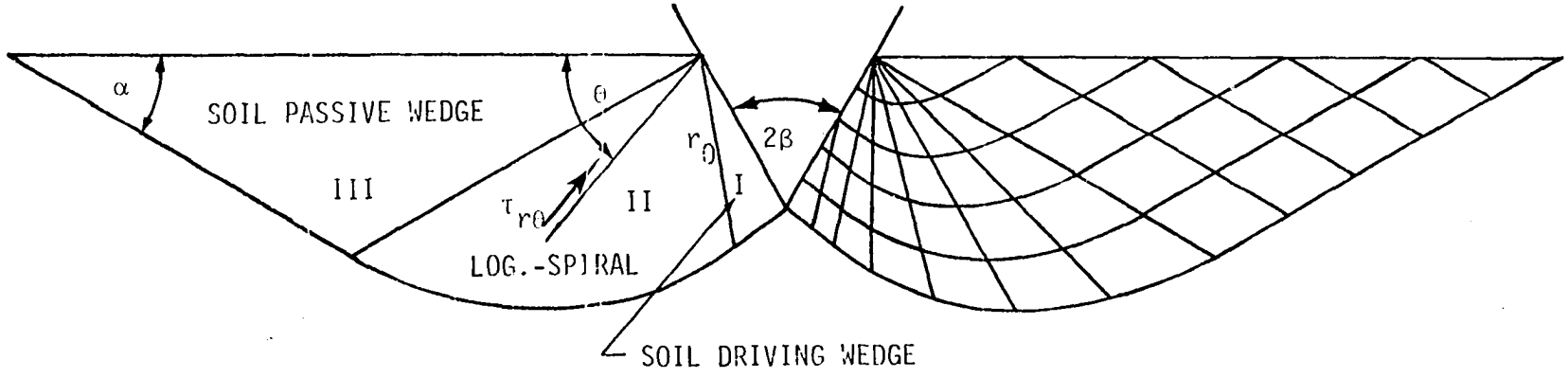

Figure 3. Prandtl's slip-line field

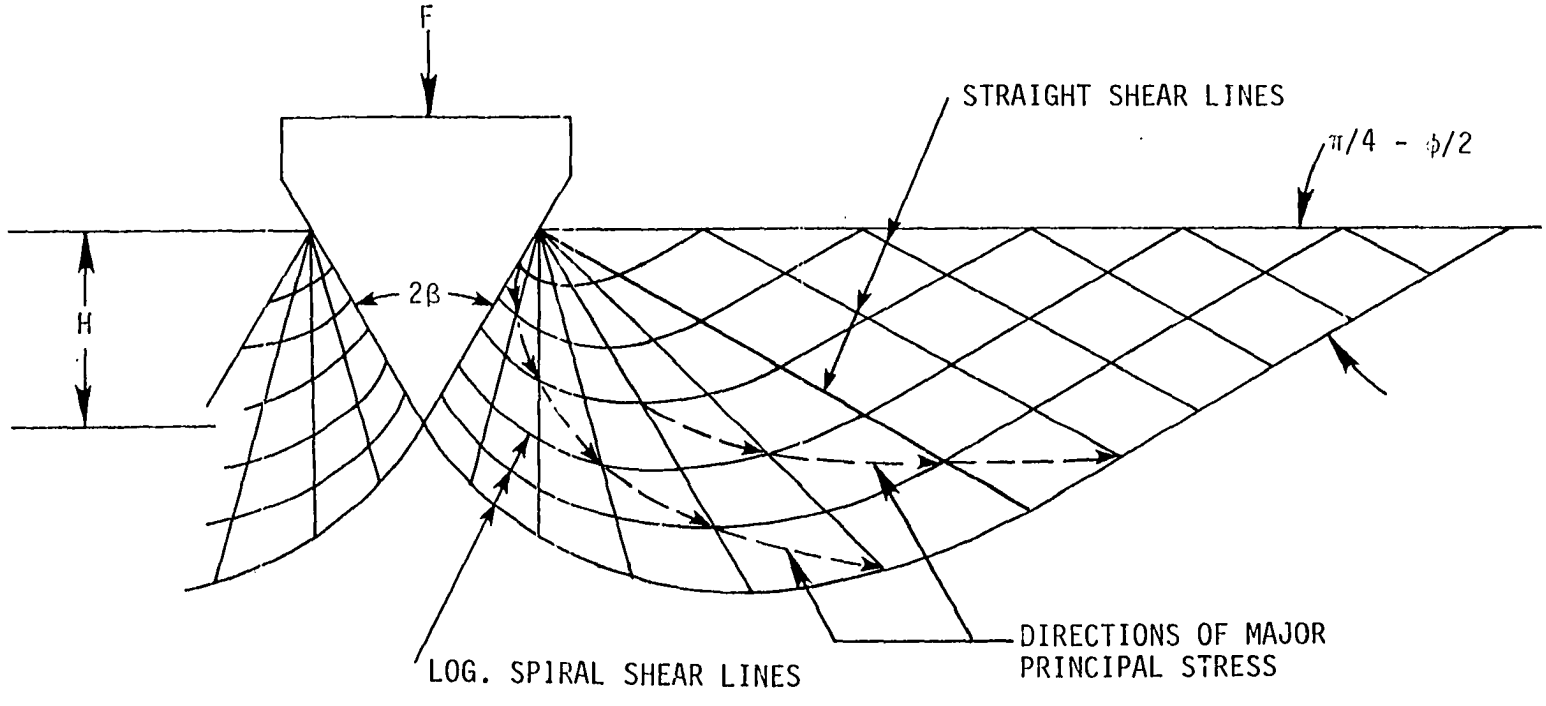

Figure 4. Slip-line for perfectly rough wedge

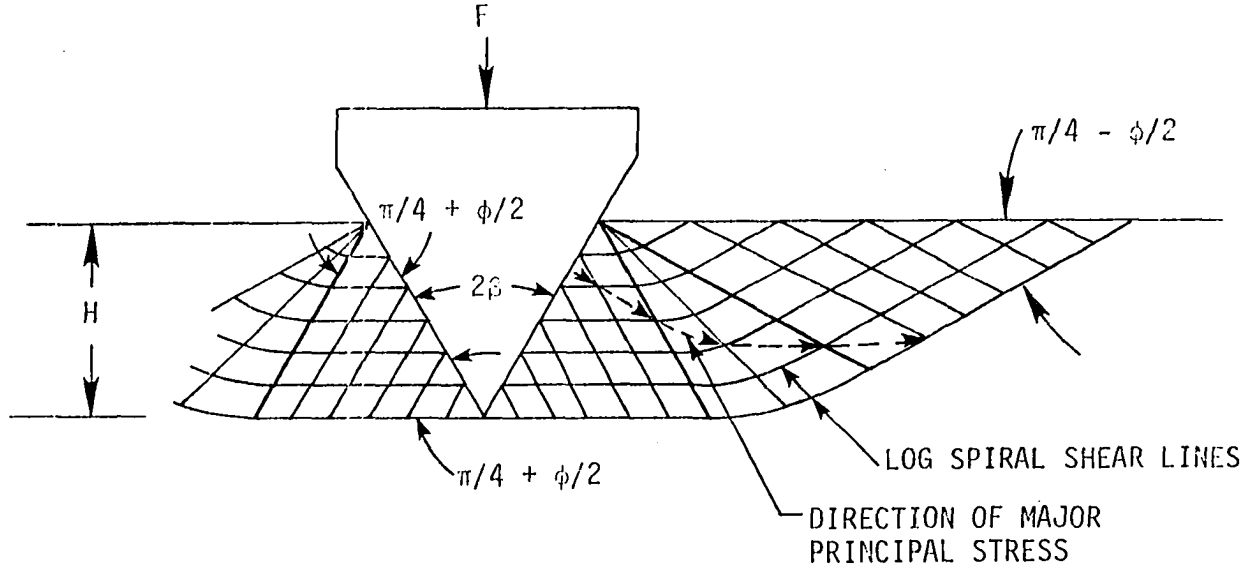

Figure 5. Slip-line for perfectly smooth wedge

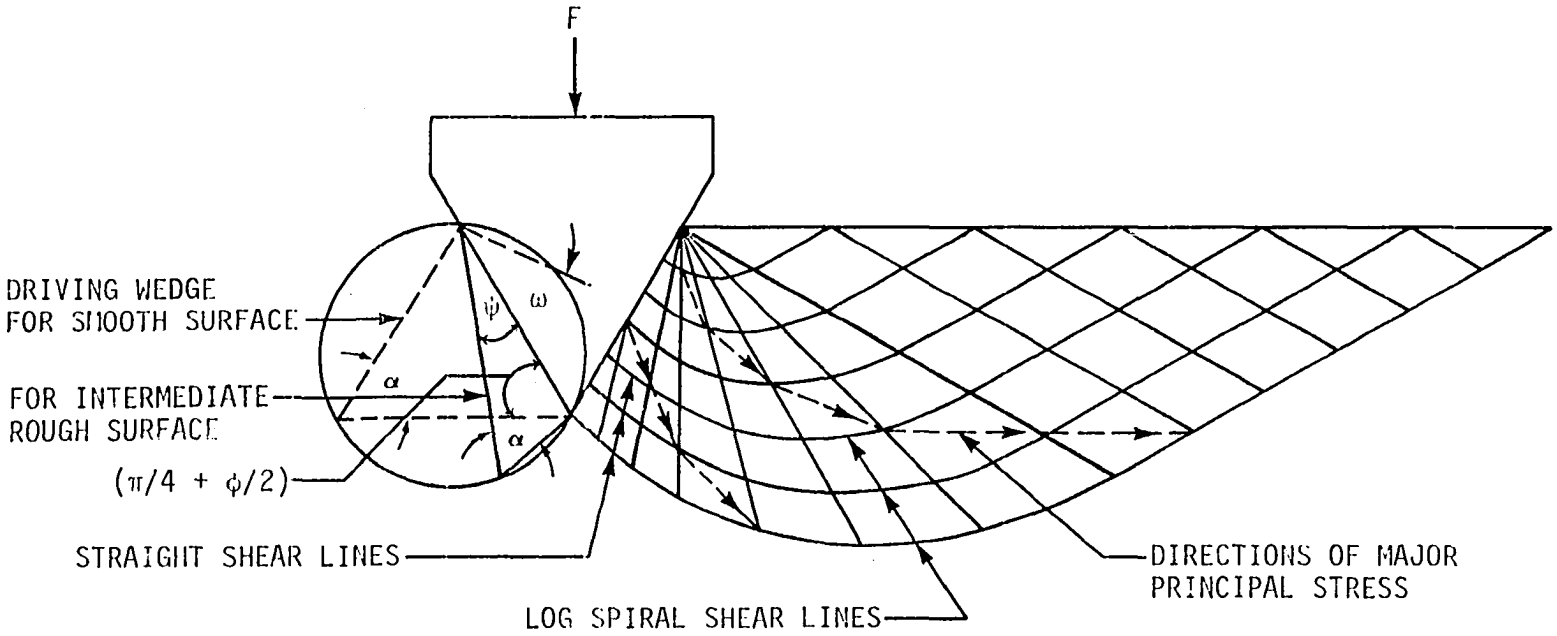

Figure 6. Slip-line for intermediate rough wedge

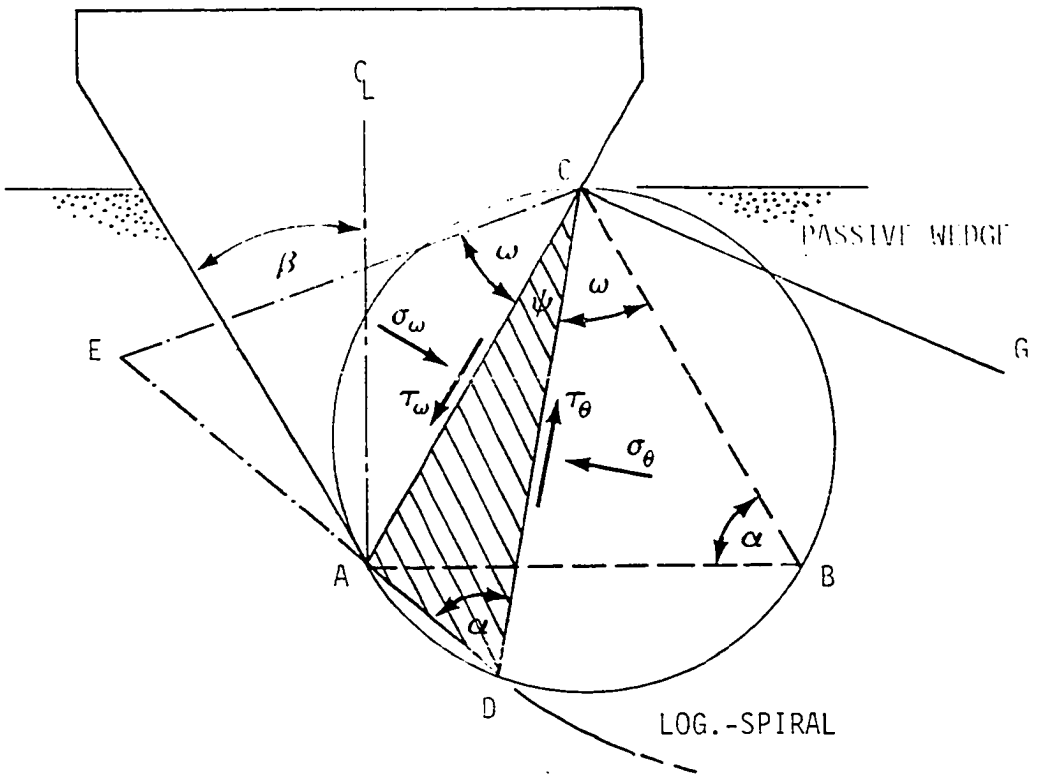

Figure 7. Geometry of soil driving wedge

2. The angle $\alpha = \frac{\pi}{2} - \phi$ = constant (3)

regardless of value of ϕ_s. Then the locus of point D is arc ADB on the circle enclosing the fully formed driving wedge ABC.

According to the geometry on Figure 7 the angle

$$\omega = \left(\frac{\pi}{4} + \frac{\phi}{2}\right) - \left(1 - \frac{\phi s}{\phi}\right)\left(\frac{\pi}{4} + \frac{\phi}{2}\right) = \frac{\phi s}{\phi}\left(\frac{\pi}{4} + \frac{\phi}{2}\right), \tag{4}$$

and angle $BCG = \pi - \left(\frac{\pi}{2} - \beta\right) - \left(\frac{\pi}{4} + \frac{\phi}{2}\right) - \left(\frac{\pi}{4} - \frac{\phi}{2}\right) = \beta.$ (5)

Cheatham (9) applied Coulomb's failure theory to the differential equations of element equilibrium in cylindrical coordinates and solved for shear stress on radial slip-line on log spiral portion. The results are

$$\tau_\theta = c\ (1 + \sin\phi)\ e^{2(\theta-\delta)\tan\phi} \tag{6}$$

where

τ_θ = shearing stress on the radial slip-line

c, ϕ = material cohesion and angle of internal friction

θ = angle from horizontal surface to the radial slip-line

δ = angle of material passive wedge = $\frac{\pi}{4} - \frac{\phi}{2}$,

and the corresponding major and minor principal stresses are

$$\sigma_1 = \frac{c}{\tan\phi}\left[\frac{(1 + \sin\phi)}{1 - \sin\phi} \cdot e^{2(\theta-\delta)\tan\phi} - 1\right] \tag{7}$$

$$\sigma_3 = \frac{c}{\tan \phi} \cdot \left[e^{2(\theta-\delta) \tan \phi} - 1 \right] . \tag{8}$$

In the case of the intermediate rough surface, it can be seen from Figure 7 that

$$(\theta - \delta) = \omega + \beta = \beta + \frac{\phi s}{\phi} \left(\frac{\pi}{4} + \frac{\phi}{2} \right) \tag{9}$$

and

$$2 (\theta - \delta) \tan\phi = 2 \left[\beta + \frac{\phi_s}{\phi} \left(\frac{\pi}{4} + \frac{\phi}{2} \right) \right] . \tan \phi . \tag{10}$$

Since σ_1 and σ_3 are known quantities, a Mohr diagram Figure 8(b) can be constructed, and stresses on the penetrating wedge surface can be solved in terms of principal stresses as;

$$\sigma_\omega = \frac{\sigma_1 + \sigma_3}{2} + \frac{\sigma_1 - \sigma_3}{2} \cos 2 \omega \tag{11}$$

$$\tau_\omega = \frac{\sigma_1 - \sigma_3}{2} \sin 2 \omega . \tag{12}$$

From Figure 8(a), the equilibrium of vertical forces gives,

$$F = 2H (\sigma_\omega . \tan \beta + \tau_\omega). \tag{13}$$

By substituting equation (11) and (12) into (13),

$$F = H (\sigma_1 + \sigma_3) . \tan\beta + (\sigma_1 - \sigma_3)(\cos 2\omega \tan\beta + \sin 2\omega). \tag{14}$$

Substitution of equation (7), (8) and (10) into (14) gives the

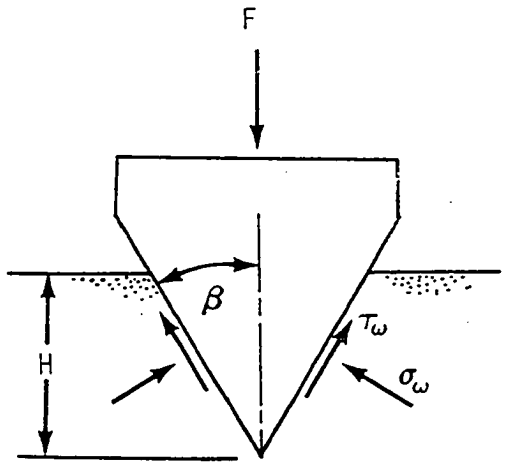

a)

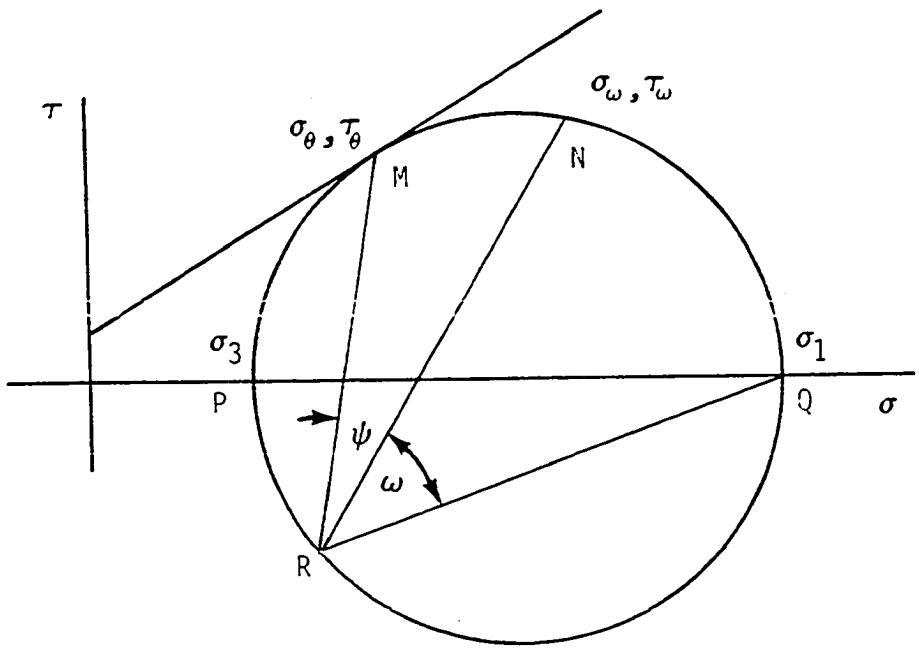

b)

Figure 8. Mohr diagram of stresses on the wedge surface

penetrating force per unit length on an intermediate rough wedge as

$$F = \frac{2c.H}{\tan\phi}\left[\frac{(\tan\beta + \sin\phi\ \cos^2\omega.\ \tan\beta + \sin\phi.\ \sin 2\omega).\ e^{B}}{1 - \sin\phi} - \tan\beta\right] \qquad (15)$$

where

F = penetrating force per unit length,

$$\omega = \frac{\phi_s}{\phi}\ \frac{\pi}{4} + \frac{\phi}{2}$$

and $B = 2\ (\beta + \omega)\ .\ \tan\phi$

Iterative adjustment

Equation (15) is strictly based on the assumptions stated in equations (2) and (3). If the assumptions are correct, point N on Figure 8(b) will be the intersect of a Mohr Circle and the friction envelope for the wedge surface. Figure 9 shows the Mohr diagram derived from c = 10 psi, $\phi = 30°$ and $\phi_s = 15°$. Point N_1 is not on the friction envelope of $\phi_s = 15°$, which must be corrected. Since σ_ω, τ_ω, σ_1, σ_3 and ω are all interrelated, no direct correlation can be made to one without affecting the other terms. An iterative method is the simplest way to obtain the correct solution by following steps:

First, the adhesion between wedge and soil is neglected ($c_s = o$).

Step 1 Assume $\omega_1 = \frac{\phi s}{\phi}\ (\frac{\pi}{4} + \frac{\phi}{2})$ as in the previous analysis; then equation (9) becomes

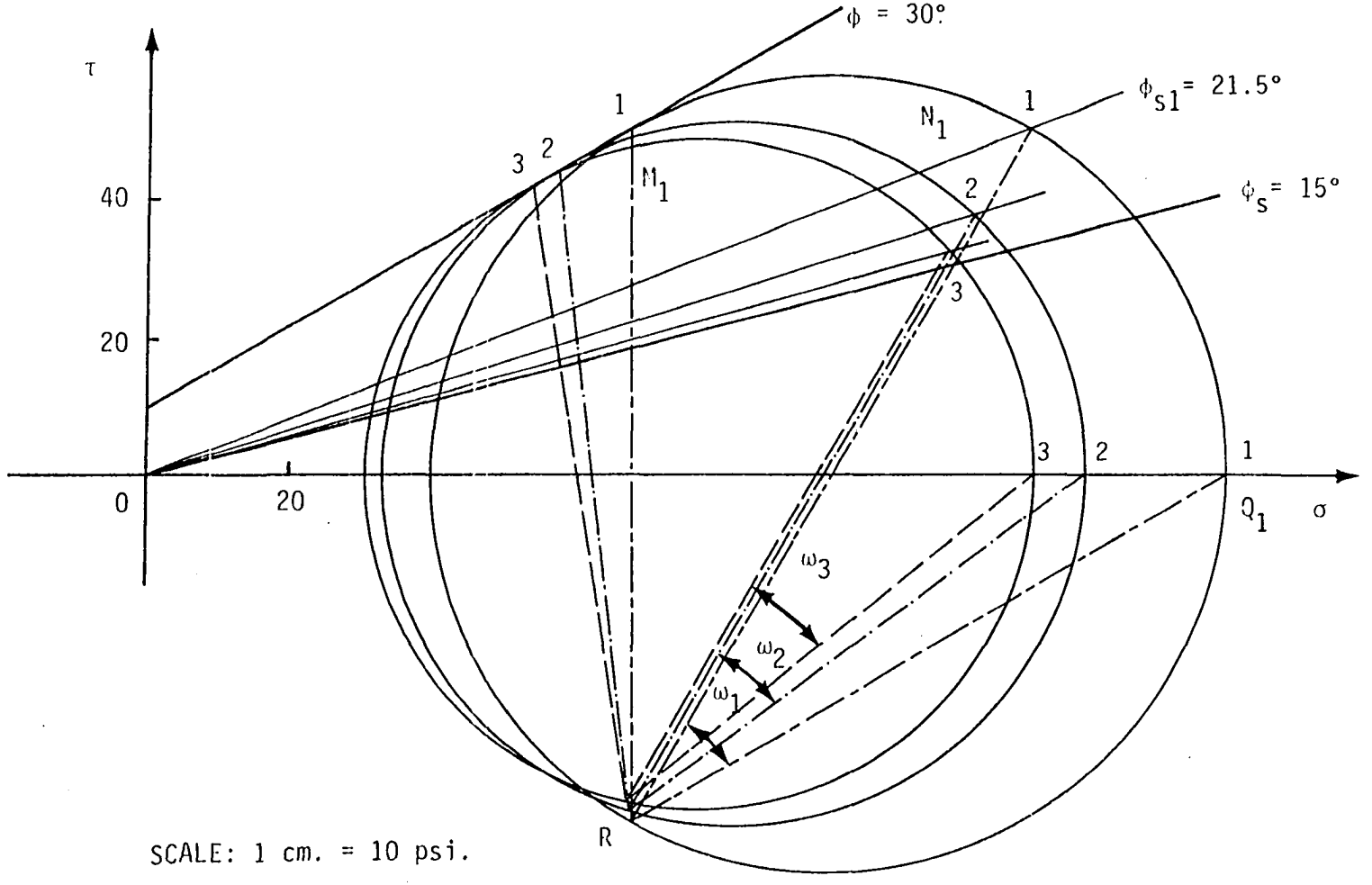

Figure 9. Mohr diagram for iterative method

$$(\theta - \delta) = \omega_1 + \beta \tag{16}$$

Step II Find σ_ω and τ_ω by a Mohr diagram as given by equations (11) and (12):

$$\sigma_{\omega 1} \frac{\sigma_1 + \sigma_2}{2} + \frac{\sigma_1 - \sigma_3}{2} \cos 2\omega_1 \tag{17}$$

$$\tau_{\omega 1} = \frac{\sigma_1 - \sigma_3}{2} \sin 2\omega_1 \tag{18}$$

Step III Check ϕ_s and adjust ω_1, from Figure 9.

$$\phi_{s1} = \tan^{-1} \frac{\tau_{\omega 1}}{\sigma_{\omega 1}} \tag{19}$$

Then replace ω_1 by

$$\omega_2 = \omega_1 - (\phi_{s1} - \phi_s) \tag{20}$$

and repeat Steps I to III until consecutive solutions for ϕ_s agree,

$$\phi_{si} \tilde{=} \phi_{s(i+1)} \tag{21}$$

Then substitute $\sigma_{\omega i}$ and $\tau_{\omega i}$ into equation (13) to obtain

$$F_I = 2H \sigma_{\omega i} (\tan \beta + \tan \phi_s) \tag{22}$$

which is the actual solution.

The iterative method provides the flexibility to vary the value

of c_s such as, when c_s = constant, then equation (19) becomes

$$\phi_{s1} = \tan^{-1} \frac{\tau_{\omega 1} - c_s}{\sigma_{\omega 1}} \tag{23}$$

Since $c_s = a \tan \phi_s$ (a = intrinsic stress, or negative intercept of the shear envelope on the σ axis), equation (19) becomes

$$\phi_{s1} = \tan^{-1} \frac{\tau_{\omega 1}}{\sigma_{\omega 1} + a} \tag{24}$$

Simplified method

By plotting on a log scale the normal stresses on a wedge surface, σ_ω, obtained from the iterative solution for any set of c, ϕ, and ϕ_s values, versus the half wedge angle, β, some interesting properties can be seen, as shown on Figure 10.

1. The plots are almost straight-line except when $\beta < 25°$.
2. The normal stresses are in direct proportion to cohesion such that when cohesion is doubled, the normal stress also is doubled provided that other parameters are the same.
3. The line for a higher ϕ has a lower slope.

These above properties allow a significant simplification. If the curves are approximated by straight lines for the whole practical range of β, then for a certain ϕ and ϕ_s, the normal stress on wedge surface can be written as

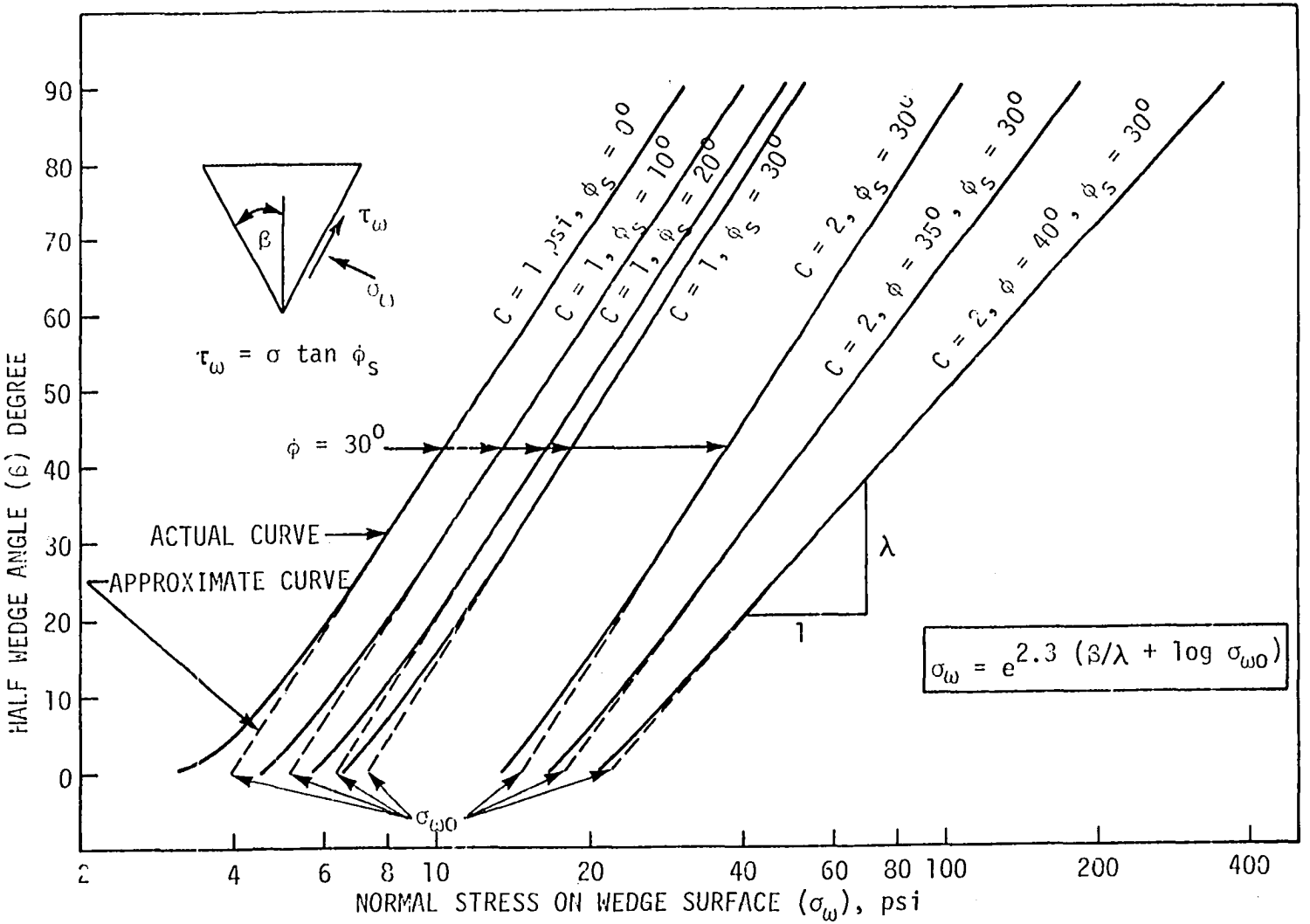

Figure 10. Relation of normal stress on wedge surface and the wedge angle

$$\sigma_{\omega} = ce^{2.3\ (\beta/\lambda + \log \sigma_{\omega o})} \tag{25}$$

where β = half wedge angle (degrees)

λ = slope of approximated straight line or change of degree per logarithmic cycle of normal stress (degrees)

$\sigma_{\omega o}$ = normal stress at $\beta = 0°$, or intercept of the approximated line on the normal stress axis (psi)

c = soil cohesion (psi)

Table 1, Figure 11 and Figure 12 show the values of λ and $\sigma_{\omega o}$. Equation (22) then becomes

$$F_s = 2cH\ (\tan \beta + \tan \phi_s)\ e^{2.3\ (\beta/\lambda + \log \sigma_{\omega o})} \tag{26}$$

The following example shows how the force/unit length can be calculated by the simplified method:

For c = 5 psi, $\phi = 30°$, $\phi_s = 20°$, $\beta = 30°$ and H = 2 in., from Table 1, $\lambda = 104.144$, $\sigma_{\omega o} = 6.432$

Then

$$F_s = 2(5)(2)(\tan 30° + \tan 20°)\ e^{2.3\left(\frac{30}{104.144} + \log 6.432\right)}$$

$$= 234 \text{ lb.}$$

A comparison of the resisting forces/unit length calculated from the first approximate, iterative, and simplified methods are shown on Figure 13. The last two are in exceptionally close agreement. The largest difference is less than 2%, when $\beta = 45°$, $\phi_s = 30°$,

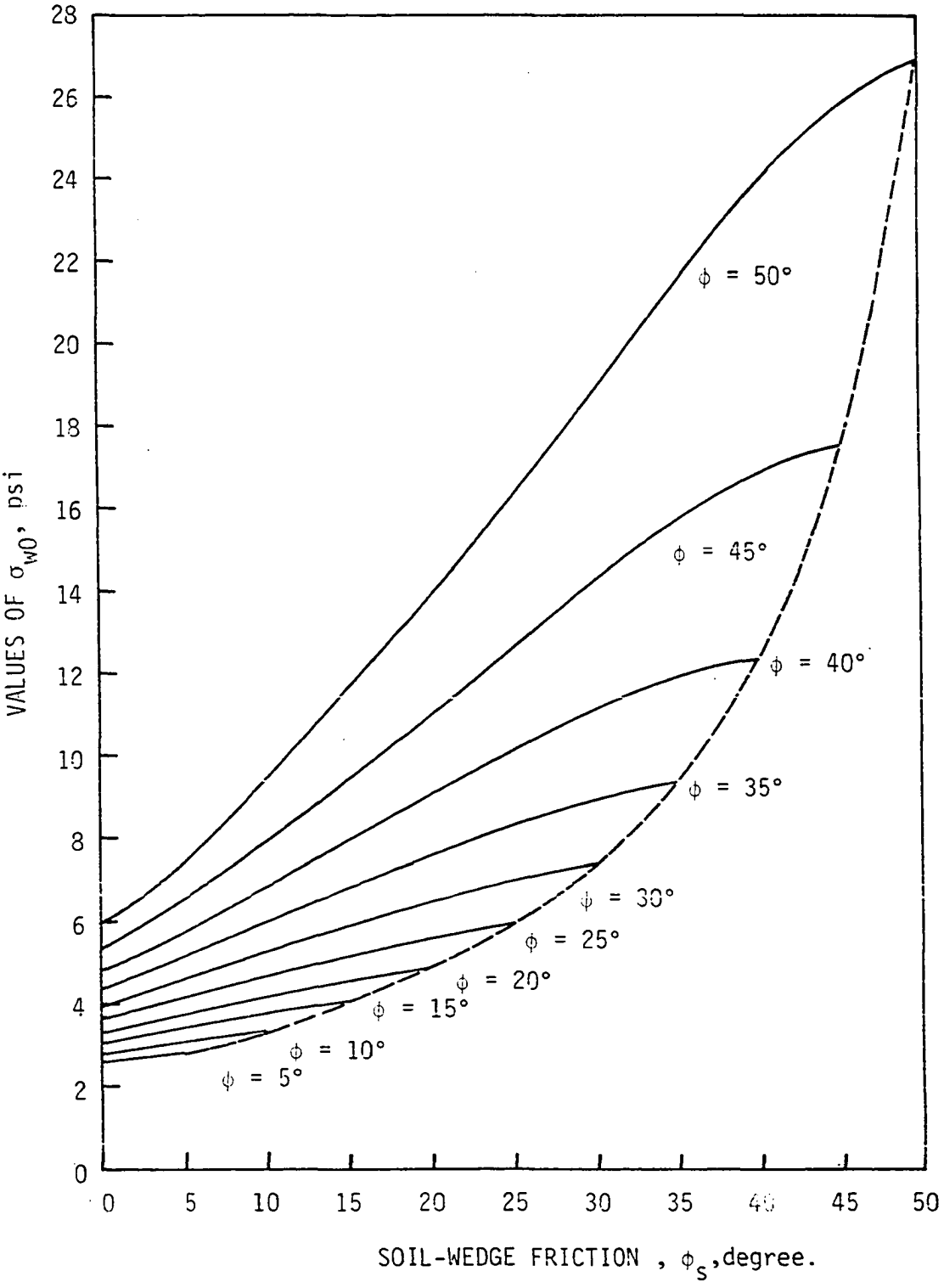

Figure 11. Values of σ_{wo}

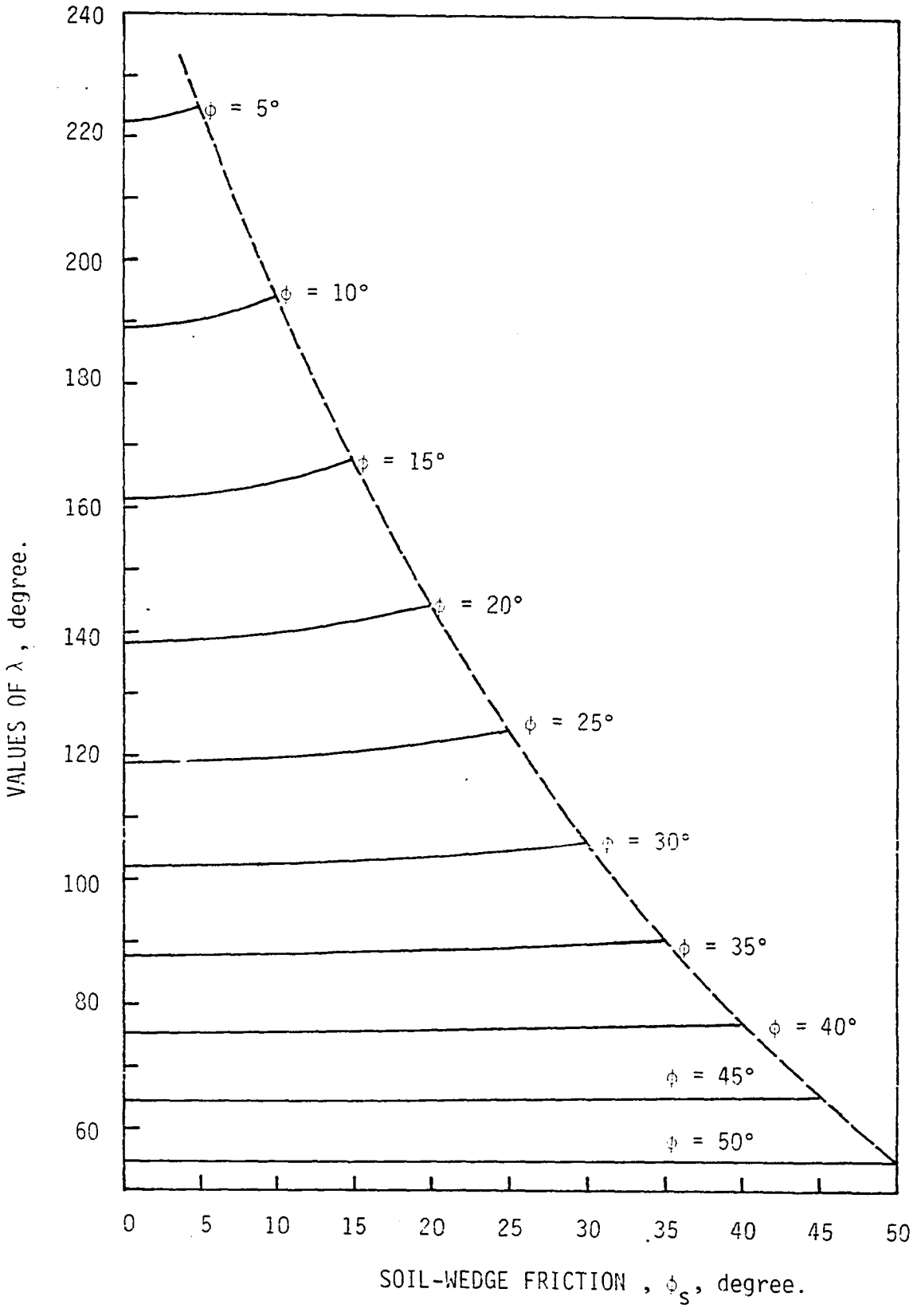

Figure 12. Values of λ

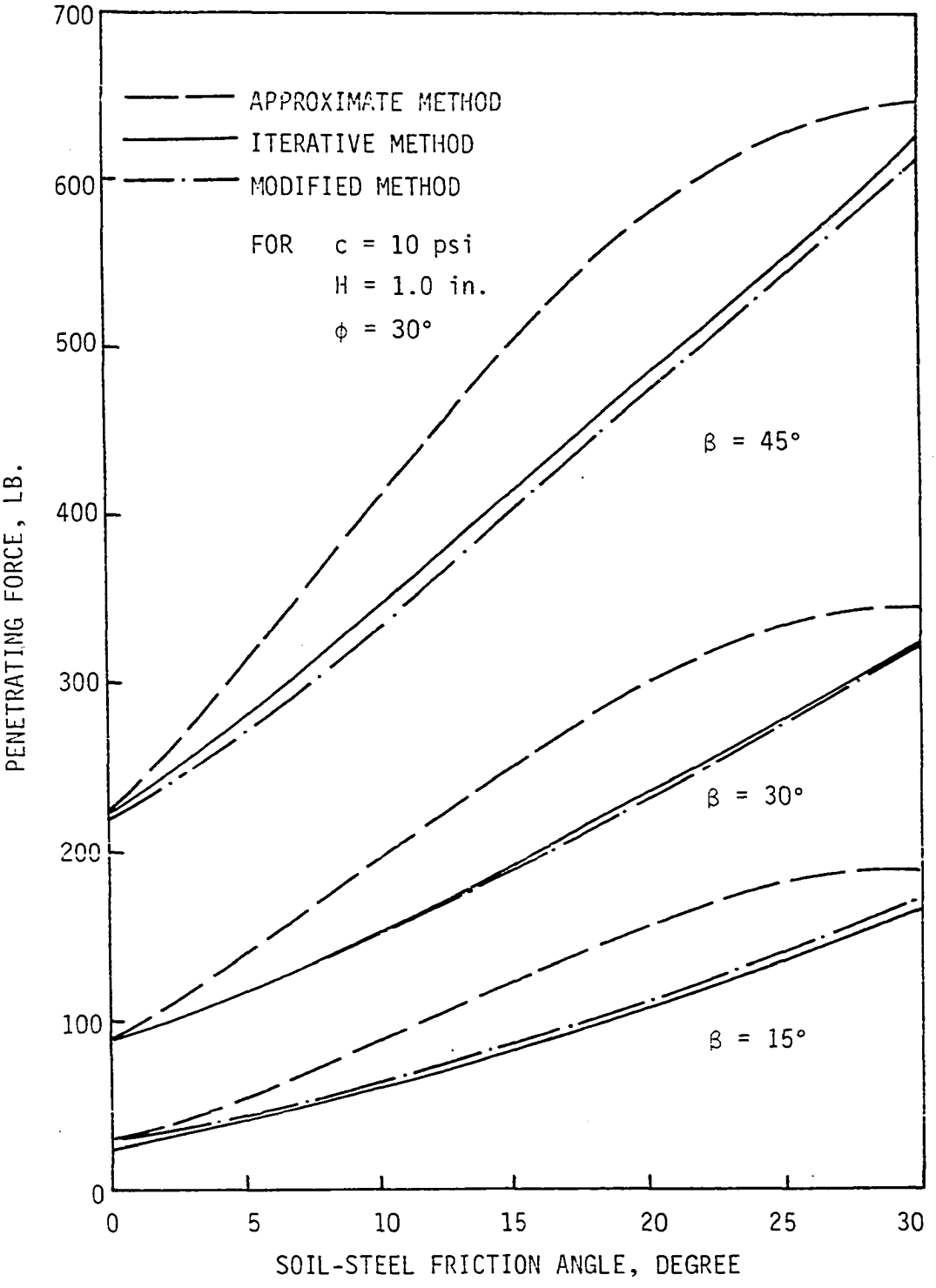

Figure 13. Comparison of approximate, iterative and modified methods

Table 1. Values of λ and $\sigma_{\omega o}$

Soil-steel friction angles	Soil friction angles				
	50°	45°	40°	35°	30°
0°	54.571[a] 5.986	64.287 5.330	75.233 4.793	87.691 4.341	102.010 3.952
5°	54.595 7.555	64.328 6.535	75.304 5.741	87.809 5.100	102.201 4.569
10°	54.649 9.395	64.427 7.897	75.477 6.773	88.099 5.207	102.682 4.628
15°	54.718 11.500	64.556 9.393	75.706 7.877	88.494 6.734	103.351 5.118
20°	54.791 13.842	64.698 10.983	75.954 8.997	88.949 7.542	104.144 6.432
25°	54.863 16.366	64.839 12.610	76.230 10.085	89.437 8.285	105.042 6.942
30°	54.930 18.984	64.978 14.196	76.500 11.075	89.958 8.906	106.144 7.322
35°	54.992 21.568	65.111 15.638	76.774 11.884	90.590 9.333	
40°	55.049 23.936	65.239 16.800	77.104 12.396		
45°	55.101 25.840	65.394 17.482			
50°	55.163 26.893				

[a]The upper value is λ (degrees) and the lower value is $\sigma_{\omega o}$ (psi).

25°	20°	15°	10°	5°
118.631	138.126	161.241	188.963	222.632
3.612	3.309	3.036	2.787	2.558
118.940	138.626	162.052	190.300	224.884
4.628	3.726	3.382	3.076	2.800
119.732	139.932	164.236	194.054	
4.628	4.139	3.713	3.335	
120.862	141.869	167.682		
5.118	4.522	4.019		
122.265	144.480			
5.556	4.847			
124.036				
5.905				

$c = 10°$, $\phi = 30°$, and H = 1".

Penetration of Long Cylinder

The simplified method for calculating wedge penetration forces allows further analysis for penetration of various shapes. A long cylinder, Figure 14, is a plane strain problem if the end effect is neglected. The area element "dA" is subjected to two stress components σ_ω and τ_ω. The amount of normal stress and shearing stress from equation (25) can be written as

$$\sigma_\omega = c.e^{2.3\left(\frac{\theta}{\lambda} + \log \sigma_{\omega o}\right)} \tag{27}$$

$$\tau = \sigma_\omega . \tan \phi_s \tag{28}$$

where θ = angle about center of cylinder, measuring from horizontal to the location of dA.

The total vertical force on area dA is

$$dF = \sigma_\omega . (\sin \theta + \cos \theta \tan \phi_s)\, dA \tag{29}$$

Substitution of equation (27) into (29) gives

$$dF = c.e^{2.3\left(\frac{\theta}{\lambda} + \log \sigma_{\omega o}\right)} [\sin \theta + \cos \theta . \tan \phi_s]\, R.d\theta \tag{30}$$

Integration of equation (30) along arc ABC gives the total penetrating force as

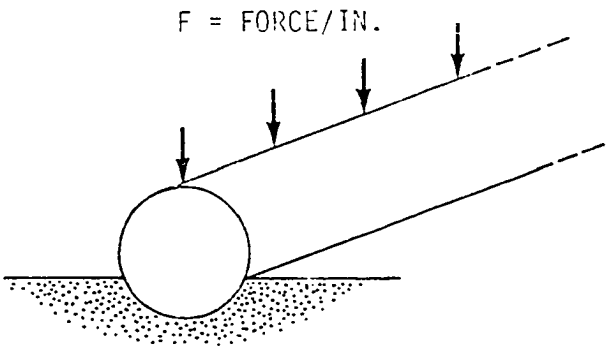

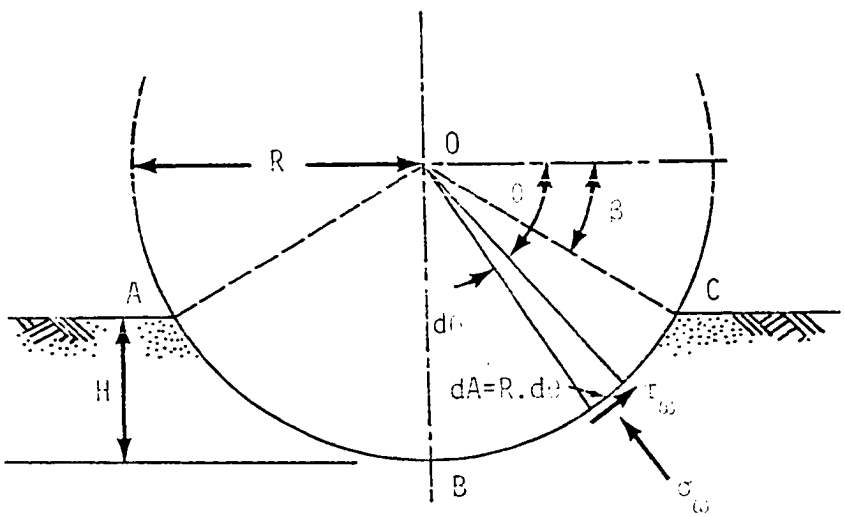

Figure 14. Long cylinder penetration

$$F = 2C.R.e^{2.3 \log \sigma_{\omega o}} \int_{\beta}^{\frac{\pi}{2}} (\sin\theta + \cos\theta . \tan \phi_s)$$

$$. e^{2.3\theta/\lambda} . d\theta \qquad (31)$$

$$F = \frac{2.C.R.e^{\kappa 1}}{(\kappa 3^2 + 1)} [(\kappa 3 + \tan \phi_s)(e^{\kappa 2} - \sin \beta)$$

$$+ \cos \beta (1 - \kappa 3 \tan \phi_s)] \qquad (32)$$

where $\kappa 1 = 2.3 \frac{\beta}{\lambda} + \log \sigma_{\omega o}$

$\kappa 2 = \frac{2.3}{\lambda} (\frac{\pi}{2} - \beta)$

$\kappa 3 = \frac{2.3}{\lambda}$

$\beta = \sin^{-1} \frac{(R-H)}{R}$

The details of derivation of equations (31) and (32) are given in APPENDIX A.

Penetration of Rounded Tip Wedge

The penetrating force on a rounded tip wedge represents the combined forces for a cylinder and a wedge. Figure 15 shows the geometry of a rounded tip wedge for which the following quantities are known:

H = actual depth of penetration

H_o = missing depth of complete wedge

β = half wedge angle

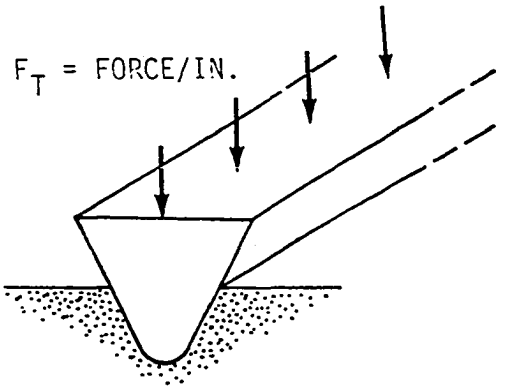

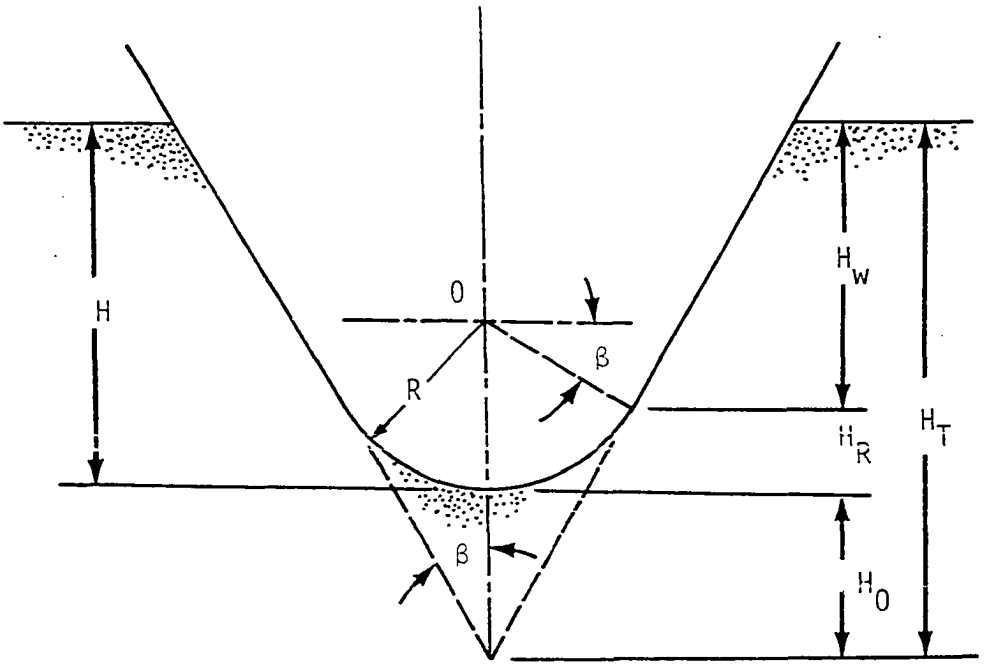

Figure 15. Rounded tip wedge penetration

The radius of rounded tip is

$$R = \frac{H_o \cdot \sin \beta}{(1-\sin \beta)} \tag{33}$$

The depth of penetration on rounded tip is

$$H_R = H_o \sin \beta \tag{34}$$

The depth of penetration of the flat portions of the wedge is

$$H_w = H - H_R = H - H_o \sin \beta \tag{35}$$

The penetrating force carried by the round tip and by the wedge is given by equations (32) and (26) respectively, the radius of the cylinder and the depth of penetration for the wedge being given by equations (33) and (35).

The total penetrating force on a rounded tip wedge is

$$F_T = F_R + F_W \tag{36}$$

where F_R = force on rounded tip (see APPENDIX B.)

F_W = force on wedge (see APPENDIX B.)

Penetration of Blunt Wedge

The penetrating force on a blunt wedge is in effect a combination of the forces on a wedge with two different angles. Figure 16 shows the geometry of blunt wedge for which the following quantities are known:

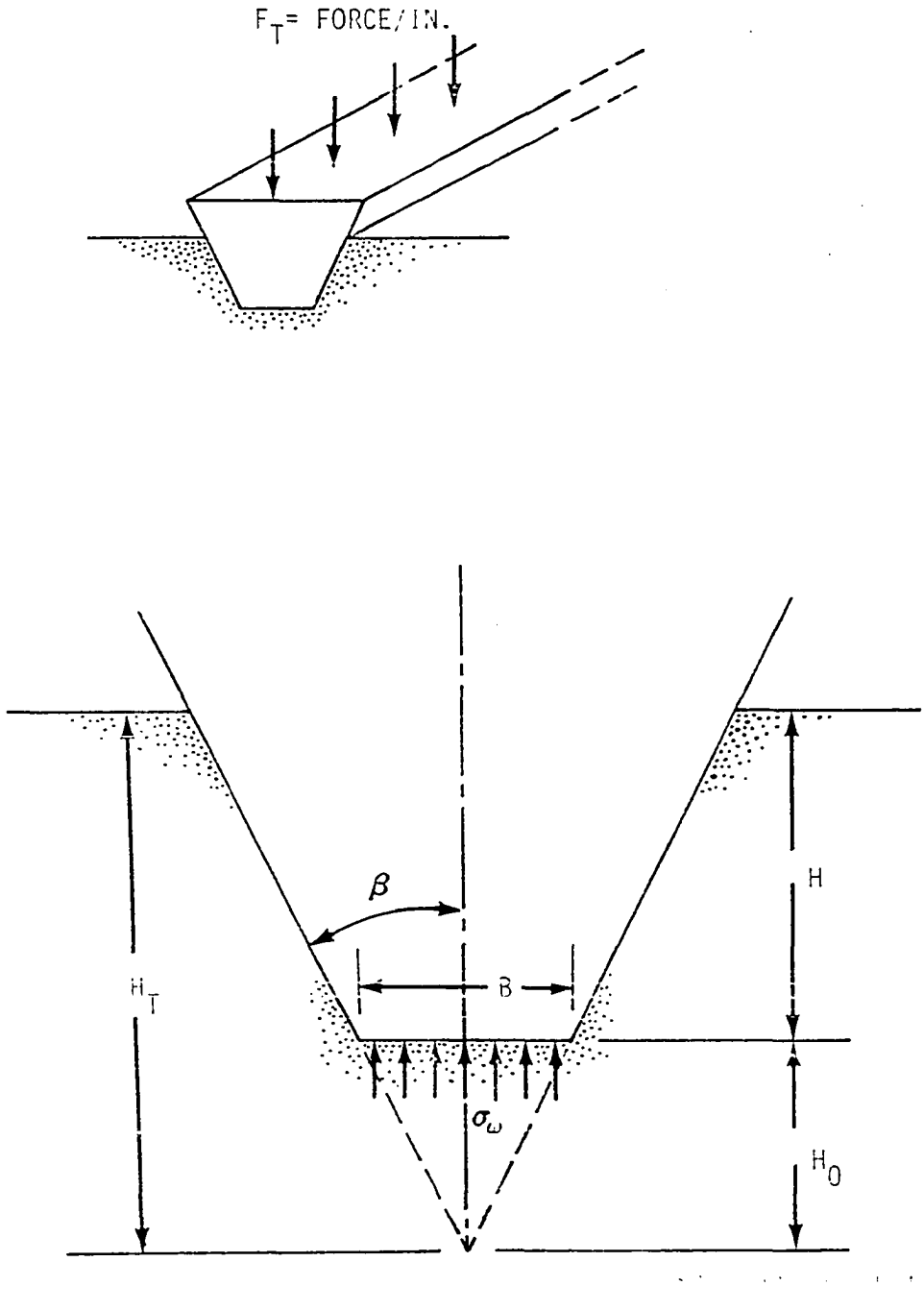

Figure 16. Blunt wedge penetration

H = actual depth of penetration

H_o = missing depth of complete wedge

β = half wedge angle

Then the width of the blunt point is given as

$$B = 2H_o \cdot \sin \beta \tag{37}$$

The force on a blunt point then equals width B times the normal stress from equation (25) when $\beta = 90°$.

The force on the wedge portion is given by equation (26) with the depth of penetration equal to H.

The total penetrating force on a blunt wedge is

$$F_T = F_B + F_W \tag{38}$$

where F_B = force on blunt point (see APPENDIX C.)

F_W = force on wedge portion (see APPENDIX C.)

Cone Penetration

The penetrating force on a cone is derived from revolving a wedge about the vertical axis as shown on Figure 17. The area element "dA" is subjected to the same normal and shearing stresses shown in equations (27) and (28). The total vertical force on area dA is

$$dF = \sigma_{zo} \cdot (\sin \beta + \cos \beta \cdot \tan \phi_s)\, dA \tag{39}$$

Substitution of equation (27) into (39) gives

$$dF = c.e^{K1} (\tan \beta + \tan \phi_s) \tan \beta.h.dh.do \tag{40}$$

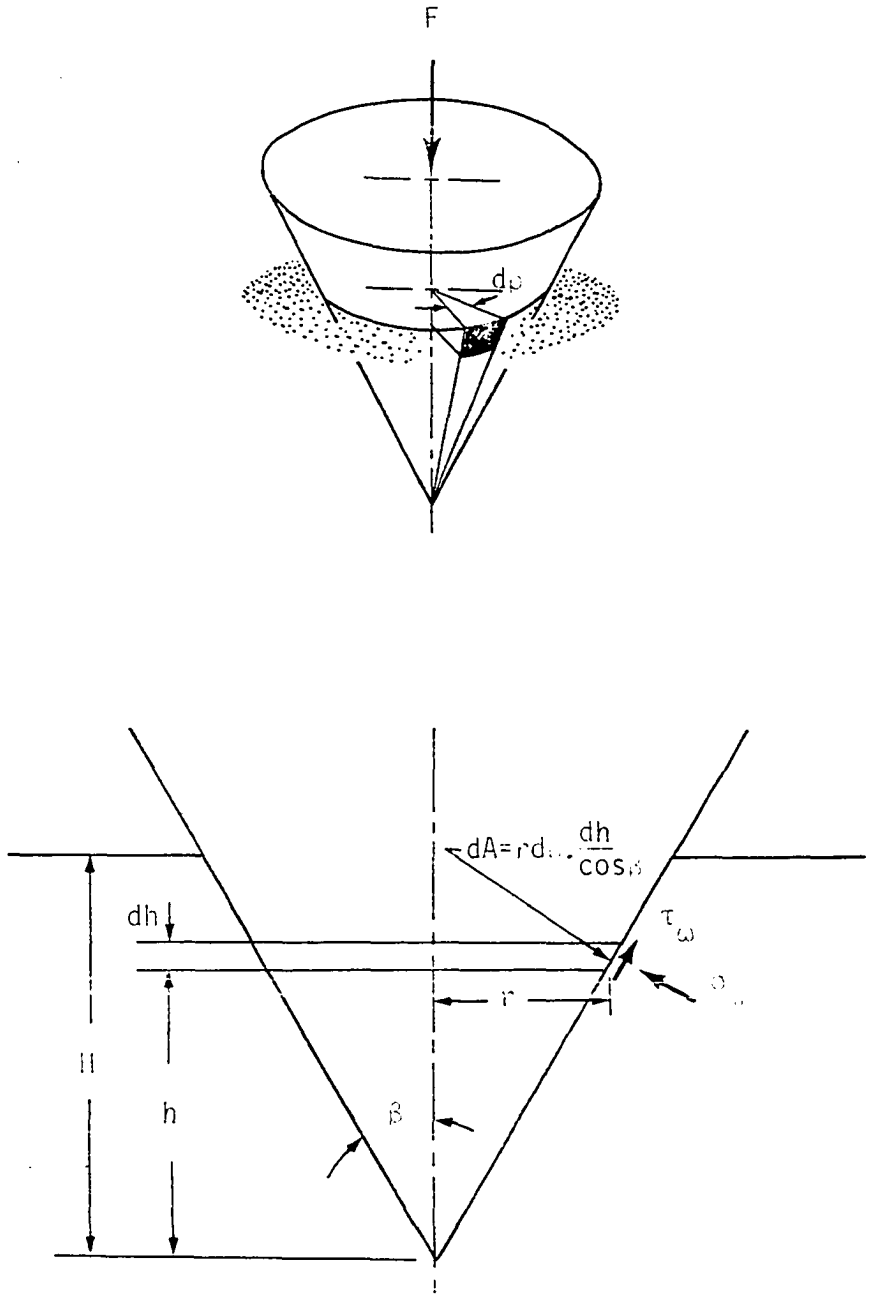

Figure 17. Cone penetration

Integration of equation (40) for the total contact surface gives a penetrating force,

$$F = c.e^{K1} (\tan \beta + \tan \phi_s) \tan \beta \int_0^{2\pi} \int_0^{H} h.dh.d\rho$$

$$F = \pi c.e^{K1} (\tan \beta + \tan \phi_s) \tan \beta.H^2 \qquad (41)$$

where $\kappa_1 = 2.3 (\beta/\lambda - \log \sigma_{\omega o})$

Sphere Penetration

Penetration of a sphere is a symmetrical case of cylinder penetration and is shown by Figure 18. The vertical force on area dA is,

$$dF = \sigma_\omega (\sin\theta + \cos\theta. \tan \phi_s) dA \qquad (42)$$

Substitution of σ_ω from equation (27) and integration over the contact surface gives the penetrating force on a sphere as

$$F = 2.c.\sigma_{\omega o}.R^2 \int_0^{2\pi} \int_\beta^{\frac{\pi}{2}} (\sin\theta. \cos\theta + \cos^2\theta. \tan \phi_s)$$

$$.e^{2.3\beta/\lambda}.d\theta.d\rho \qquad (43)$$

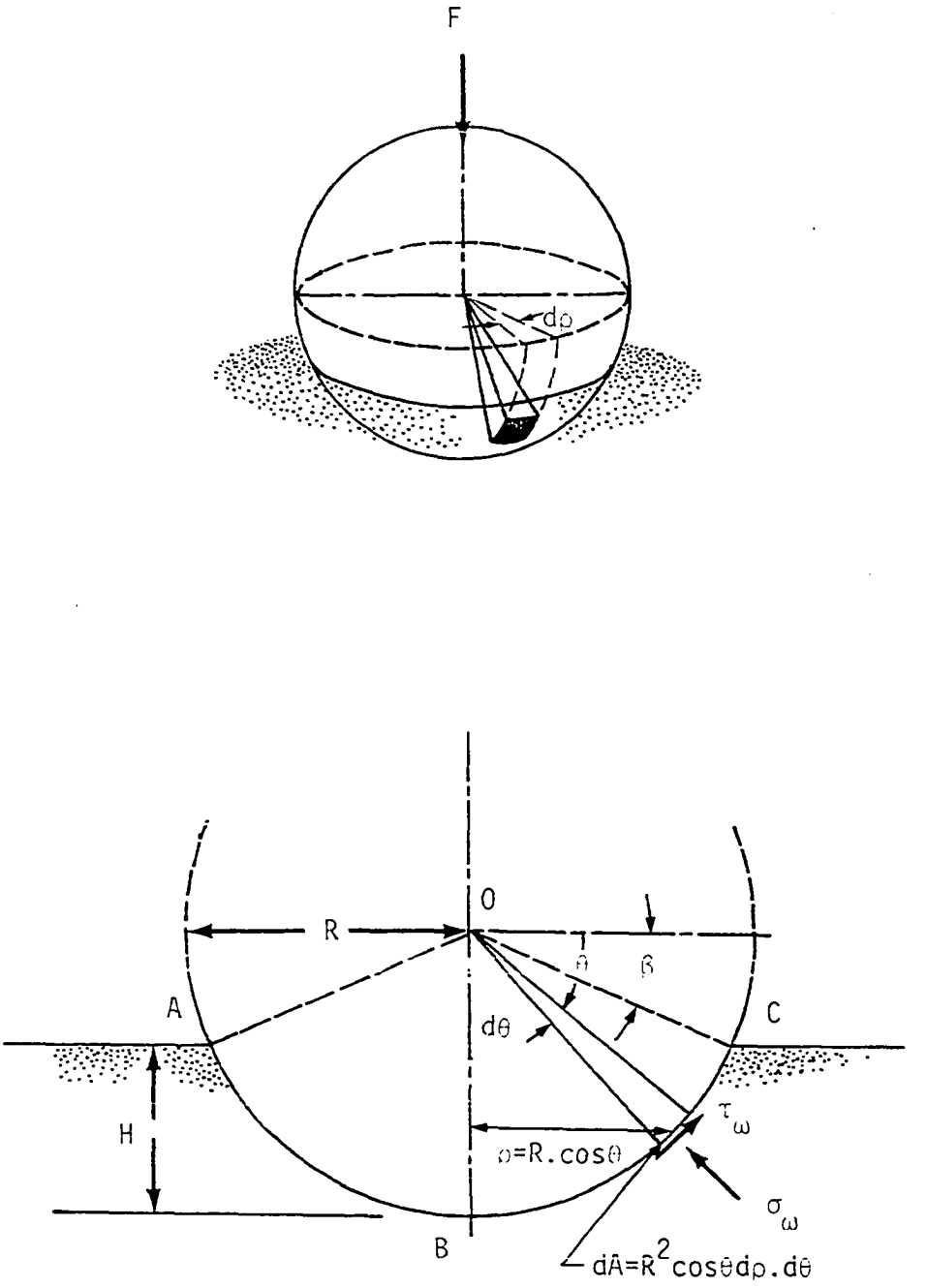

Figure 18. Sphere penetration

$$F = \frac{4\pi . c . R^2 . e^{K4}}{(K3^2 + 4)} \left[(1 + \frac{2}{K3} \tan \phi_s) e^{\frac{\pi}{2}} - \left\{ \sin 2\beta \, (\frac{K3}{2} + \tan\phi_s) - \cos 2\beta \, (1 - \frac{K3}{2} \tan \phi_s) + (\frac{K3}{2} + \frac{2}{K3}) \tan \phi_s \right\} e^{\beta} \right] \quad (44)$$

where $K3 = \frac{2.3}{\lambda}$

$K4 = 2.3 \, (\frac{1+\beta}{\lambda} + \log \sigma_{\omega o})$

$\beta = \sin^{-1} \frac{(R-H)}{R}$

The details of derivation of equation (43) are given in APPENDIX D.

Determination of Strength Parameters by Penetration

The adhesion and friction angle of a penetrometer surface to soil usually vary over the small range which may be controlled or determined from laboratory tests. Then the soil cohesion and angle of internal friction could possibly be measured in the field by two wedges or cones of different angles. The procedure would involve the following steps:

1. Two penetrating forces are measured from a set of wedges or cones at the same depth of penetration. Let us assume that a set of wedge penetrations gives the forces penetrating force F_1 and F_2 for wedges of the angles $2\beta_1$ and $2\beta_2$, respectively. Then from equation (26), the following equations can be written:

$$F_1 = 2.C.\sigma_{\omega o}.H\ (\tan \beta_1 + \tan \phi_s).e^{2.3\ \beta_1/\lambda} \tag{45}$$

$$F_2 = 2C.\sigma_{\omega o}.H.\ (\tan \beta_2 + \tan \phi_s).e^{2.3\ \beta_2/\lambda} \tag{46}$$

2. A simultaneous solution of equations (45) and (46) for λ gives

$$\lambda = \frac{2.3\ (\beta_1 - \beta_2)}{\ln \left[\dfrac{(\tan \beta_2 + \tan \phi_s).F_1}{(\tan \beta_1 + \tan \phi_s).F_2}\right]} \tag{47}$$

A similar solution for a set of cones gives

$$\lambda = \frac{2.3\ (\beta_1 - \beta_2)}{\ln \left[\dfrac{\tan \beta_2\ (\tan \beta_2 + \tan \phi_s)\ F_1}{\tan \beta_1\ (\tan \beta_1 + \tan \phi_s)\ F_2}\right]} \tag{48}$$

3. Read off ϕ from Figure 12 for a known λ and ϕ_s. Thus ϕ is determined.

4. Read off $\sigma_{\omega o}$ from Figure 11 for a known ϕ_s and ϕ.

5. Substitute values of ϕ_s, λ, and $\sigma_{\omega o}$ back in equation (45) or (46) and solve for cohesion c.

Summary of Theoretical Investigation

By manipulation of Prandtl's solutions for penetrations of rough or smooth wedges into soil the solution is extended to intermediate semi-rough or semi-smooth wedges. Trial solutions of the resulting equations presented a simple linear approximation for penetrating force as a function of wedge angle. Since this relationship is linear, it could readily be integrated to give solutions for rounded tip and blunt tip wedges and for cylinders laid on their side and pressed into soil. A second type of integration also was performed involving revolution about a vertical axis to give penetrating forces for cones and for spheres, two of the most common penetrometer shapes. A plate or flat-ended rod penetrometer represents a special case of a cone with an apical angle of 180°. Finally, it is shown that if the theory is correct, penetration measurements with two different wedge or cone angles should separably define the soil cohesion and internal friction angle. Actual utilization of this method to measure soil c and ϕ may be impractical because of lack of sensitivity of the method, but the analysis, if valid, is valuable for optimizing the penetrometer shape and surface roughness to emphasize the contribution of one or the other.

Finally, it must be emphasized that the several solutions proposed can be expected to describe reality only as the assumed failure conditions approximate reality. The Mohr-Coulomb theories utilized

in the derivations have a long history of trial and almost universal acceptance, but the failure geometries of Figure 3 through 6 are approximations based on weightless soil and ideal plastic behavior. Nevertheless comparative calculations for other more-or-less similar geometries and other methods of analysis reported in the literature usually give differences of $\pm$ 20 percent or less. When real soil properties are entered the problem becomes indeterminant, and solutions as by physical or finite element modeling became case-specific. Thus a prediction of the order of $\pm$ 20 percent should be acceptable.

Perhaps the most serious new problem raised is use of the integration procedures, which necessarily involves an assumption that at failure the slip line field of Figure 6 distorts to follow around the penetrometer surface at a uniform angle ψ, regardless of the shape of the penetrometer, and that penetrometer shape and hence confining stresses developed in soil under the contact do not influence soil behavior, which is assumed to be ideally plastic. We may anticipate that the derived relationships will decrease in accuracy as confining stresses increase and the soil becomes compressible, i.e. for blunt wedges or cones or rods, or for the area under the central axis of a sphere or side-penetrating cylinder.

EXPERIMENTAL INVESTIGATION

Displacement Model Test

The previous theoretical analyses are necessarily based on several assumptions;

1. The failure condition of the material obeys Coulomb's theory,
2. The failure boundary follows Prandtl's slip-line pattern,
3. The material is rigid-plastic, with no significant deformation before failure.

The validity of the theoretical expression thus depends on how closely the assumptions represent the actual behavior. The first assumption had been practically demonstrated, accepted, and widely used in soil and rock engineering fields for many years. The last two assumptions will be tested by displacement models in which the actual soil deformations will be recorded continuously under penetrating loads.

For two dimensional viewing, rectangular prism soil samples held in plane strain were penetrated by 30°, 60°, and 90° wedges, and 1" and 2" diameter cylinders. The penetrometers are shown on Figure 19a. Even though cone and sphere penetrations are 3-dimensional problems, they also are axisymmetrical cases of wedge and cylinder penetration. The deformation patterns on the plane through the centerlines of a cone or a sphere are expected to be the same as those of a wedge or a cylinder, respectively.

Materials

The displacement model tests were conducted on the following materials:

1. remolded modeling clay, designated MC,
2. compacted Shelby soil, designated SB,
3. compacted Ottawa sand, designated OS,
4. compacted Monona soil, designated MN.

The modeling clay is commercial sculpture material, highly plastic and oil saturated. The unconfined compressive strength reported by Baligh and Scott (2) is between 1.0 - 1.25 kg/cm^2 at 5% strain. The strength parameters c and ϕ from triaxial tests reported by Fox, Barkdale, Handy and Trott (14) are 3 psi and 4°, respectively. The predominant clay mineral is kaolinite.

The Shelby soil is a silty clay developed in oxidized and leached Kansan till. Monona soil is a silty clay loam developed in calcareous loess. A summary of physical properties of Shelby and Monona soils is presented in Table 2.

Apparatus

The equipment set-up is shown in Figure 19b, and consists of a displacement box and loading frame. The box is made of 1 in. thick aluminum, with a 1 in. thick plexiglass front and is bolted together for ready disassembly for sample preparation. The inside dimensions of the box are 3 x 3 x 11.25 in. The loading machine is a Fairbanks-Morse platform dead load scale with an accuracy of $\pm$ .5 lb.

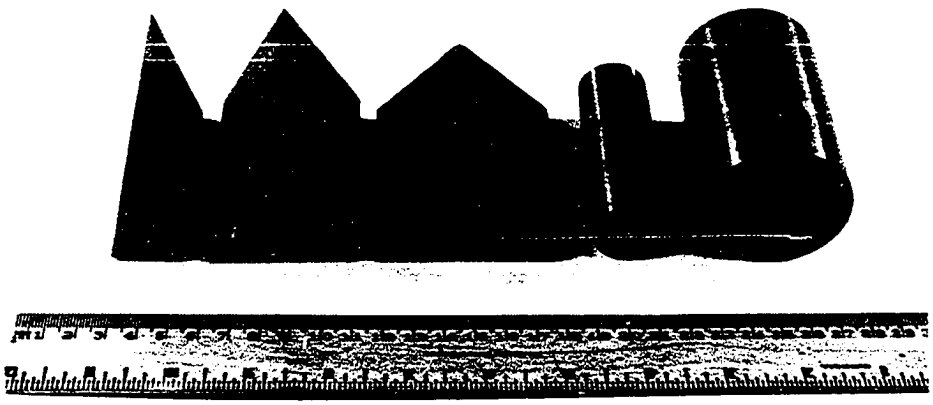

a)

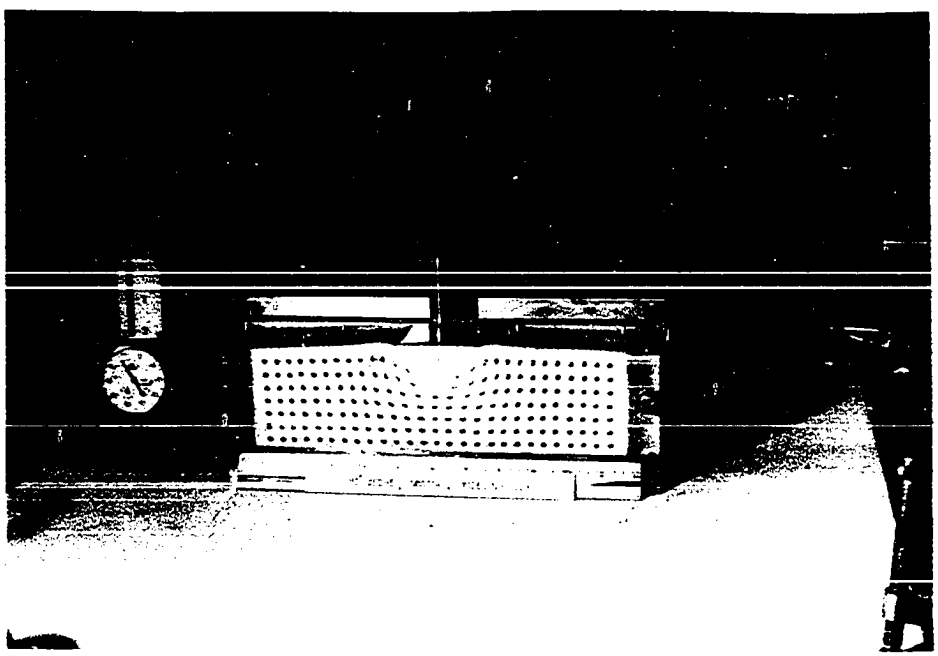

b)

Figure 19. Displacement model test; penetrometers and set-up

Table 2. Physical properties of Shelby and Monona soils

Properties	Monona Sioux City, Iowa	Shelby Knoxville, Iowa
Horizon sampled	B/C	B/C
Textural Composition, %		
Gravel (>4.76 mm.)	0.0	0.0
Sand (4.76 - 0.074 mm.)	0.6	2.6
Silt (0.074 - 0.005 mm.)	78.4	57.4
Clay (<0.005 mm.)	21.0	40.0
Colloids (<0.001 mm.)	17.0	34.1
Physical Properties:		
Liquid limit, %	32	54
Plastic limit, %	26	32
Plasticity index, %	6	22
Specific gravity	2.71	2.70
Classification:		
Textural	Silty clay loam	Silty clay
Engr. AASHTO	A-4 (8)	A-7-5 (15)
Predominant clay minerals	Montmorillonite	Montmorillonite
Other clay minerals	Illite[a] Kaolinite[a]	Illite[a] Kaolinite[a]
Geological description	Loess, calcareous	Kansan Till, oxidized, leached

[a]Indicated clay mineral present in small amount.

The 35 mm single lens reflex camera is used to record the soil deformations. It is mounted to the scale platform so that no relative movement can take place between the camera and the displacement box.

Sample preparations

Table 3 presents the method of compaction, average densities, and water contents for the soil samples.

Table 3. Sample preparation for displacement model test

Samples	Method of Compaction	Average Density (pcf)		Average Moisture Content (%)
		Total	Dry	
MC-11-15	Kneading and static	97.7	-	-
SB-11-15	Static	126.4	107.1	18.00
SB-21-25	"	101.8	84.8	20.05
SB-41-45	"	108.3	93.7	15.58
SB-61-65	"	114.7	93.0	23.31
OS-11-15	Vibration	106.2	106.2	Dry
MN-12 and 14	Static	124.40	106.1	17.19

The samples were transferred from compaction molds except that the Ottawa sand and the modeling clay were compacted in the displacement box. The $\frac{5}{32}$ in. dia. steel balls were placed at 1 cm spacing

on grid points on the front of the samples. A template was used to provide an accurate spacing; then the Plexiglass front was bolted on.

Testing procedures

The penetrometers were pushed down at the mid-length of the samples, and resisting forces were recorded at every 0.1 in.[1] penetration up to 1.6 in. Photographs were also taken at the same penetration intervals, which created multi-exposure images showing the movements of the grid points.

Another technique, reported by Butterfield, Harkness and Andrawes (8), was attempted by taking individual photographs at each penetration increment. Viewed stereoscopically, a pair of successive photographs then shows a stereo-image related to the movement of soil particles; the farther they move, the greater the "depth" perceived. This method does not require grid points so long as the sample shows distinctive tones between particles. The method was not applicable to the modeling clay.

Penetration of Proctor Samples

Penetration tests were performed on 1/30 - cubic foot Proctor samples in order to check the following:

1. The general behavior of cone and of sphere penetrations.
2. The application of penetration tests as a direct method

---

[1] For some samples, the forces were recorded at 0.025 and 0.05 in. intervals.

to evaluate soil parameters in the laboratory.

3. The relation of cone and sphere penetration to soil density and water content.

The materials used for the Proctor sample test were modeling clay and Shelby soil.

Apparatus

The penetrometers and equipment set-up are shown on Figure 20. A motorized California Bearing Rate machine with 0.1 in./min strain rate was adapted for the test. The 30° and 60° cones, and the 1, and 1.5 in. diameter spheres were the test penetrometers.

Sample preparation and testing

The modeling clay was kneaded and statically compacted into the Proctor mold, to reduce air voids inside the sample. The Shelby soil was compacted at standard Proctor conditions under the five control water contents. Densities and water contents were determined for every soil sample.

The cone and sphere penetrometers were loaded at the center of the sample and resisting forces were recorded at every 0.05 in. to about 1.5 in. penetration.

Soil-Steel Friction Test

Direct soil-steel friction tests were performed using a 45° wedge field penetrometer as shown in Figure 21. A normal load (N) was applied and the shearing force (F) increased until a slipping movement occurred between soil and wedge. Figure 22 shows the

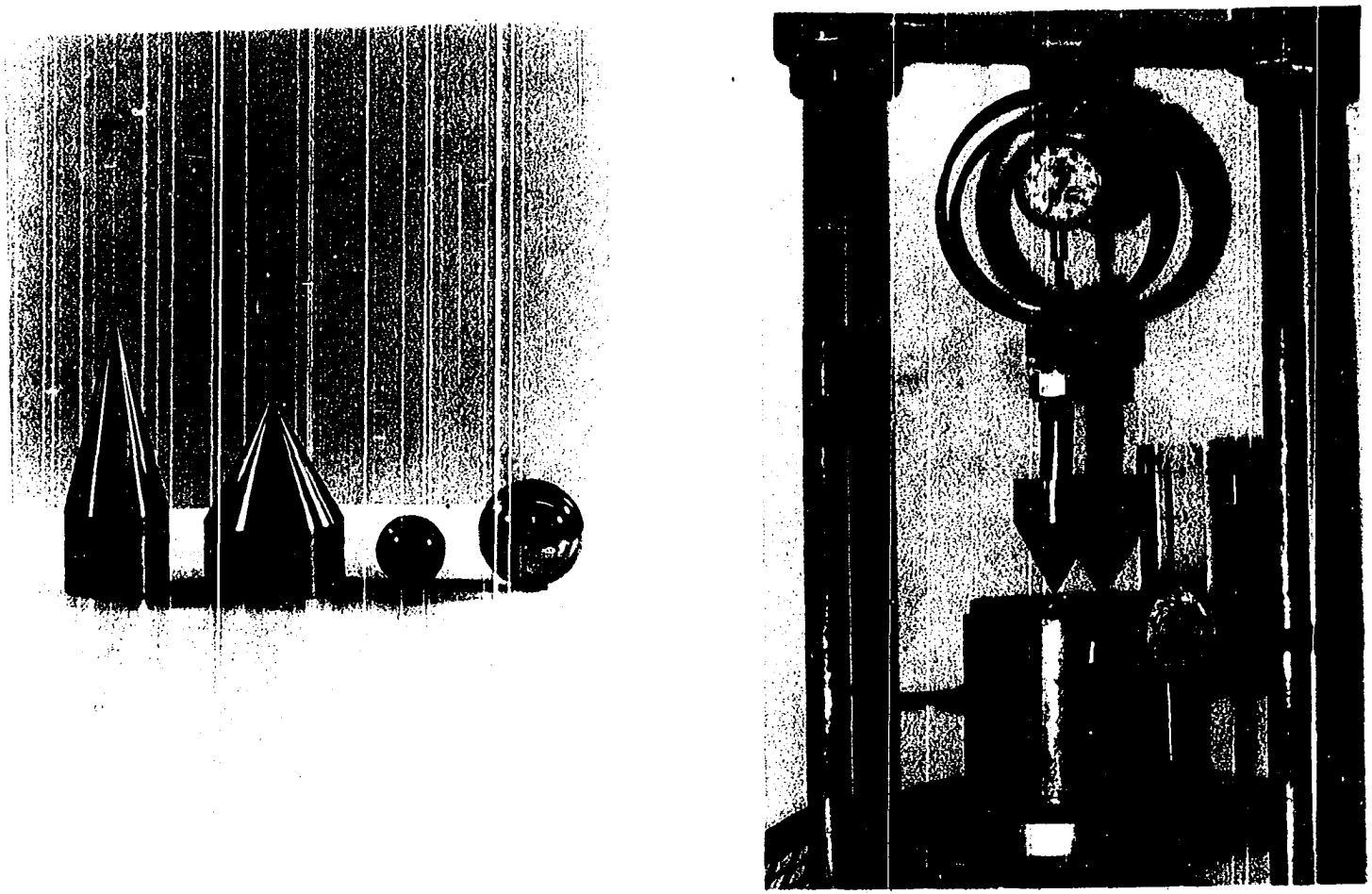

a) b)

Figure 20. Proctor sample test; penetrometers and set-up

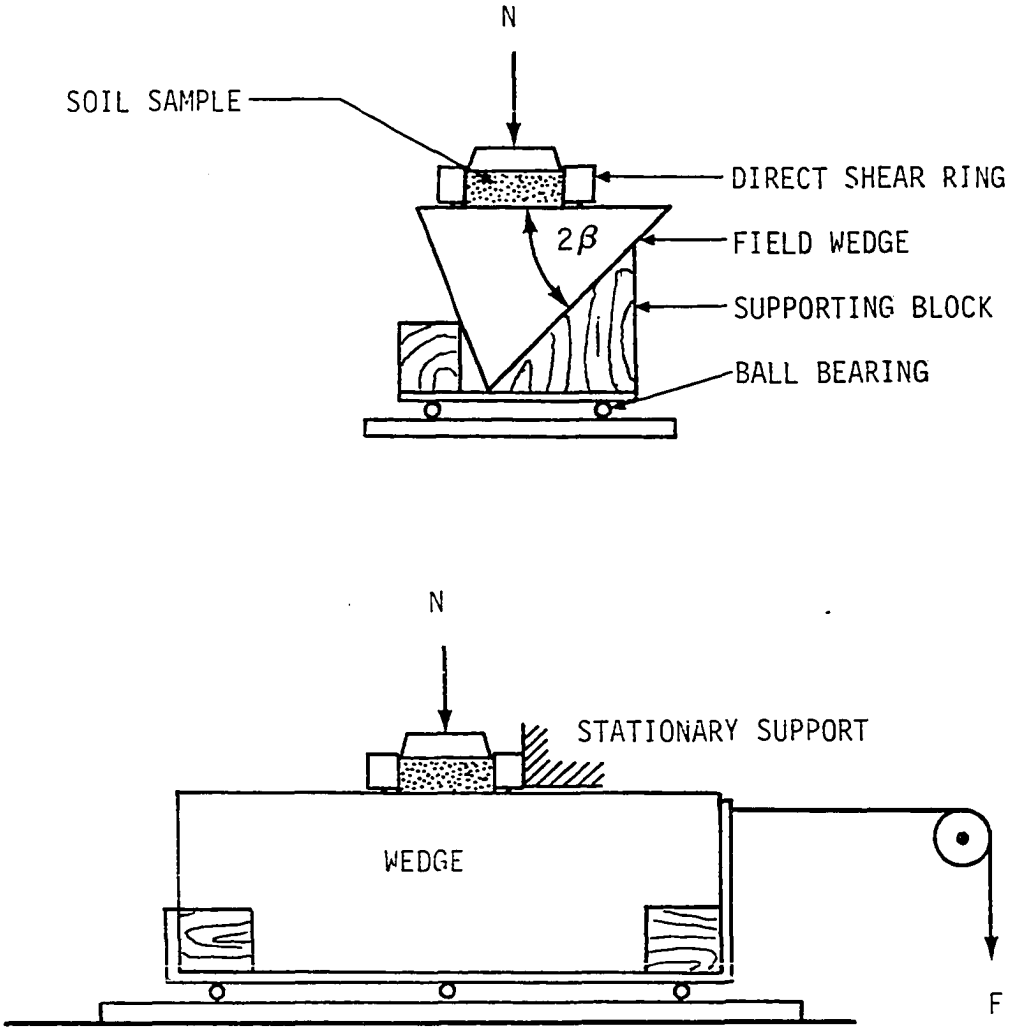

Figure 21. Schematic of soil-steel friction test

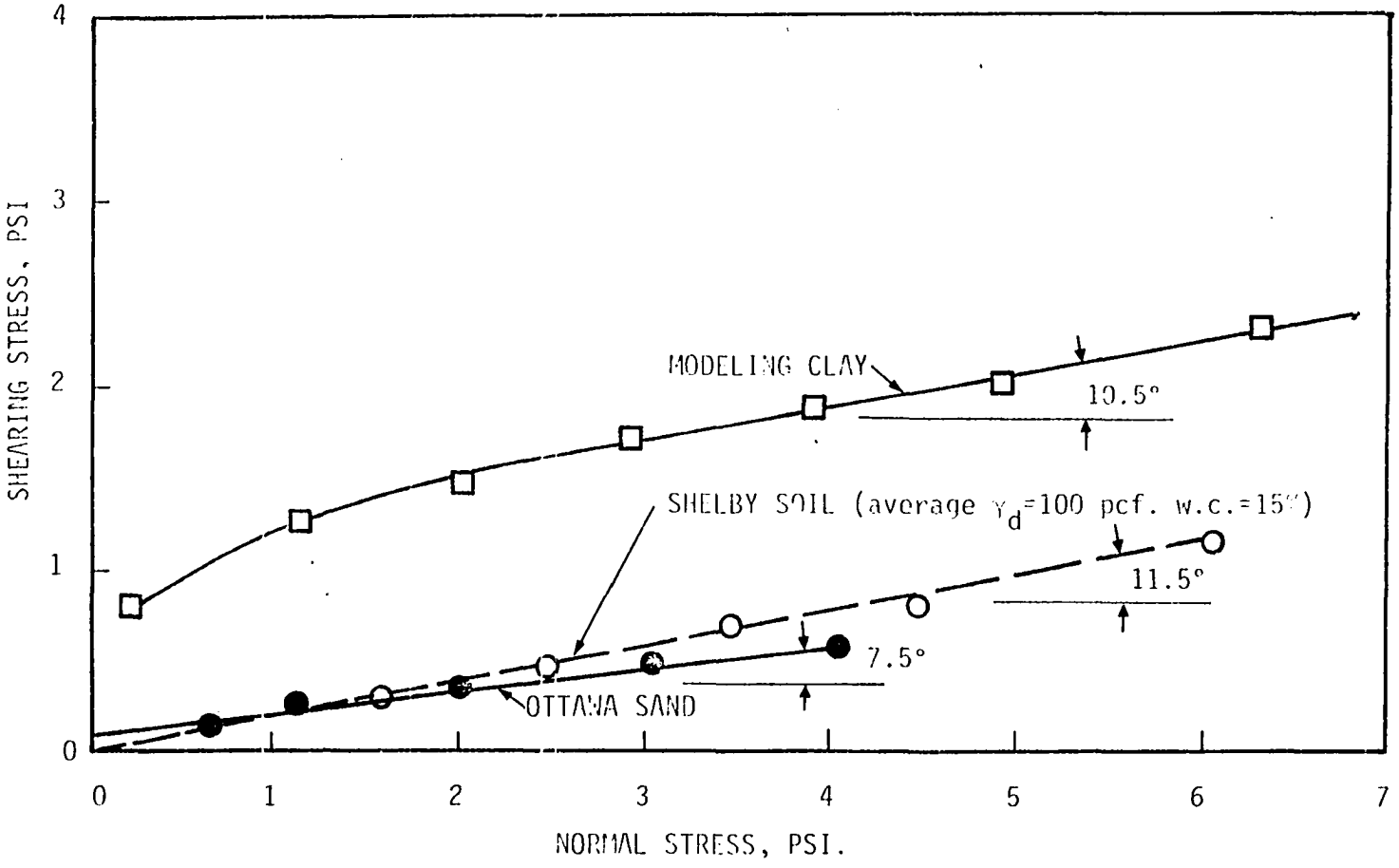

Figure 22. Soil-steel friction for Shelby soil, modeling clay and Ottawa sand

results from Shelby soil, modeling clay and Ottawa sand.

Field Test

Field tests were attempted primarily to see what problems might arise from penetration testing under field conditions, to determine in situ shear strength parameters.

Description of soils

Two types of soil were tested, Clarion loam and a silty sand. The Clarion is derived from calcarious glacial till, located west of Ames on Iowa State University farm. The silty sand is on a county road near Alburnett, Linn County, Iowa. Physical properties of the tested soil are summarized on Table 4.

Table 4. Properties of field tested soils

Properties	Clarion soil	Silty sand
Textural composition, %		
Gravel (>4.76 mm.)	0.0	0.0
Sand (4.76-0.074 mm.)	40.7	84.2
Silt (0.074-0.005 mm.)	30.4	14.5
Clay (<0.005 mm.)	25.5	1.3
Dry density, pcf.	95.4	104.2
Field water content, %	22.0	6.9

Field penetrometers

The field penetrometers are shown in Figure 23a: 30° and 45° wedges 12 in. long, 30° and 60° cones, and a 6 inch diameter sphere. Loading was with a 10,000 lb. hydraulic jack mounted at the back of a load test truck, Figure 23b.

Penetrations were measured by use of a dial gage attached to a cantilever arm from five feet away to avoid local surface deformations around the penetrometer.

Test procedure

The top six inches of desiccated soil was removed and the area was leveled. The penetrometer was set vertically below the jack; an initial seating load was applied and the dial gage was zeroed. A load increment of 220 lb was applied by the jack, and the penetration was recorded when the gage was steady.

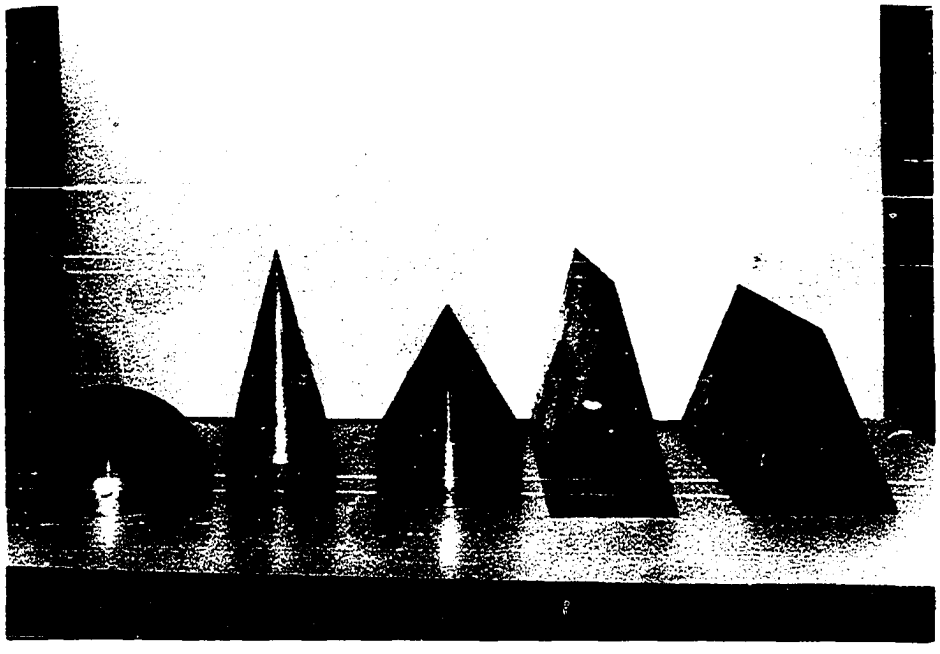

a)

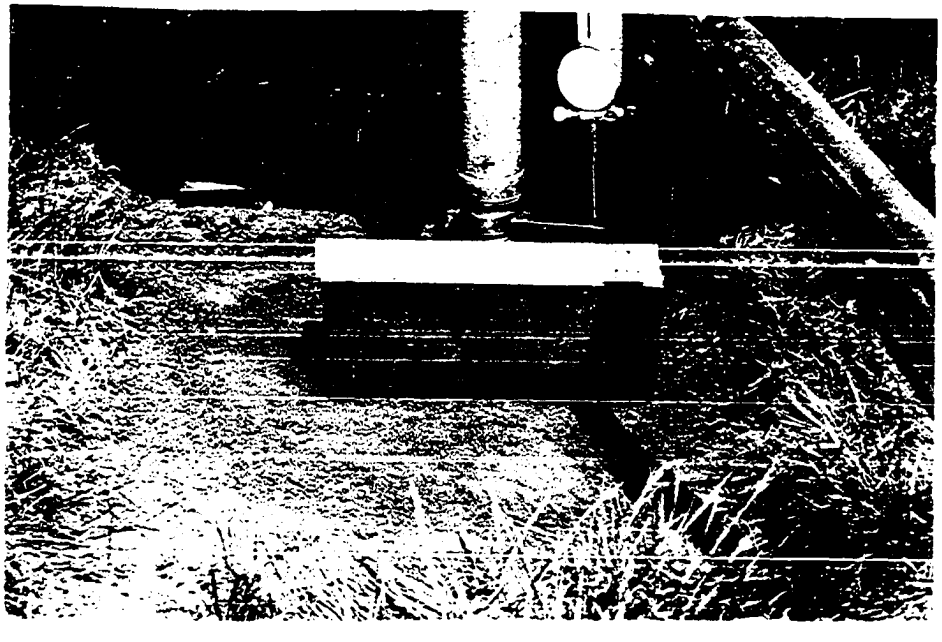

b)

Figure 23. Field test; penetrometers and set-up

PRESENTATION AND DISCUSSION OF RESULTS

Saturated Cohesive Soil

(Modeling Clay)

Displacement model test

The Figures 24 to 27 are photographs showing the progressive deformation of modeling clay during penetration tests. Below are shown corresponding vector fields. The continuous points on the photograph represent the positions of grid balls after every 0.1 in. penetration for the wedges and 0.05 in. for the cylinders.

No discrete failure boundaries were observed during 0-1.6 in. penetration, perhaps because of the highly plastic remoldable nature of the modeling clay. The movement along selected vertical planes during the last 0.4 in. of penetration was plotted vs. depth, Figure 28, the slopes of the curves representing shearing strains. The point on each curve where an abrupt change in slope occurs may be defined as a failure plane, but most of the curves are smooth. An exception is the 60° wedge, where two curves show changes of slope, both occurring at about 0.05 in. movement. Therefore the contour showing 0.05 in. movement was more-or-less arbitrarily taken as the failure boundary for every case with the modeling clay.

The theoretical failure boundaries were established based on modified Prandtl slip-line theory as mentioned before. The parameters ϕ and ϕ_s needed to establish the slip-line geometry were obtained from the soil-to-steel friction and from the wedge penetration data,

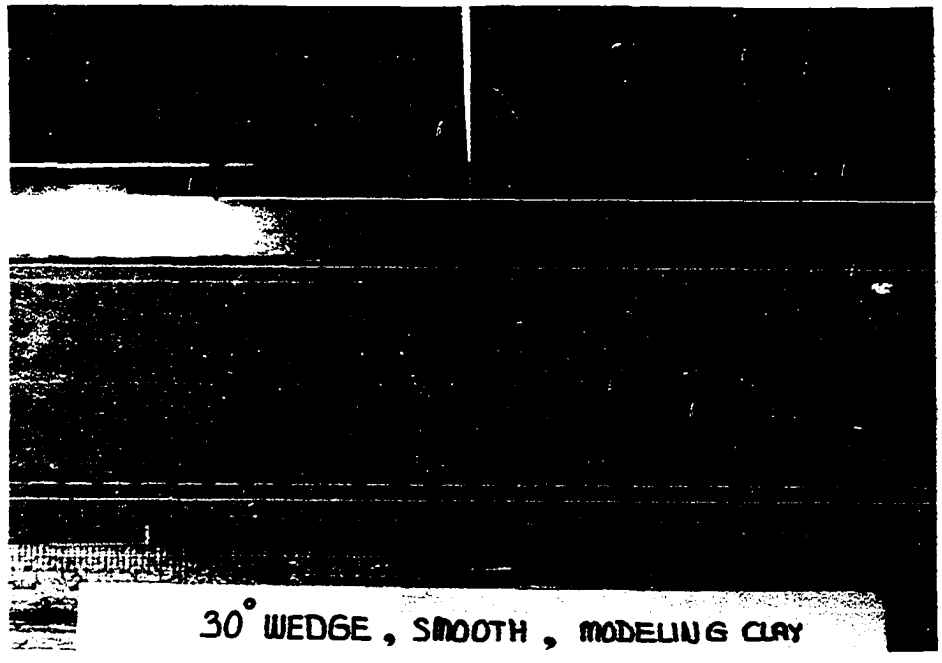

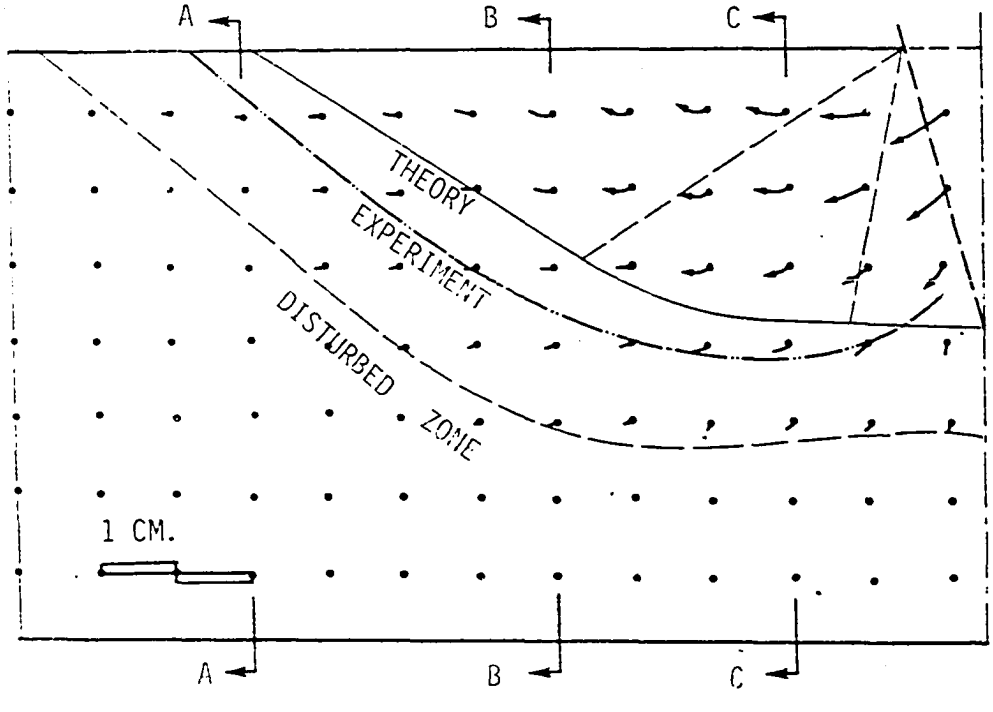

Figure 24. Soil deformation and vector field under 30° wedge penetration on modeling clay

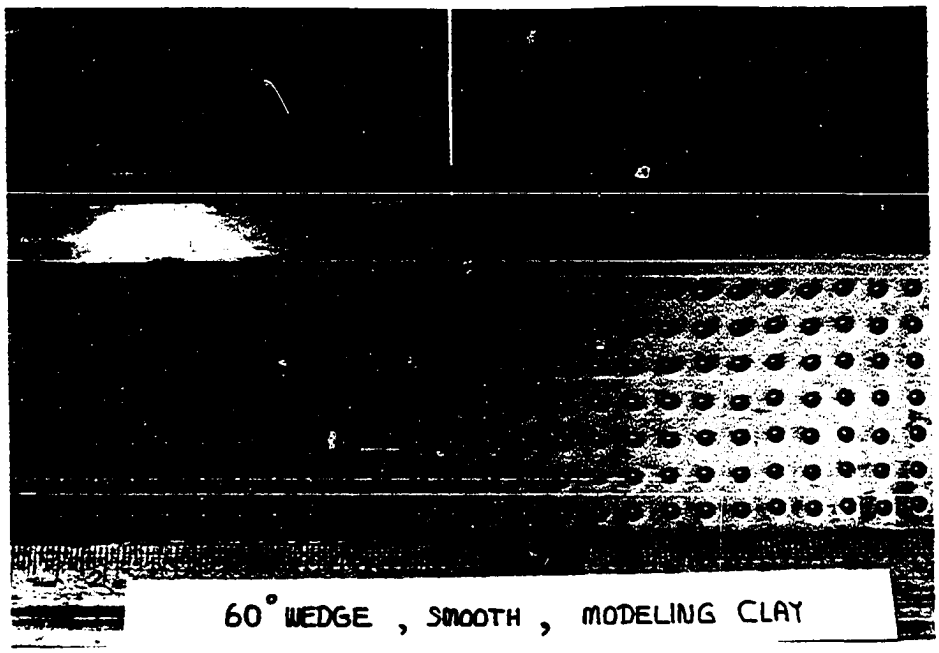

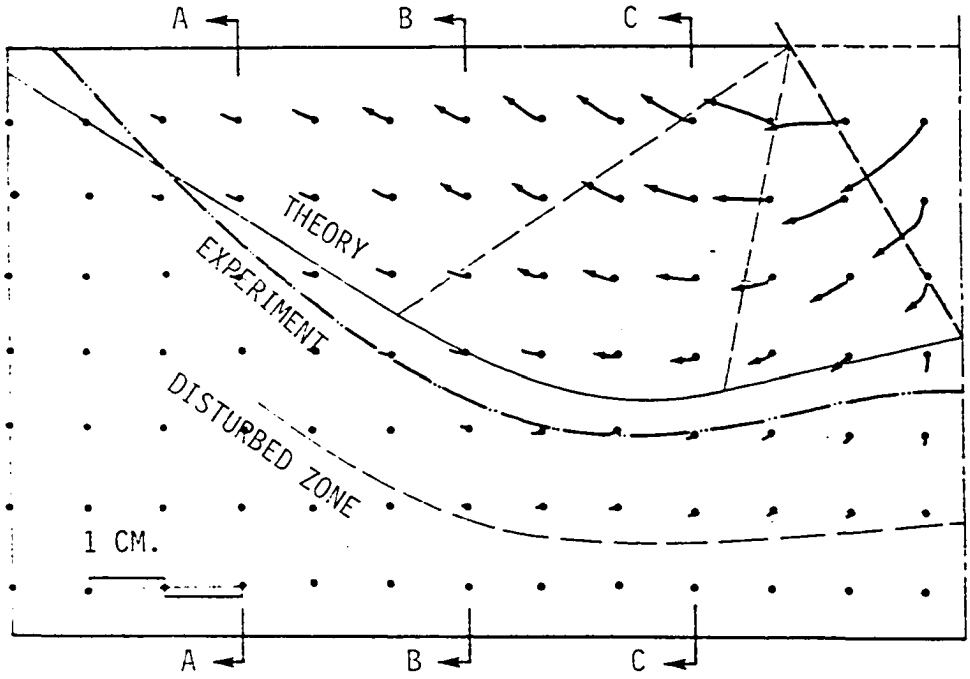

Figure 25. Soil deformation and vector field under 60° wedge penetration on modeling clay

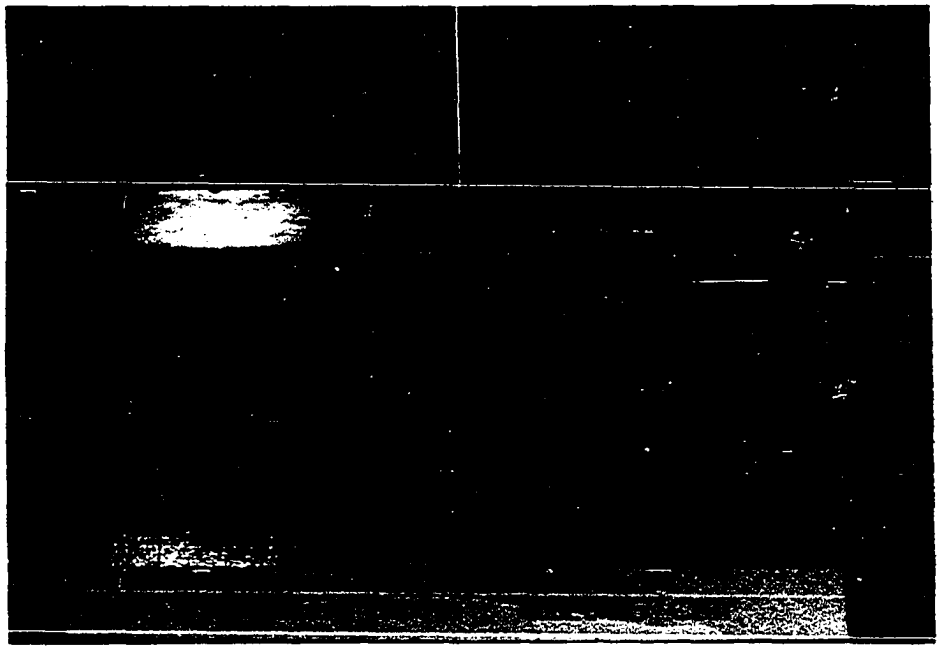

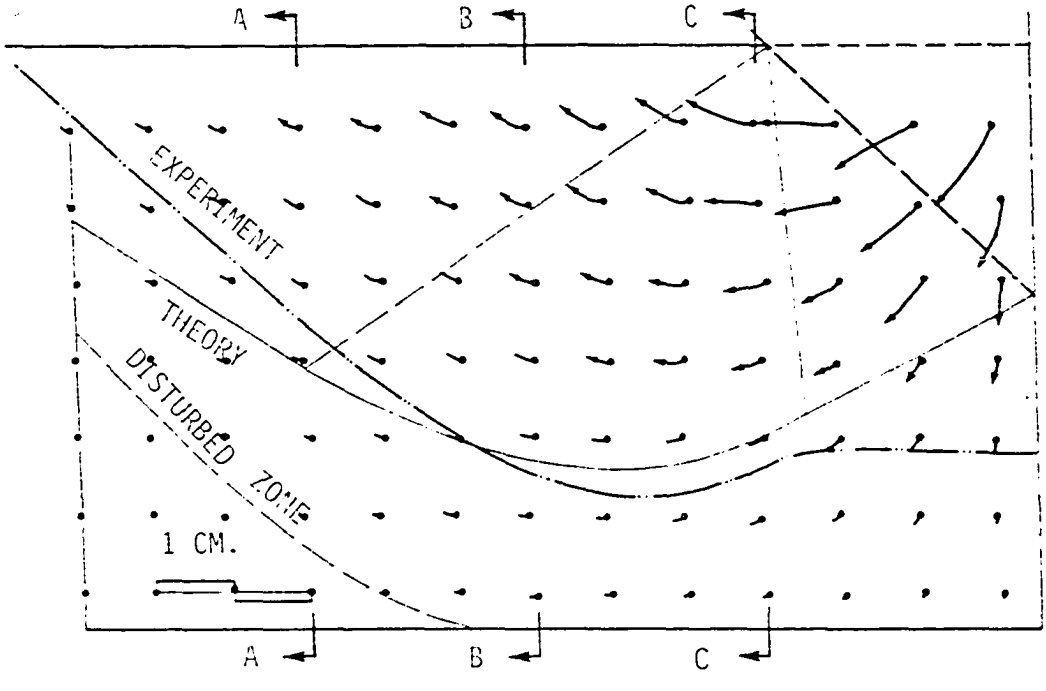

Figure 26. Soil deformation and vector field under 90° wedge penetration on modeling clay

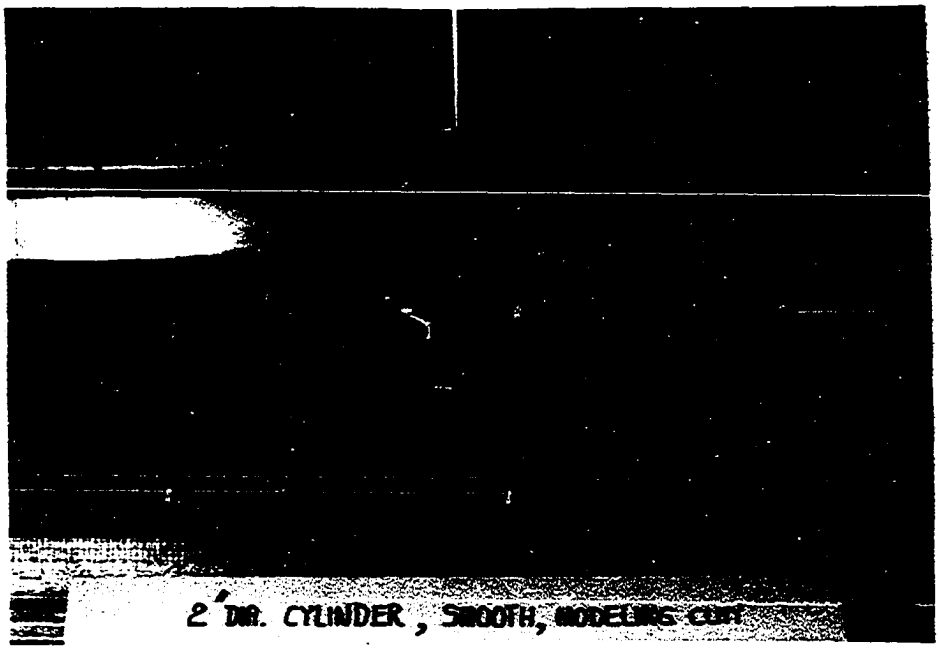

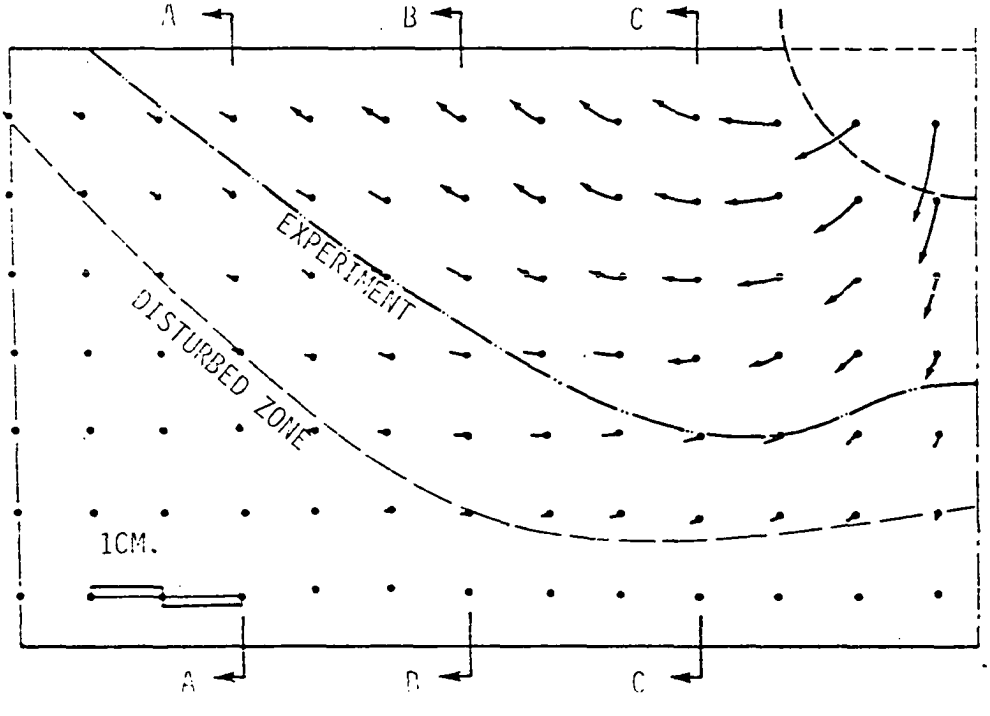

Figure 27. Soil deformation and vector field under 2.0 in. dia. cylinder penetration on modeling clay

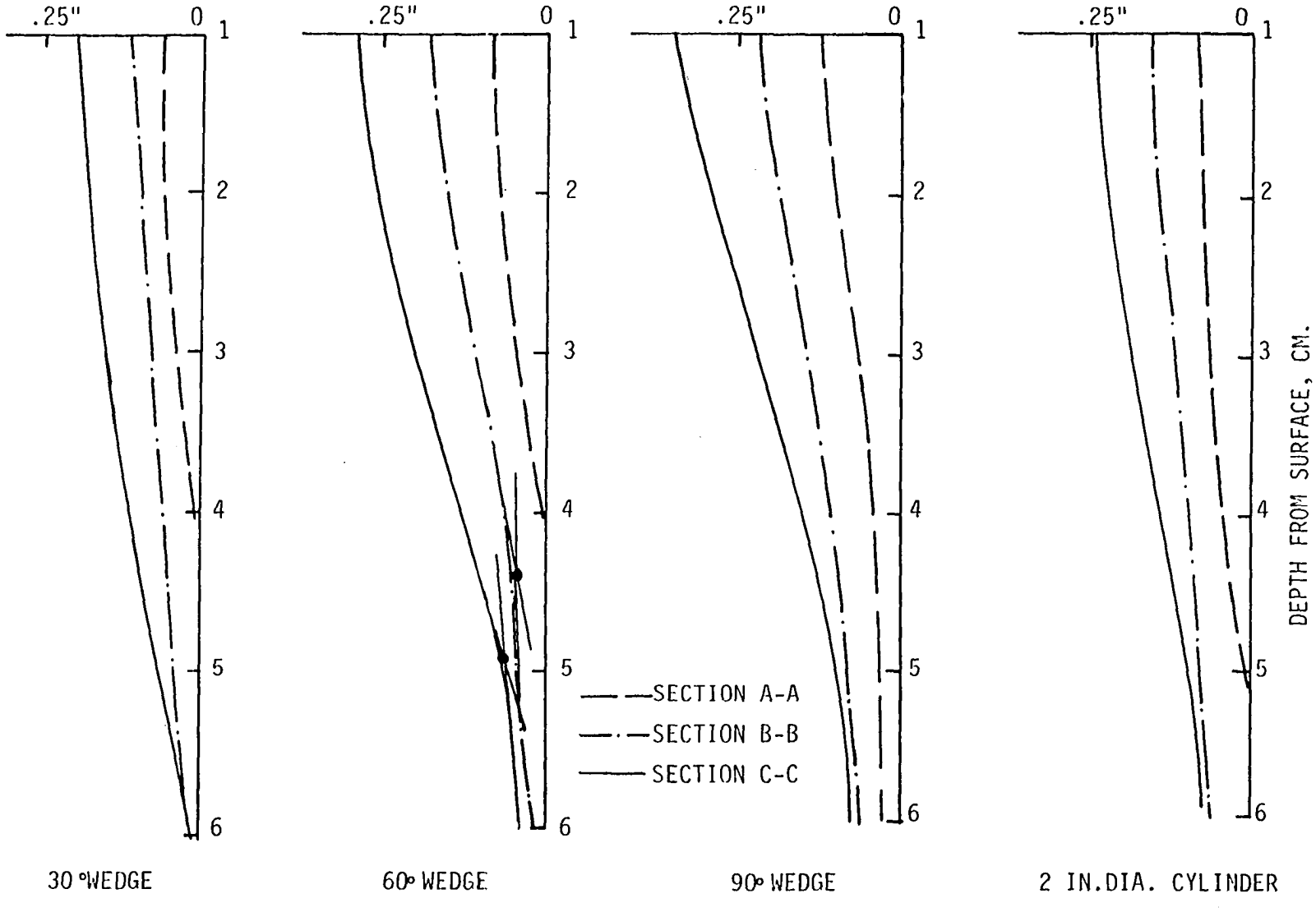

Figure 28. Soil movement along selected planes in modeling clay

as will be described later. A similarity in patterns and reasonable agreement between experimental (based on 0.05 in. movement) and theoretical failure boundaries can be seen in Figures 24 to 27. Movements outside of the defined failure boundary probably represent a transition, but for the purposes of the analysis may be considered as elastic deformation. In the figures it is simply labelled "disturbed zone". Generally the disturbed zone was larger from penetration of the larger angle wedge and the cylinder.

Force-penetration relation

Wedge The plot of resisting force on the penetrometer versus the depth of penetration is sometimes called a "penetration curve". Typical penetration curves of the wedges are shown in Figure 29. These are not exactly straight lines as predicted by the mathematical expression, but rather curve upward. This may be because of the deepening failure zone boundaries and increasing transitional or disturbed zone as penetration goes deeper, and perhaps restriction of movement by the rigid, unyielding boundary at a depth of 3 in. The early portions of the curves therefore were used in evaluation of the strength parameters.

The method of evaluating c and ϕ from results of tests with pairs of wedges was illustrated in APPENDIX G. Results calculated from different wedge pair combinations are shown in Figure 30. The values show the best agreement at the penetrations between 0.5 and

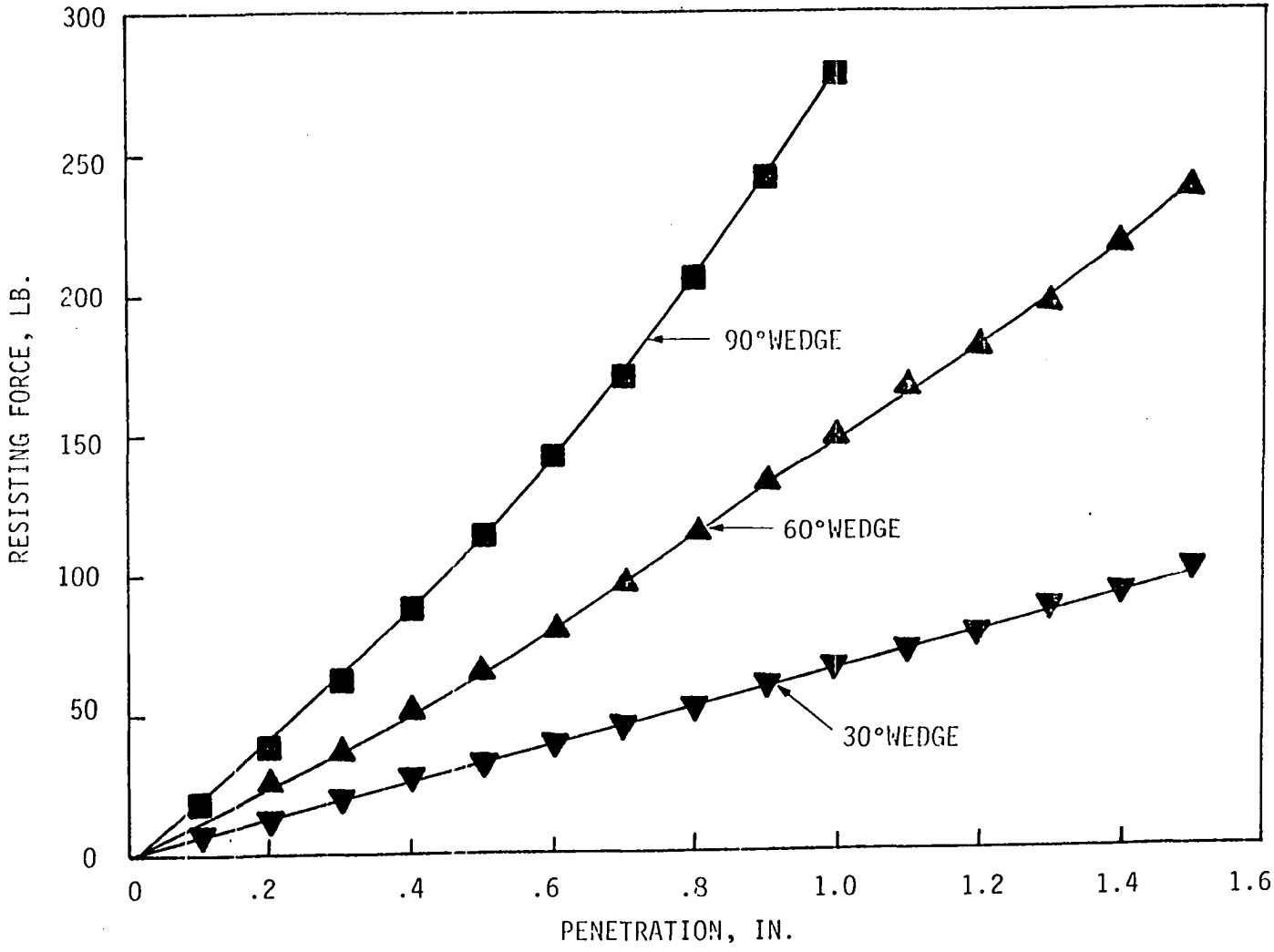

Figure 29. Penetration curves for wedges on modeling clay

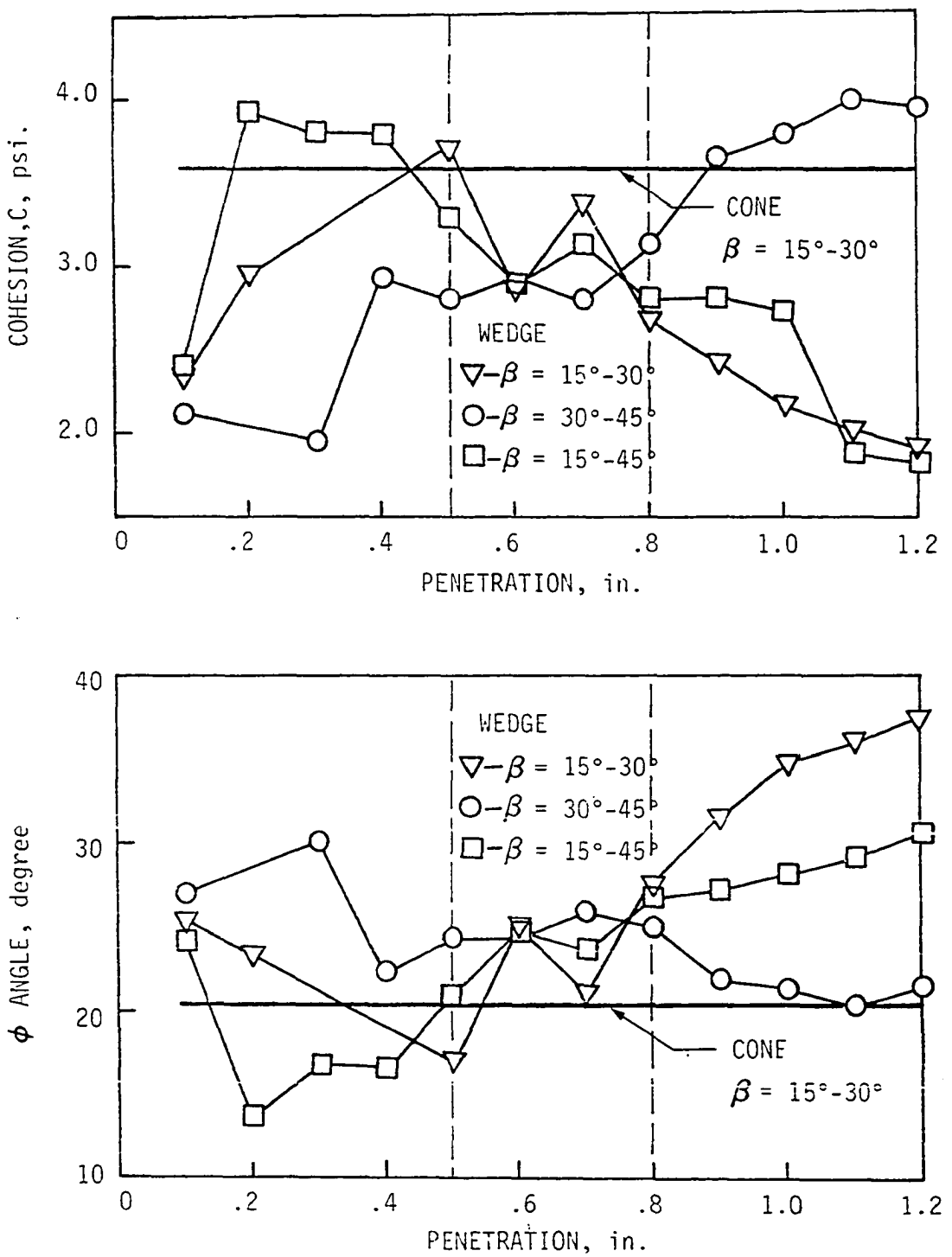

Figure 30. Soil strength parameters for modeling clay from wedge and cone penetrations

and 0.8 in., with every close agreement at 0.6 in. penetration, as presented in Table 5.

Table 5. Basic soil parameters for modeling clay by wedge penetration

Wedge angles (degree)	cohesion (psi)	ϕ (degree)
30°-60°	2.87[a]	24.8
60°-90°	2.93	24.2
30°-90°	2.90	24.5

[a]The calculations are based on soil-steel friction = 10.5°

The average ϕ angle obtained from wedge penetration is many times higher than the values reported from triaxial tests and K-Tests, which are between 4° to 6°. This discrepancy is believed due to the following reasons:

1. The penetration test operates under very low confining pressure, such that the clay may tend to shear as clusters or aggregates rather than as individual particles.
2. The elastic zone is increased as the wedge angle increases and giving a higher resisting force.
3. The boundary of the penetration box has a larger confining effect with larger wedge angles.

The values of cohesion from triaxial tests was reported to be about 3 psi, which agrees with the average of 2.9 psi from penetration test.

Cylinder Figures 31 and 32 present penetration curves for 1.0 and 2.0 in. diameter cylinders in modeling clay. The theoretical curves were evaluated from equation (32) using $\phi = 24.6°$, $\phi_s = 10.5°$ and $c = 2.9$ psi, and predict higher resisting forces that were approached as penetration progressed. The experimental curves show straight-line portions at penetration depths less than 15 to 20 percent of the diameter, which suggests two possible phenomena:

1. The elastic state of stress occurred at small penetration and gradually developed into a plastic state.
2. The mechanism during penetration was not controlled by the cylindrical shape but by a wedge of clay forming beneath the cylinder and moving along with the penetrometer.

An evidence supporting the latter idea is that the vector fields for the 60° wedge and for the 2 in. diameter cylinder, Figures 25 and 27, are very similar, both in direction and in magnitude.

A modification of theoretical prediction equation (32) was therefore attempted based on the following assumptions:

a) Assume a soil wedge of $(\frac{\pi}{2} - \phi)$ apical angle moving along with the cylinder as shown of Figure 33.

b) At small penetrations, when H_a is less than H_{ac}, the penetration is by soil forming a rough wedge ahead of the cylinder.

c) At large penetrations when H_a is larger than H_{ac}, the penetration is by the combined soil wedge and steel cylinder.

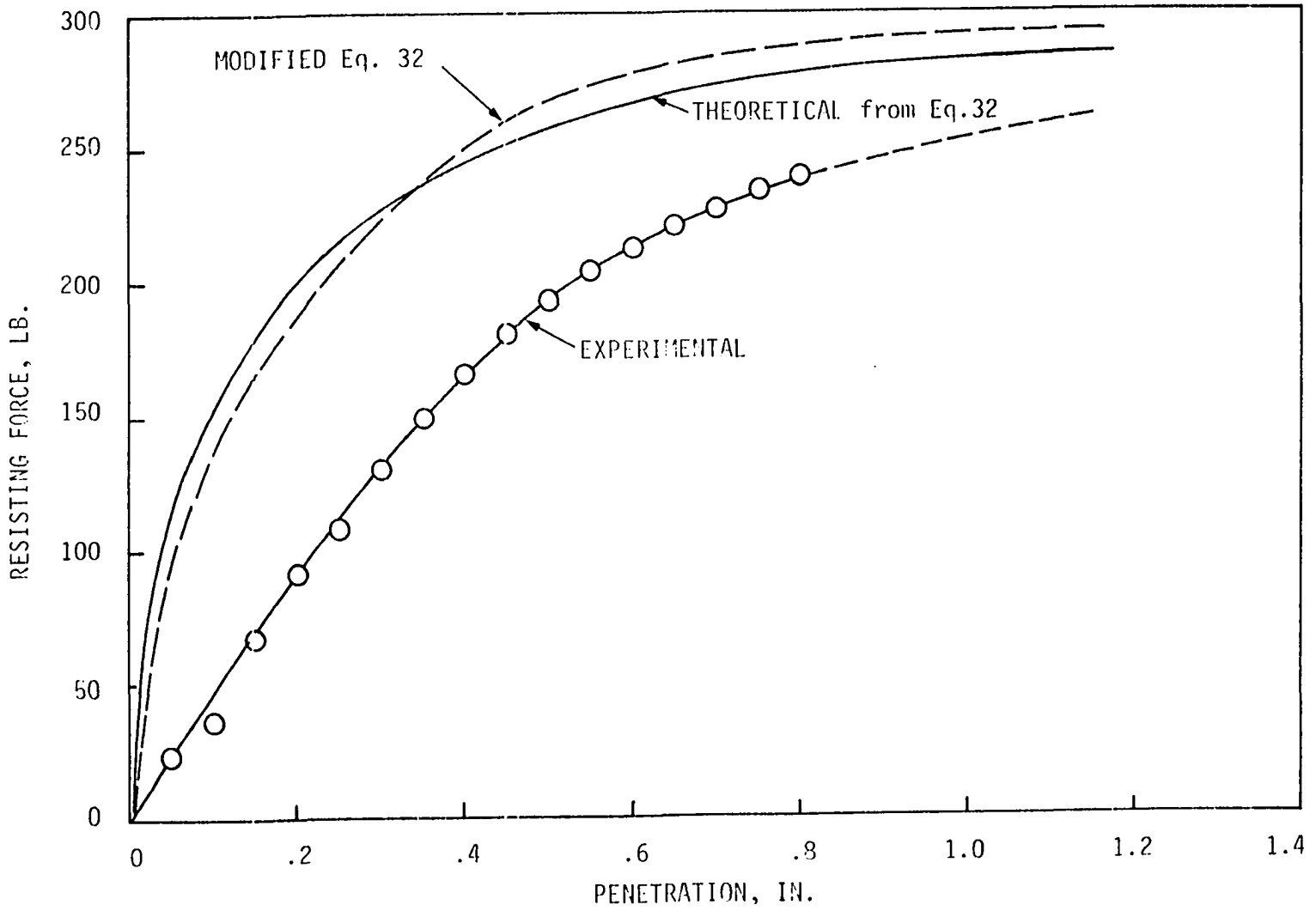

Figure 31. Penetration curves for 2.0 in. dia. cylinder on modeling clay

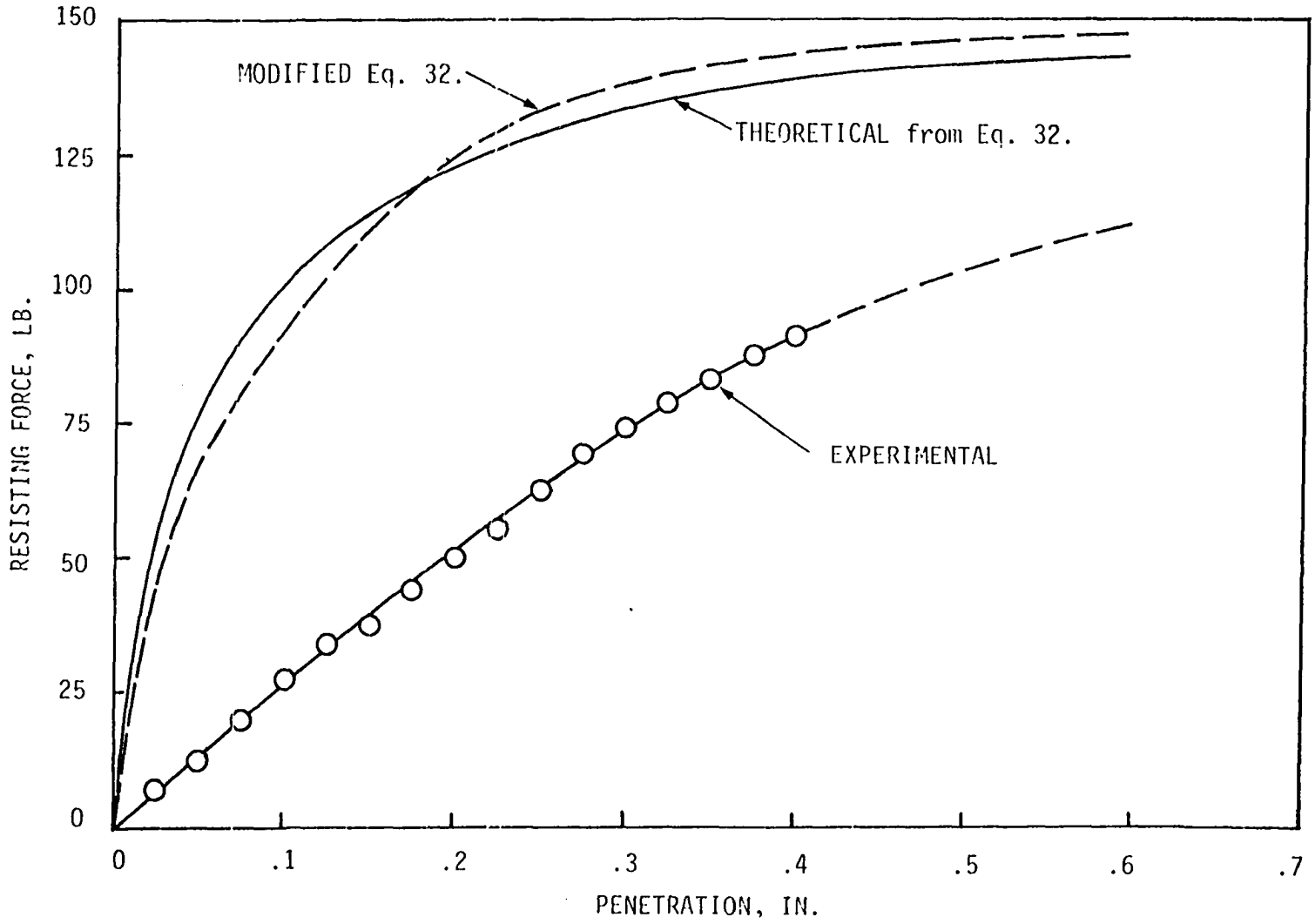

Figure 32. Penetration curves for 1.0 in. dia. cylinder on modeling clay

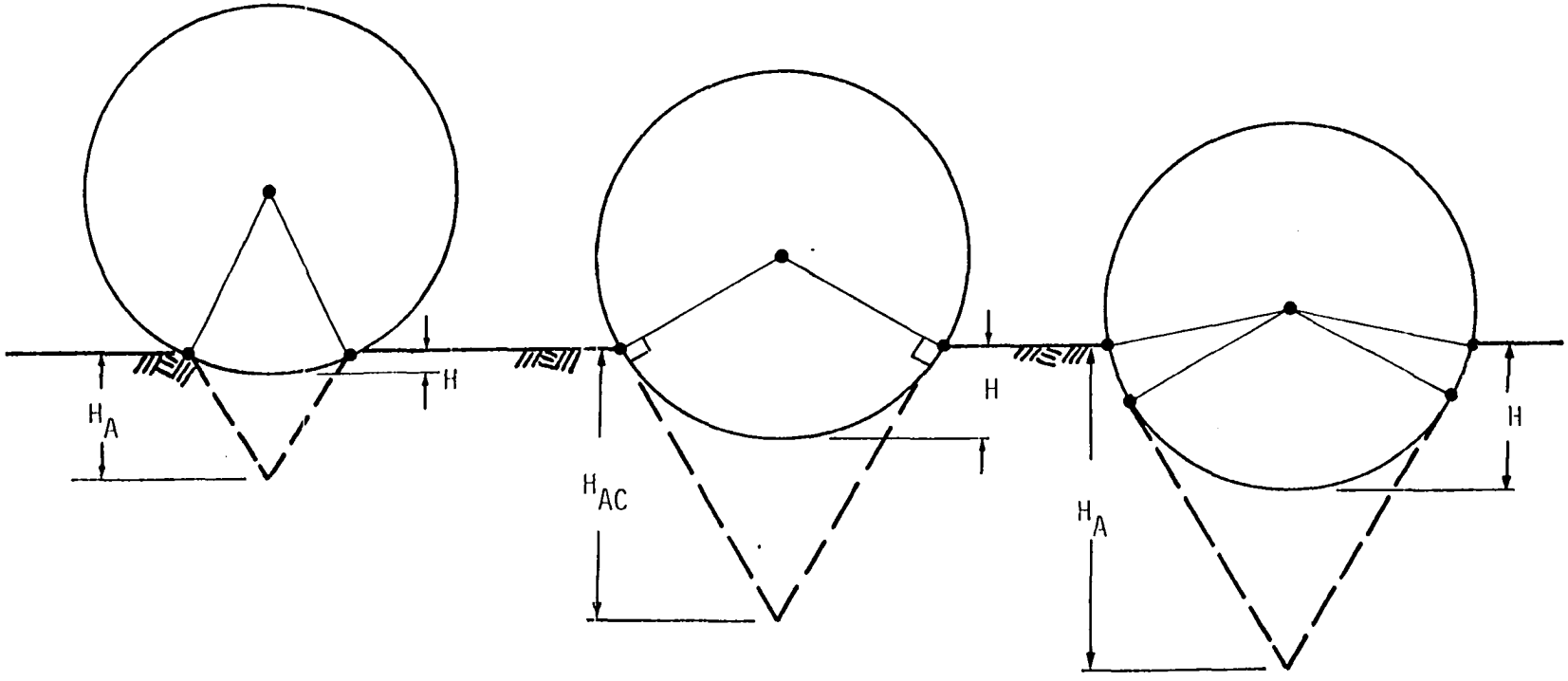

STAGE 1. WEDGE ACTION STAGE 2. FULLY WEDGE ACTION STAGE 3.COMBINE WEDGE-CYLINDER

Figure 33. Modified cylinder penetration

The details of mathematical expression for the modified equation (32) are presented in APPENDIX C. The solutions indicate a relatively small difference from equation (32), as shown in Figures 31 and 32.

Cone Figure 34a shows typical experimental cone penetration curves on modeling clay. When the square root of force is plotted versus penetration, the result is a straight line relation as shown on Figure 34b. The theoretical expression of equation (41) also gives the same relationship, since for a given soil and cone, the resisting force should be proportional to the square of the penetration.

The experimental evaluation of soil parameters from comparative results with 30° and 60° cones gave a value for cohesion of 3.59 psi and for friction angle, 20.5°. Since the slope of transformed linear plot is used to calculate soil parameters, only one pair of c and ϕ values is obtained for penetration of a cone set.

Sphere The penetration curves of the 1.0 and 1.5 in. diameter spheres are presented in Figures 35 and 36. The plots generally show straight lines at penetration less than 25 to 35 percent of the diameter of sphere, and then flatten down as the penetration increased. The same type of curve was observed by Richardson, and by Dexter and Tanner (34, 13), who represented it by an empirical equation,

$$F = A + B.e^{-k\ (L/R)}$$

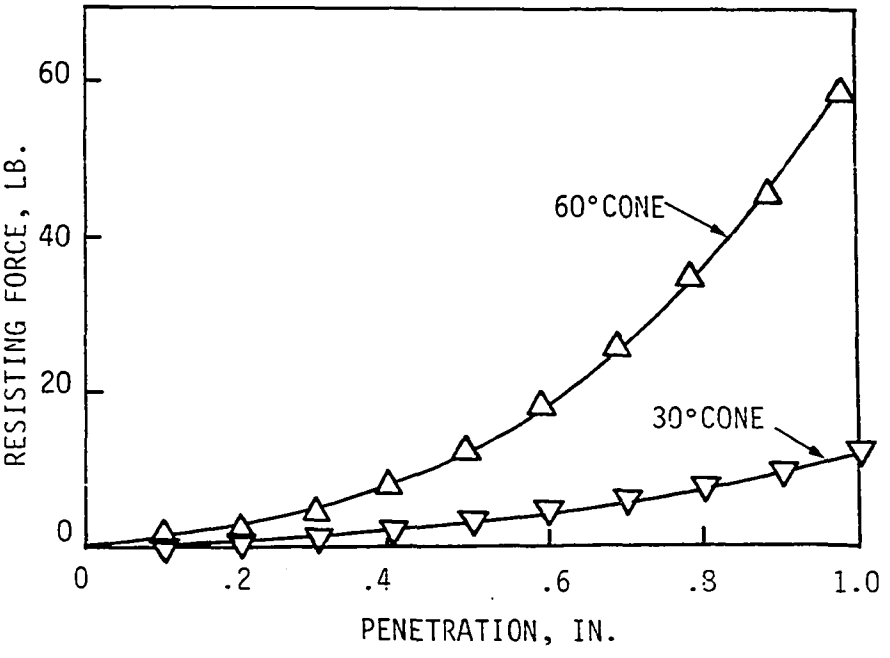

a)

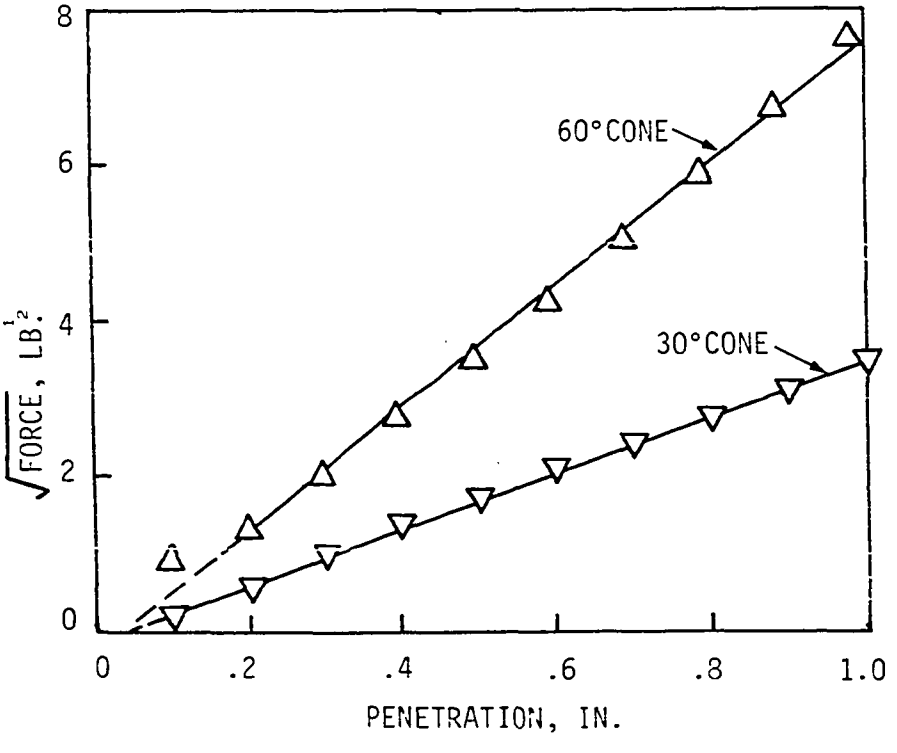

b)

Figure 34. Actual and transformed penetration curves for 30° and 60° cones on modeling clay

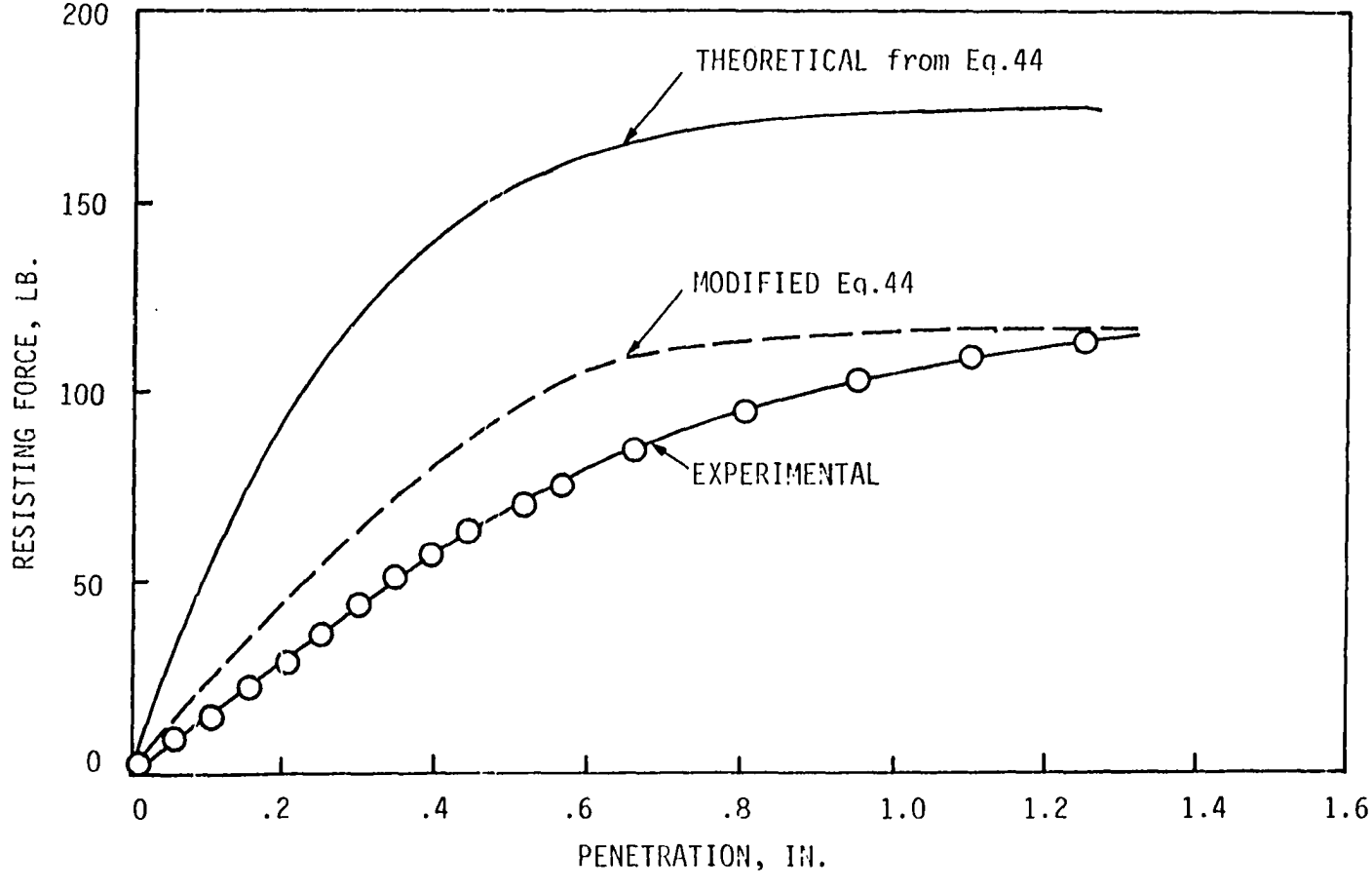

Figure 35. Penetration curves for 1.5 in. dia. sphere on modeling clay

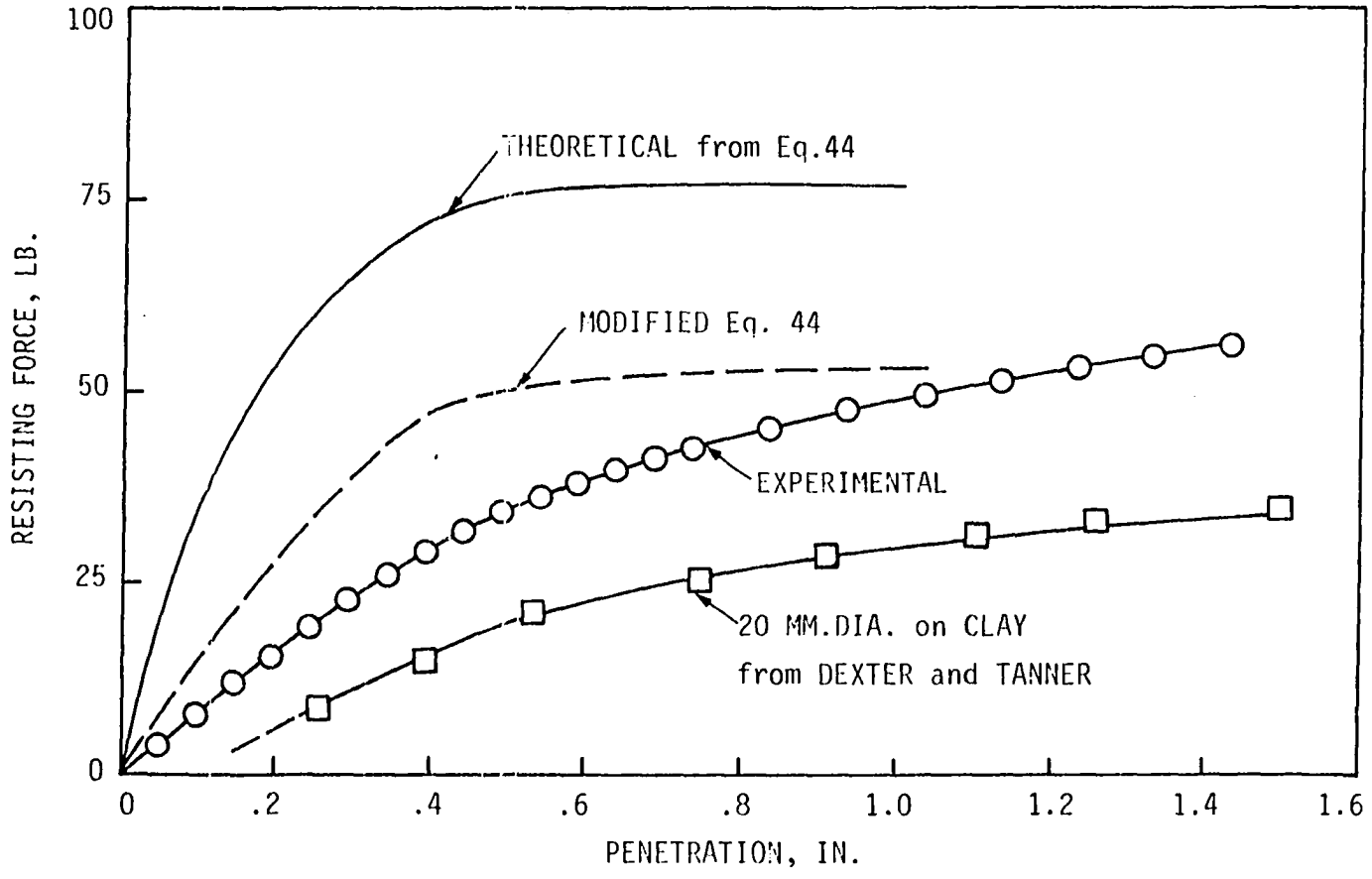

Figure 36. Penetration curves for 1.0 in. dia. sphere on modeling clay

where

F = resisting force on the sphere

A, B and k = adjustable parameters

L/R = dimensionless depth of penetration.

The experimental curves obtained by Dexter and Tanner for a 20 mm diameter sphere penetrating on clay are also shown on Figure 36. The theoretical expression from equation (44), as shown on Figure 35 and 36, using the average soil parameters from wedge penetration $\phi = 24.6°$, $\phi_s = 10.5°$ and c = 20.9 psi, gave much higher resisting forces. A modification of equation (44) was made based on the same assumption as for cylinder penetration, but with a cone of soil rather than a wedge of soil beneath the sphere. This gave closer agreement to the experimental data. The modified penetration curves on Figure 35 and 36 also exhibit a straight-line portion but at somewhat higher resisting force than from experiment.

In summary, the data obtained from cone penetration seem to show good agreement to the mathematically predicted equation, which may indicate that the idealized assumptions used in the derivations might fit rather closely to the actual cone penetration mechanism.

Unsaturated Cohesive Soil

(Shelby Soil)

Displacement model test

As has been mentioned before, the displacement model tests were performed to verify movements and failure patterns in comparison to

the hypothesized slip-lines. In this section the displacement of Shelby soil will be discussed generally in qualitative terms, and a quantitative approach will be discussed in the next section.

Figure 37 to 40 show typical soil deformations and their corresponding vector fields from plane strain displacement model tests. Again the boundaries of zero soil movement and of movement exceeding 0.05 in. for 1.2 to 1.6 in. of penetration established a reference for the movement pattern. The movement patterns show dramatic differences from those of modeling clay, the deformations in Shelby soil being predominantly vertical and radial downward movements caused by the compaction within the soil mass. Some shearing movements of upward rotation occurred in the area adjacent to the soil surface and penetrometer. The compaction mechanism was directly confirmed, as soil taken from beneath the penetrometer was found to have 5 to 15 pcf higher density than soil outside the disturbed zone. As penetration exceeded 1.5 in., shearing movements started to increase. Qualitatively, the compaction and shearing mechanisms of unsaturated cohesive soil were influenced by the following factors:

1. Penetrometer geometry

The shape of the penetrometer can be considered as a major influence on compaction vs. shearing, since it induces the direction of soil movement. In general with small angle wedges such as the 30° wedge of Figure 37, the cutting or shearing mechanism prevails because the soil moves outward laterally. On the other hand the

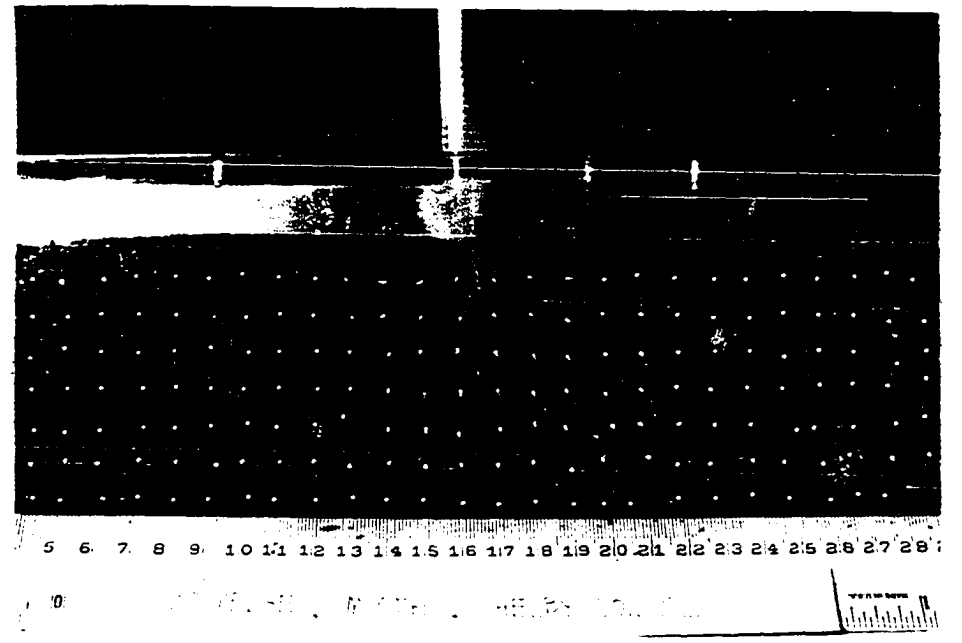

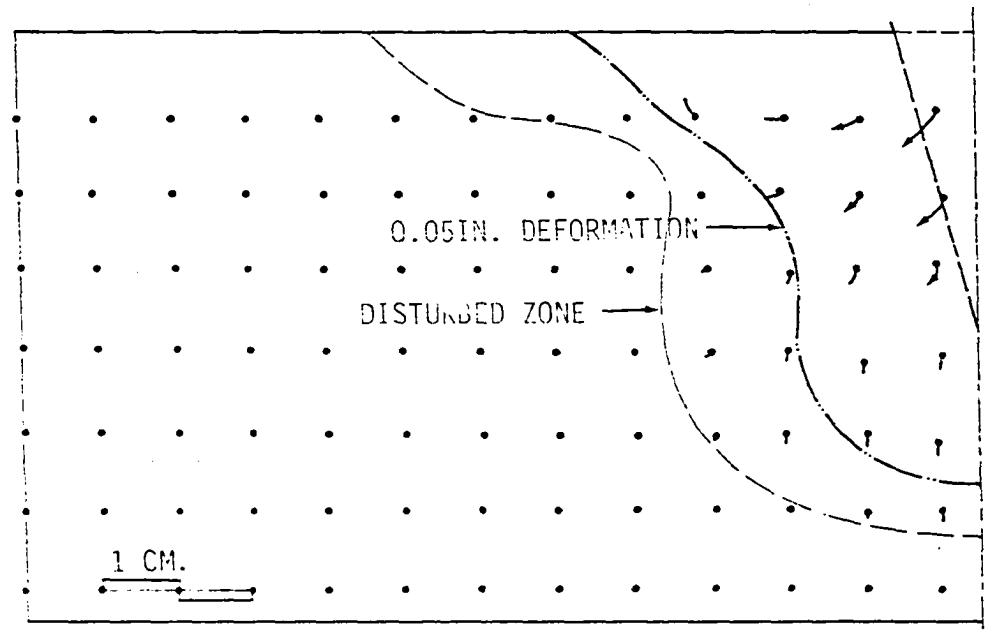

Figure 37. Soil deformation and vector field under 30° wedge penetration on Shelby soil

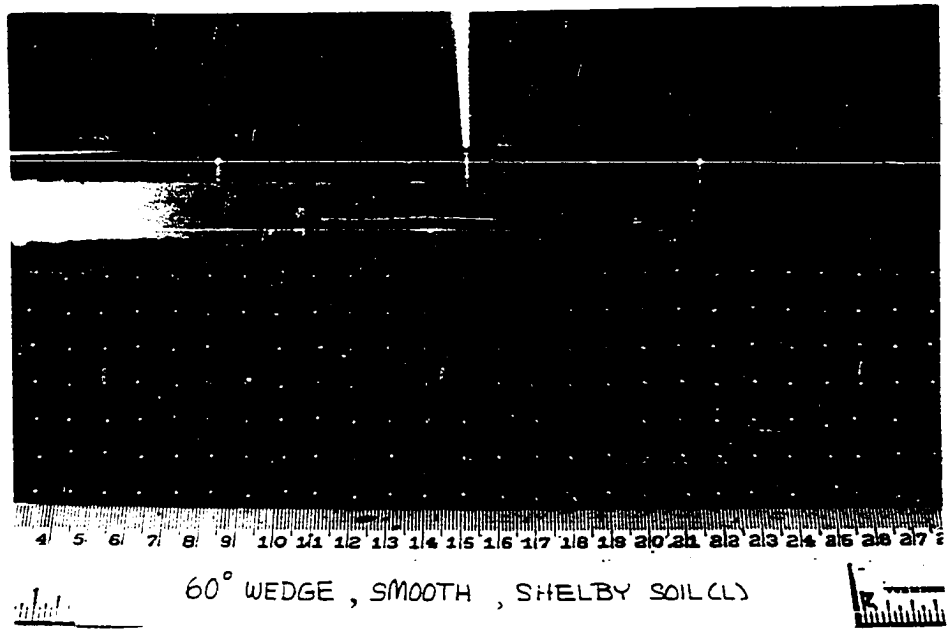

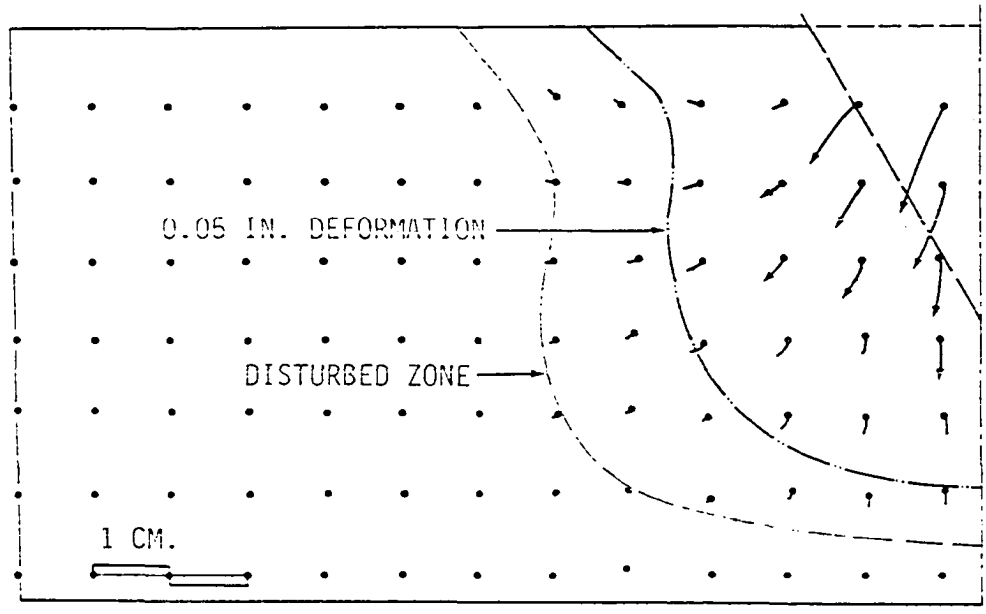

Figure 38. Soil deformation and vector field under 60° wedge penetration on Shelby soil

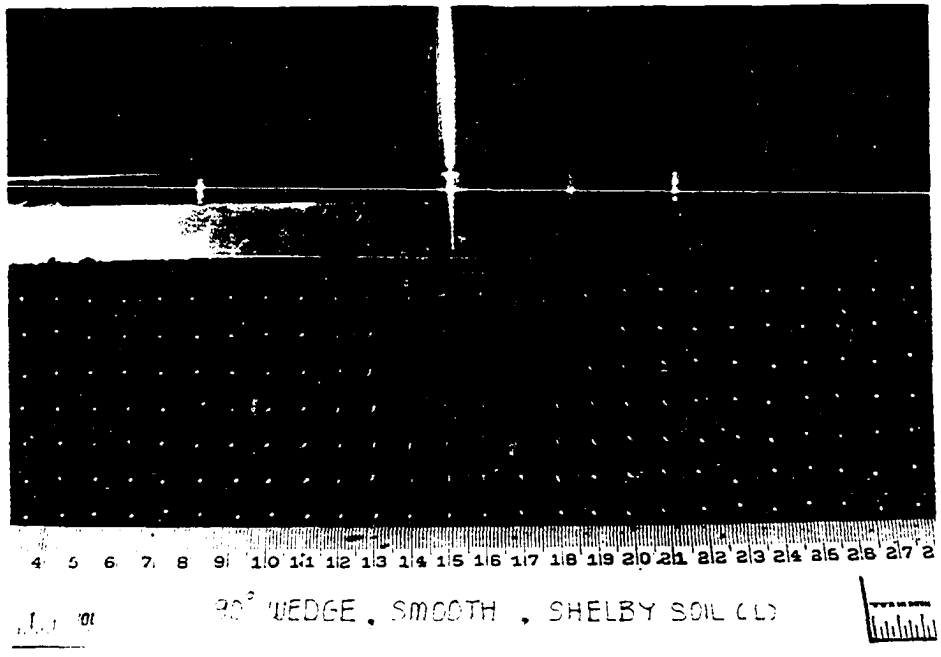

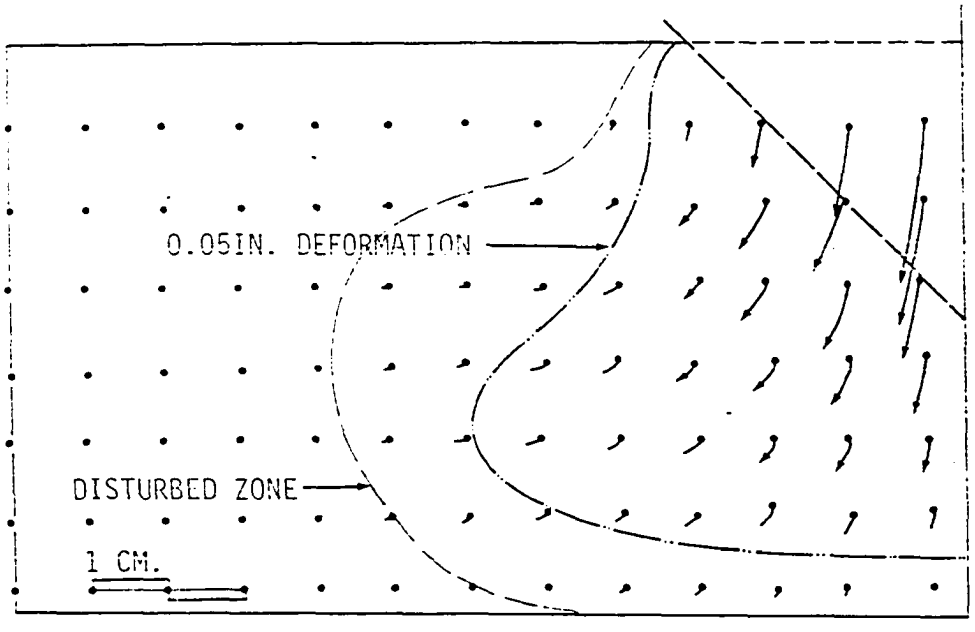

Figure 39. Soil deformation and vector field under 90° wedge penetration on Shelby soil

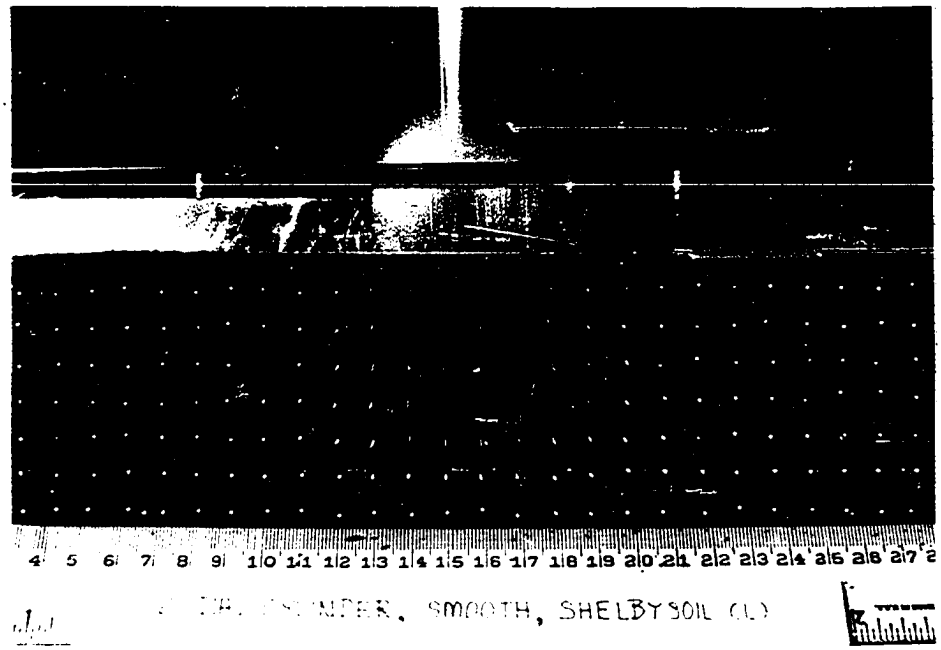

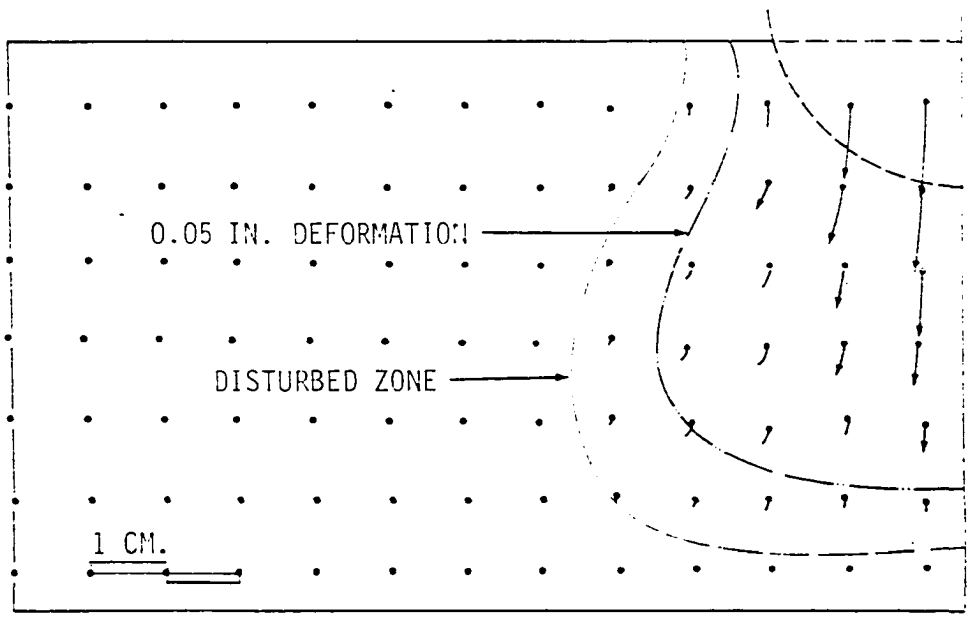

Figure 40. Soil deformation and vector field under 2.0 in. dia. cylinder penetration on Shelby soil

larger angle wedges favor the compaction mechanism since they move the soil downward and create bulb-like compacted zones shown in Figures 38 and 39. The cylinder penetrometer can be considered as a variable angle wedge, at low penetration corresponding to large angle wedge wherein compaction prevails, until the penetration is large enough that the curvature induces the shearing mechanism.

2. Degree of penetration

The degree or stage of penetration herein refers to the depth of penetration in relation to the geometry of penetrometer itself and the boundaries of soil media such as the depth of the sample. As the penetration progresses, soil within the compacted zone is denser, stiffer and higher in volumetric modulus so that further compaction requires higher energy than required to shear and rotate the soil upward, so the shearing mechanism will get its start. The example of Figure 41a for a 1 in. diameter cylinder shows the displacement of the sample at penetrations from 0.0 to 0.8 in., which mainly involved compaction of the soil beneath the penetrometer. As the penetration progressed from 0.8 to 1.6 in., Figure 41b., shearing occurred and a soil mass started to rotate upward with some lateral compaction just above the firm base.

A summary of observed disturbed zones at different stage of penetration is shown in Figures 42 and 43. The contours of the disturbed zone at the end of 0.4, 0.8, 1.2 and 1.6 in. penetration consist of both compacting and shearing zones. The compacted zones

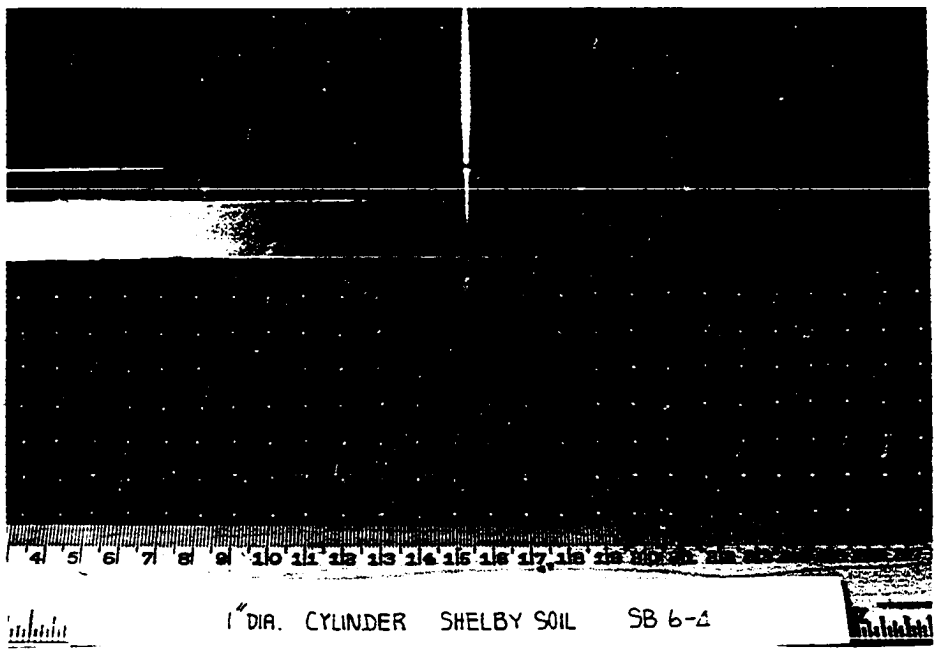

a)

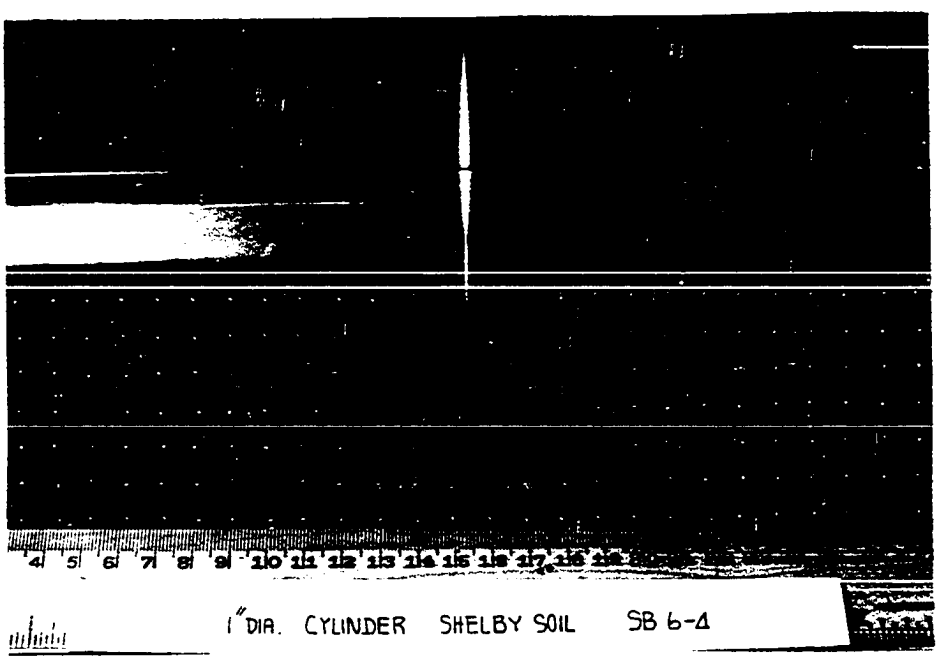

b)

Figure 41. Effect of degree of penetration on deformation mechanism on Shelby soil

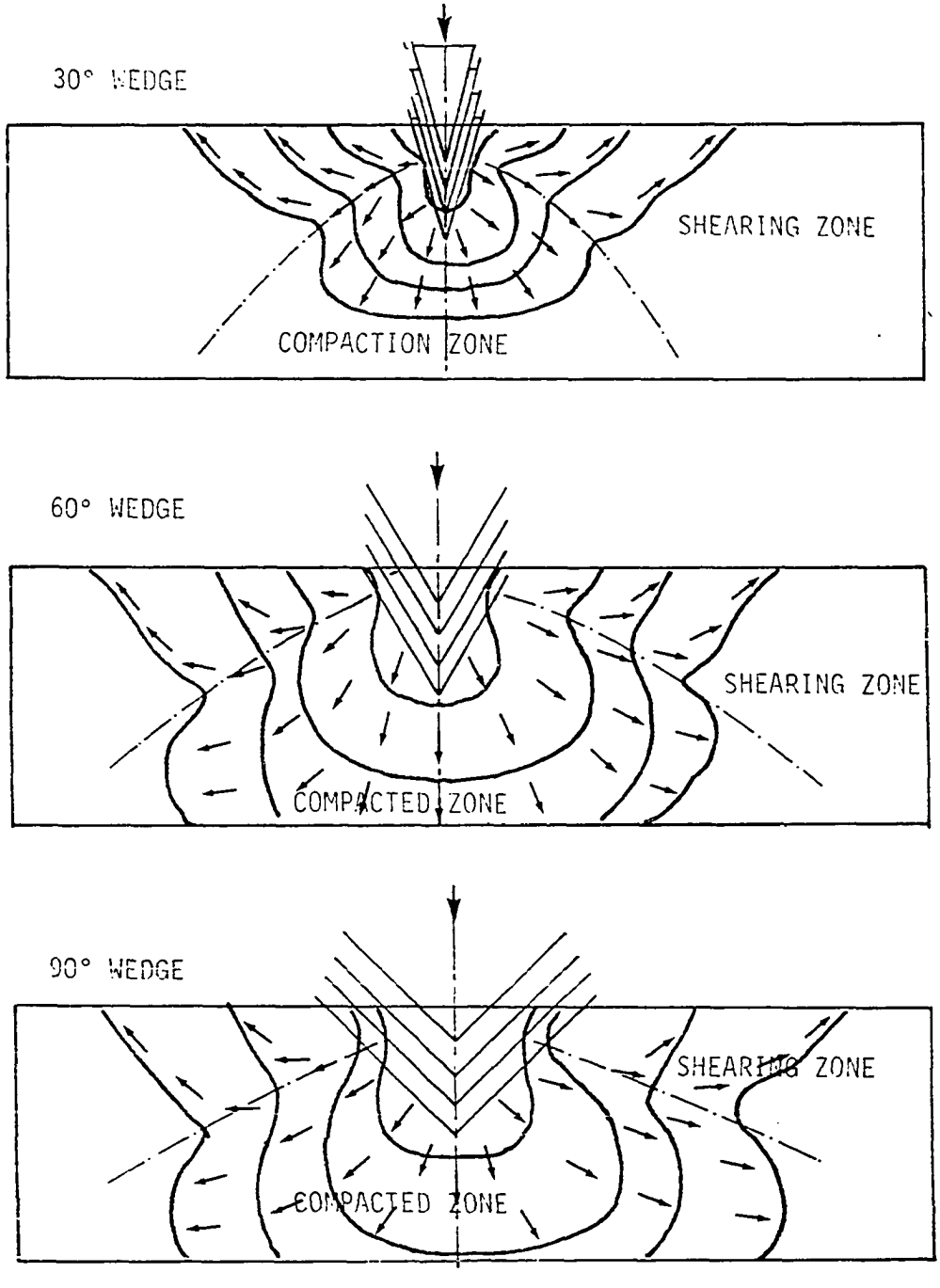

Figure 42. Progression of disturbed zones for 30°, 60° and 90° wedge penetrations on Shelby soil

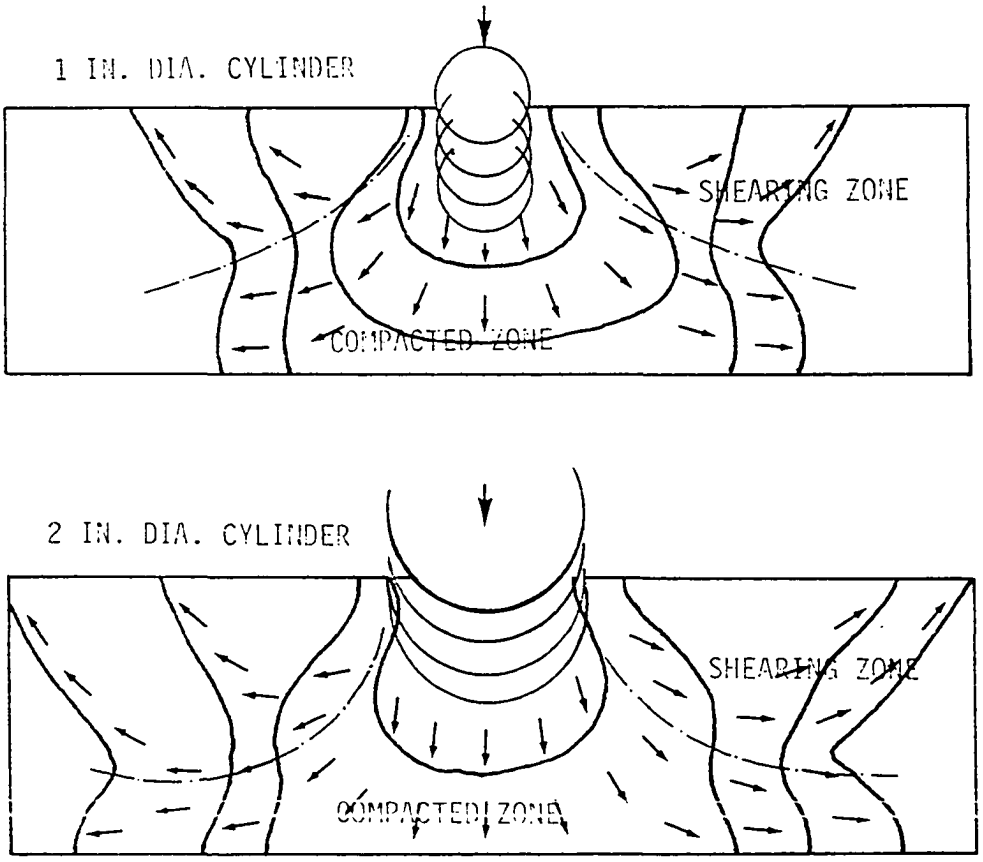

Figure 43 Progression of disturbed zones for 1.0 and 2.0 in. dia. cylinder penetrations on Shelby soil

progress below the dotted line as a dome shape below the wedge and bell-shaped below the cylinder. The compacted zones for larger wedge angles are broader and cover a larger area, and the shearing zones are smaller. The shearing zones for cylinders do not appear until the penetration is about 1.2 in.

3. Initial density and water content

The soil density characterizes the strength and compressibility of the soil. The effect of density is shown on Figure 44a and b. The higher density sample on Figure 44b has a larger disturbed zone than the lower density sample on Figure 44a. Also, a higher resisting force was observed on the high density sample, and the shearing mechanism occurred earlier at a smaller penetration, since the energy required to create further compaction is very high and exceeds the energy for shearing. This phenomenon has been recognized in relation to bearing capacity; stronger soil carries a high bearing capacity with low deformation until at a sufficiently high load general shear occurs. With a low density soil, incomplete or local shear occurs at the foundation edges, and deformation may become excessive due to a decrease in soil volume by compaction.

The initial water content also plays an important role in determining the penetration mechanism. Water in soil under load tends to weaken the soil by creating pore water pressure within the soil mass. The Terzaghi modification of Coulomb's equation (1) on an effective stress basis deducts pore pressure from the normal stress:

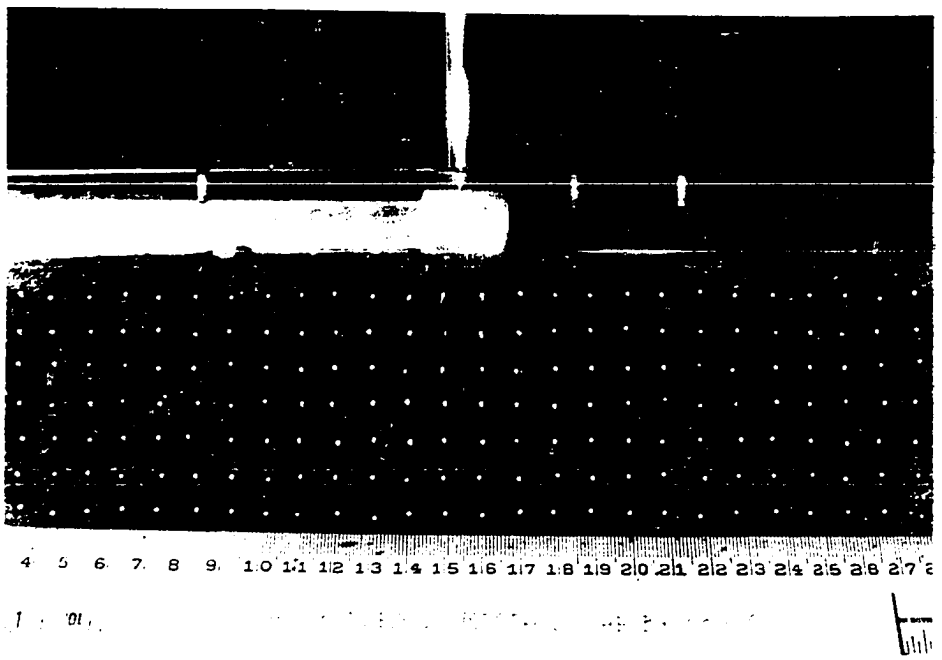

a)

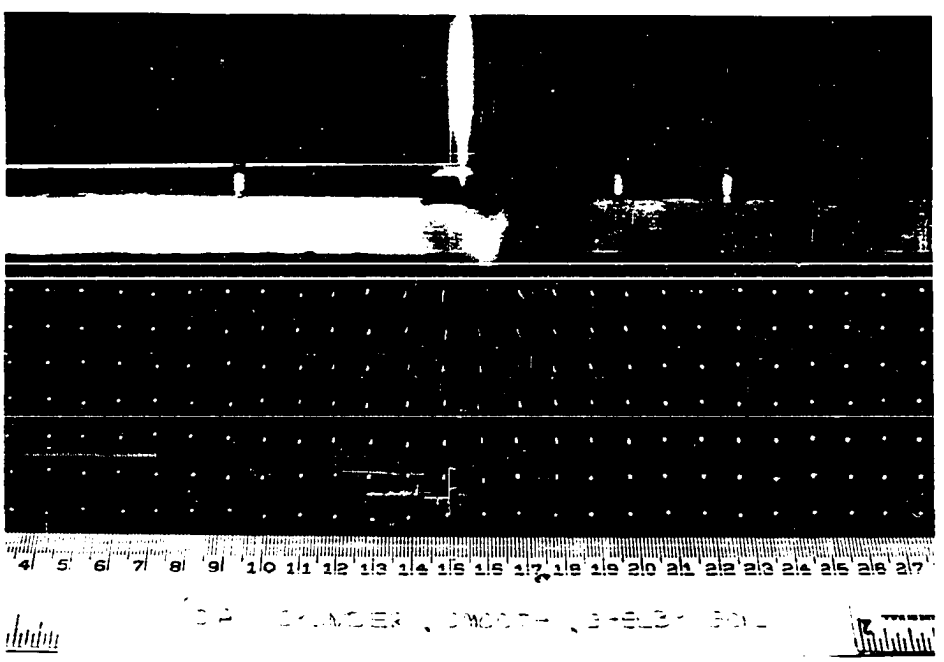

b)

Figure 44. Effect of initial density on deformation mechanism on Shelby soil

$$\tau' = c' + (\sigma - u) \tan \phi'$$

where

τ' = effective shearing strength

c' = effective cohesion

σ = total normal stress

u = pore pressure

ϕ' = effective angle of internal friction

When pore pressure increases it is obvious that the shearing strength must decrease. In the experiments of Figure 45, the soil samples have about the same dry densities but the sample of Figure 45a and Figure 45b have 15.6% and 23.2% water contents respectively. The wetter sample shows a larger shearing zone and a smaller compacted zone.

Another effect of water in soil pores is to restrict the volume of air available to be expelled by compaction. Thus a wet soil soon becomes saturated upon compaction, after which further increasing loads are partially carried by pore pressure, decreasing shear strength. A saturated soil is relatively incompressible, in that no more compaction can occur unless the water can dissipate out of the soil mass; this requires a relatively long time and is known as "consolidation".

The degree of saturation is an expression of the effects of both initial density and water content, and is defined as the ratio of volume of water to the volume of total voids within the soil mass,

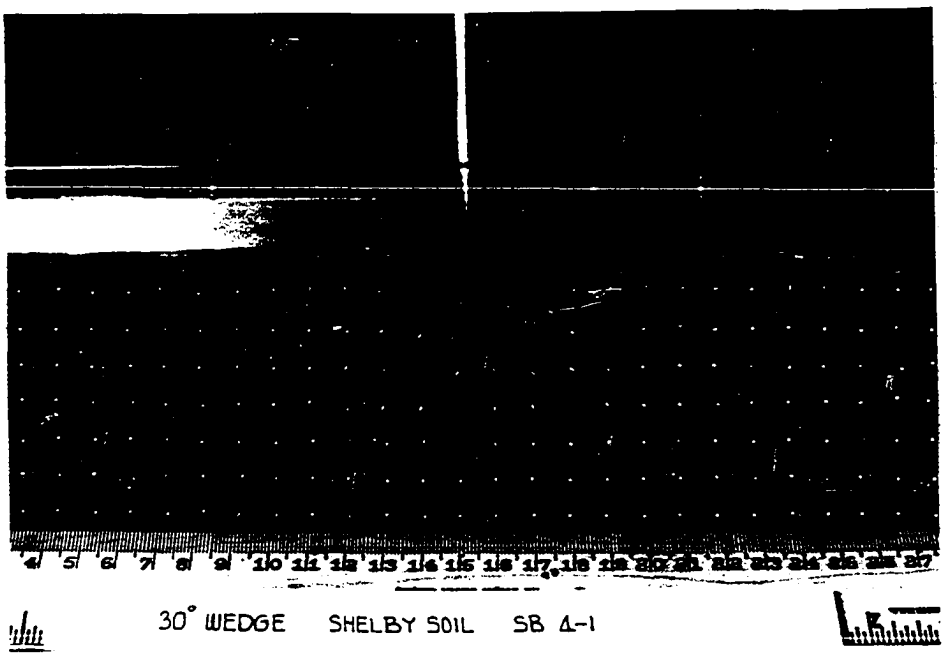

a)

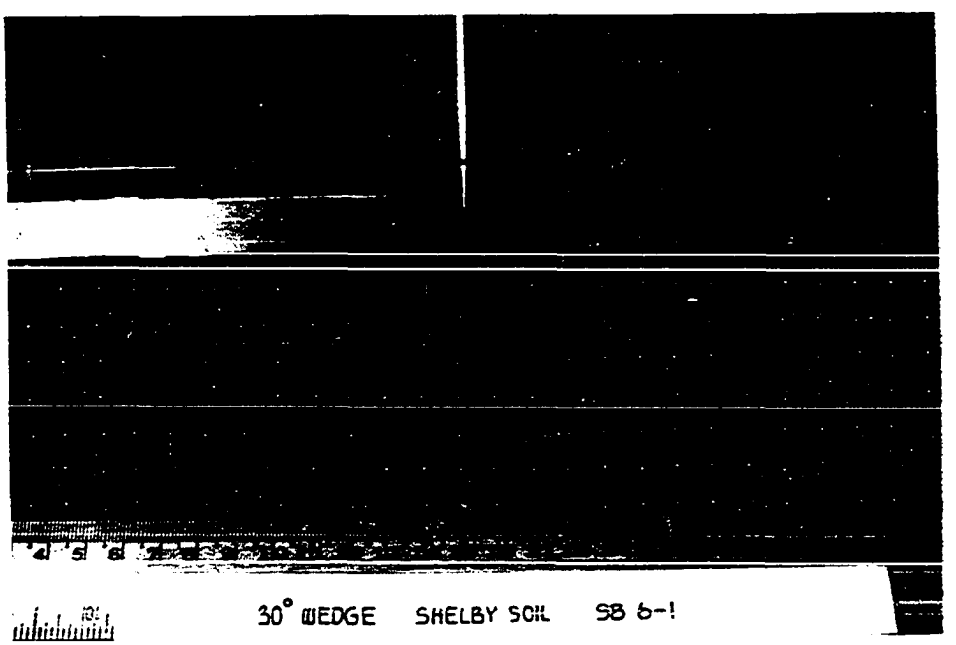

b)

Figure 45. Effect of initial water content on deformation mechanism on Shelby soil

and relates to dry density and water content as;

$$S = \frac{w.G.\ \gamma_d}{G.\gamma_\omega - \gamma_d}$$

where

S = degree of saturation

w = water content

γ_d = dry density

γ_w = water density

G = soil specific gravity.

For the same soil, as the degree of saturation increases the shearing mechanism during penetration is increased.

Force-penetration relation

As has been mentioned before, the penetration resistance curve describes the relation between resisting force and penetration. The penetration curves on Shelby soil were obtained from two different tests, namely the displacement model test and the Proctor sample test. The wedges and cylinders were penetrated on displacement model samples where the movements of the soil mass were observed and the resisting forces were recorded simultaneously, whereas the cones and spheres were tested on Proctor samples at different water contents, and only the resisting forces vs. penetration were recorded.

Wedge The typical wedge penetration curves on Shelby soil are

presented in Figure 46. The curves seem to show two portions of straight lines; the first portion between 0.0 to between 0.7 and 1.0 in. is called "free penetration", since the disturbed zones do not extend down to the base of penetration box. The second portion when penetration goes deeper is called "confined penetration", and has a higher slope because of the confining effect of the base.

The free penetration curves were used to evaluate soil parameters by the method described in the theoretical analysis. An inconsistency of the data was encountered in that more than half of the data show either negative or very high "λ" values in equation (47), as the arguments of "ln" in the denominator are close to unity. This phenomenon is believed to be the result of compaction that changes the soil properties. Regardless of the compaction effect, the parameters that could be evaluated are presented in Table 6. The average values of c and ϕ are plotted on Figure 47 along with more reliable data obtained from the K-Test and reported by Lutenegger (23).

Since the evidences show that compaction occurs during penetration of unsaturated soil, this creates a complex situation that is not well-approximated by analyzing the penetration as a shearing mechanism alone. It is therefore worthwhile to study the phenomena, and the effects of compaction on penetration tests. According to Figures 42 and 43 the compacted zones exhibit certain geometries when the shearing mechanism gets started after a certain degree of penetration. On Figure 48 are shown four successive stages of penetration of the

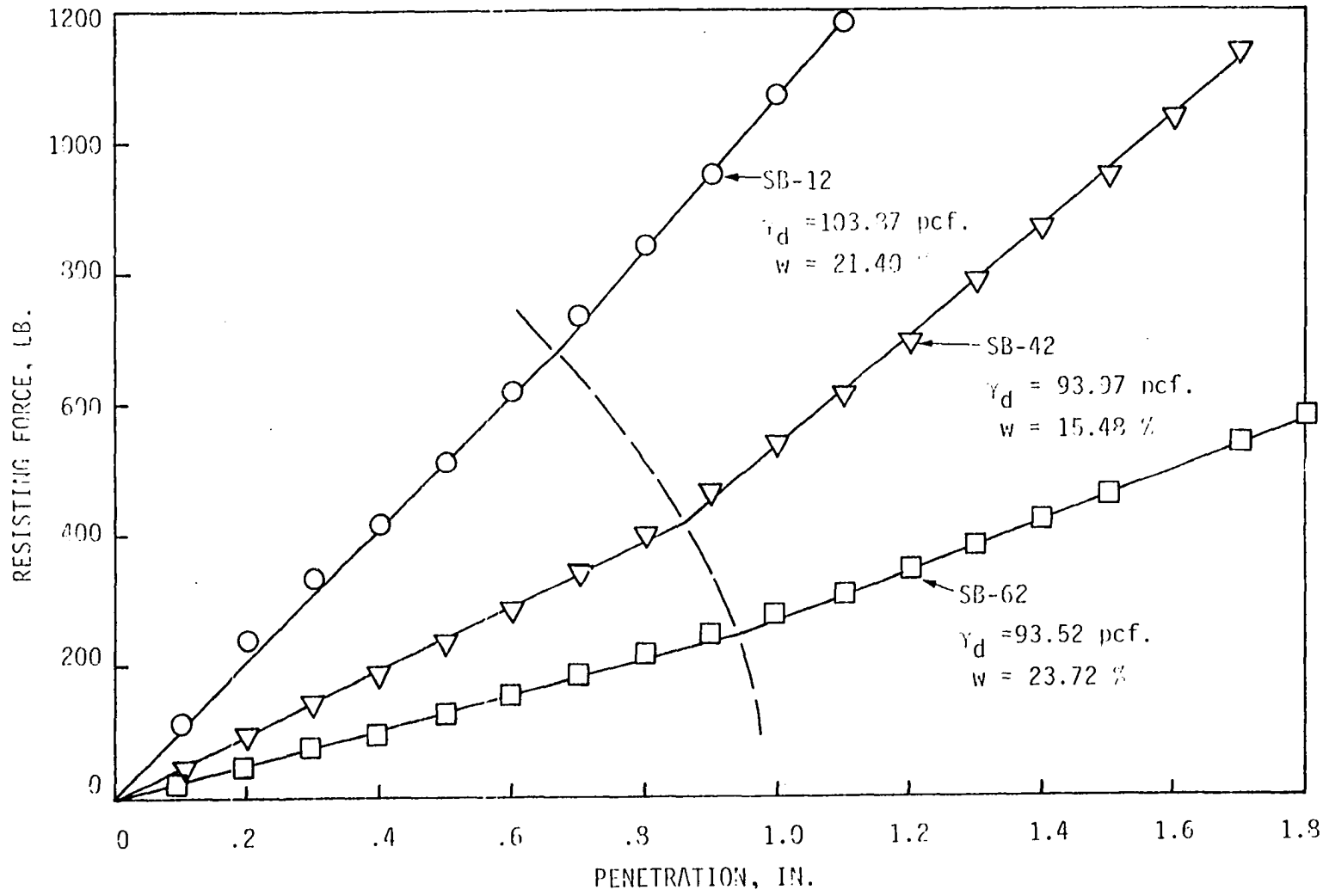

Figure 46. Typical penetration curves for wedges on Shelby soil

Table 6. Strength parameters for Shelby soil by wedge penetration

Penetration (in.)	SB 11-12 c (psi)	SB 11-12 ϕ (degree)	SB 41-43 c (psi)	SB 41-43 ϕ (degree)	SB 61-62 c (psi)	SB 61-62 ϕ (degree)
0.2	19.1	31.2	13.2	28.3	N.D.[a]	N.D.
0.4	23.1	24.1	8.0	37.2	N.D.	N.D.
0.6	27.9	24.5	7.9	37.5	N.D.	N.D.
0.8	16.9	31.2	8.9	39.5	N.D.	N.D.
1.0	17.6	30.8	9.3	40.3	44.0	12.5
1.2	18.9	29.2	-	-	36.2	19.2
1.4	20.0	28.2	-	-	30.4	25.3
average[b]	20.73	28.00	8.53	38.63	33.30	22.25
dry density	107.1 pcf.		93.6 pcf.		93.2 pcf	
water content	18.0 %		15.6 %		23.3 %	

[a] N.D. indicates the data can not determine due to large λ.

[b] Discard the quantity on the first penetration.

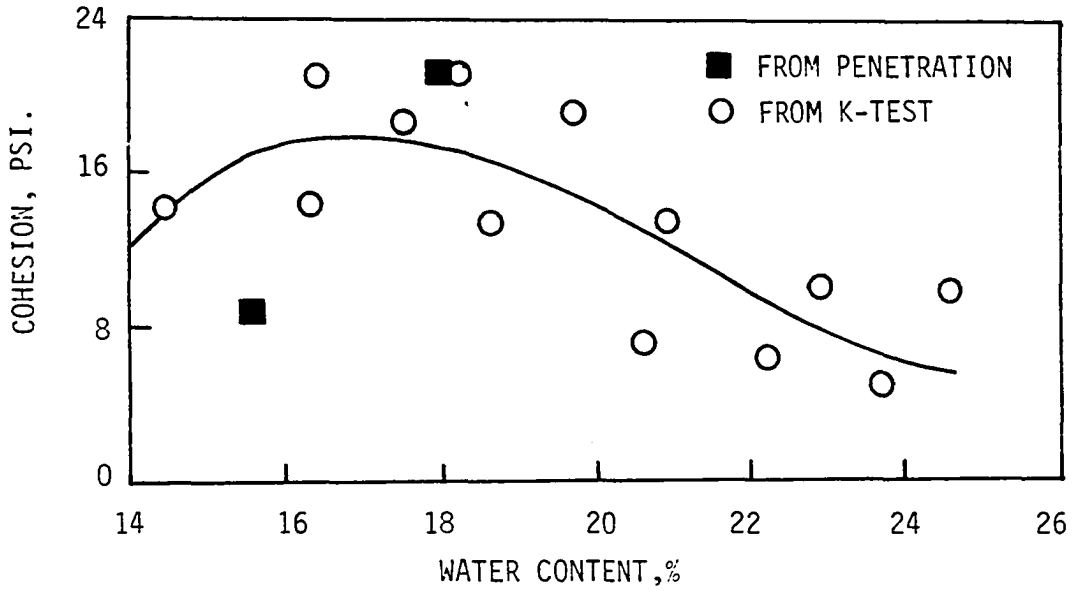

a)

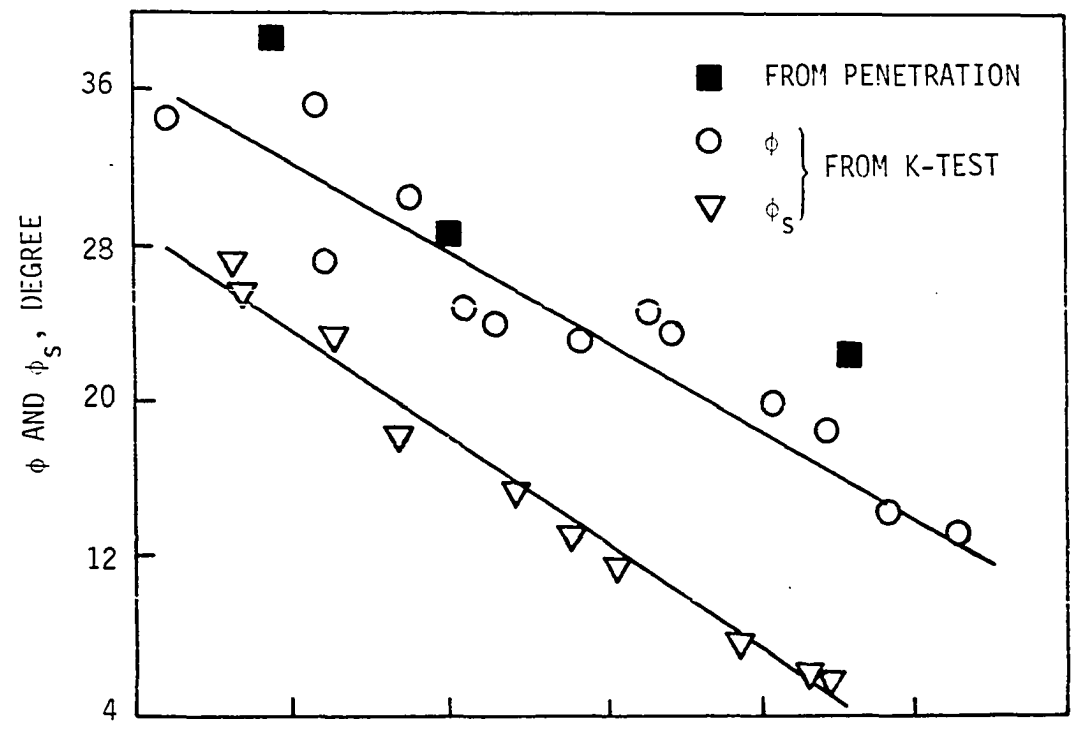

b)

Figure 47. Strength parameters for Shelby soil from K-Test

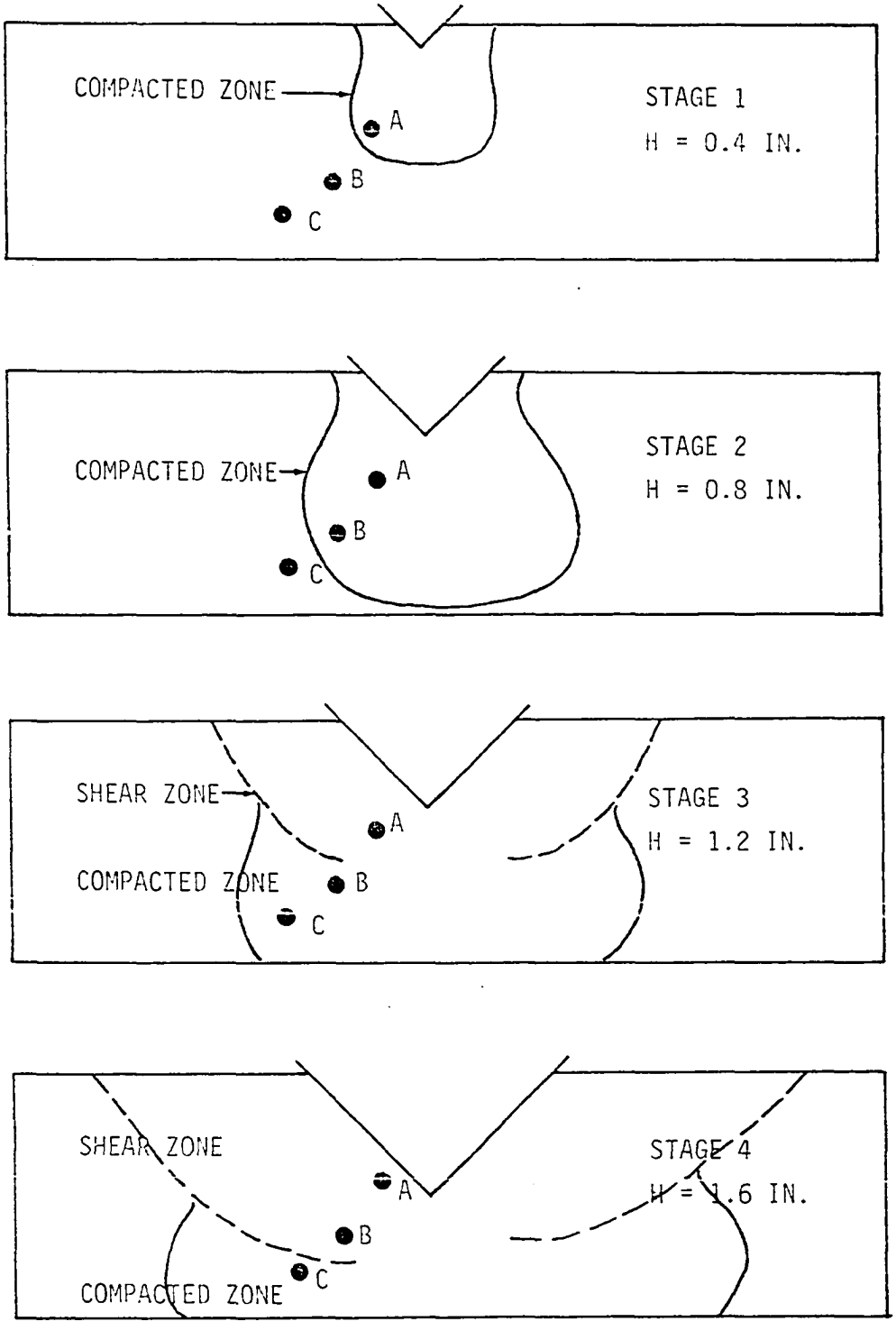

Figure 48. Progression of compacting and shearing zones on Shelby soil

90° wedge. The disturbed zones in the first two stages are compacted zones which then develop into combined shearing and compaction zones in stages 3 and 4. Points A, B and C are selected so that the stresses at various parts of the sample calculated by the previous theories can be compared to actual mechanisms observed at each point.

Table 7. Summary of actual mechanisms at various stages of penetration

Points	Mechanism During Penetration			
	Stage 1	Stage 2	Stage 3	Stage 4
A	Comp.[a]	Comp.	Shear[b]	Shear
B	Undis.[c]	Comp.	Comp.	Shear
C	Undis.	Undis.	Comp.	Comp.

The stress path method proposed by Lambe and Whitman (22) was used to calculate the stress at each point at each stage. Principal stresses were calculated according to elastic solutions under a semi-infinite mass and for an elastic medium over a rigid base, by assuming an equivalent uniform strip load at the surface over the penetrated width of the wedge. The stress paths for points A, B and C for four

[a] Compaction, indicating coordinate of the p-q values below the K_f line

[b] Shearing, indicating coordinate of p-q values on the K_f line

[c] Undisturbed zone.

stages of penetration are presented in Figure 49 along with an initial K_f line, K_{f1}. If the soil gets stronger during compaction then K_f line should be translocated upward. Also, any location in the soil that does not develop the shearing mechanism must have p-q stress coordinates below the developed K_f line. For example at point A, stages 1 and 2 present a compaction mechanism so the p-q values must be below the K_f line of stages 1 and 2, whereas the shearing mechanism starts at stage 3, when p-q value should be on K_f line of stage 3. From similar arguments p-q value at point B in stage 4 should be on the K_f line of stage 4. Based on this analysis the K_f lines of each stage of penetration can be estimated.

The shape of the compacted zone can be approximated by an elastic solution. Figure 50 and 51 show the p-q values of the various grid points under 60° and 90° wedges at 1.0 in. penetration. The wedge loads were transformed to equivalent uniform surface strip loads, and again based on an elastic solution the p-q values were calculated at each grid point. For a grid point where p-q value fall above the K_f line, either soil in that region must be in a failure state or has been compacted such that the K_f line is raised to a new position. At this penetration the experiment shows that compaction dominates in that region, and the compacted zone encloses points above the initial K_f line.

These ideas for estimating the K_f line from the geometry and stresses of the compacted zone may be criticized from their base in

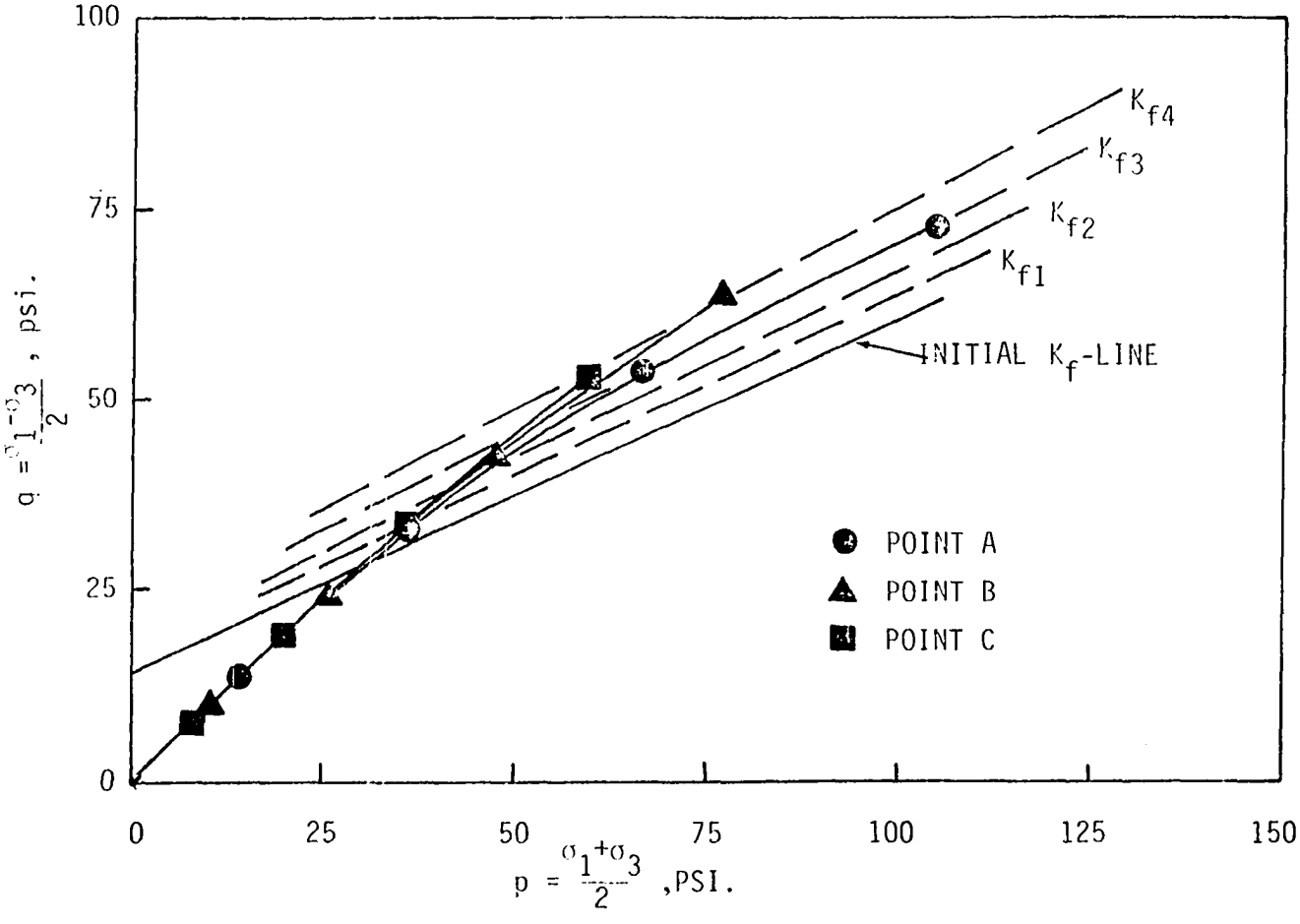

Figure 49. Stress paths during penetration on Shelby soil

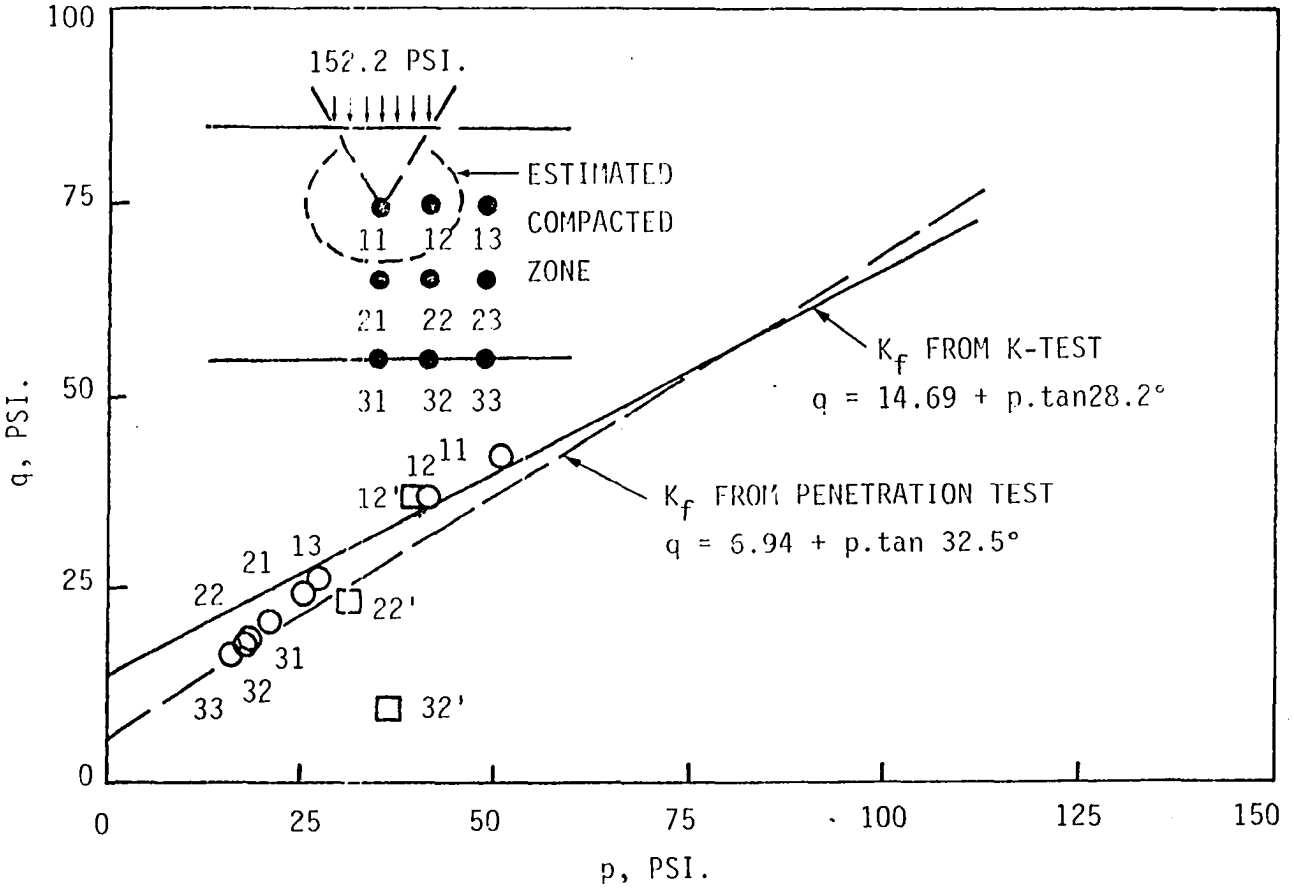

Figure 50. Stress condition under 60° wedge penetration on Shelby soil

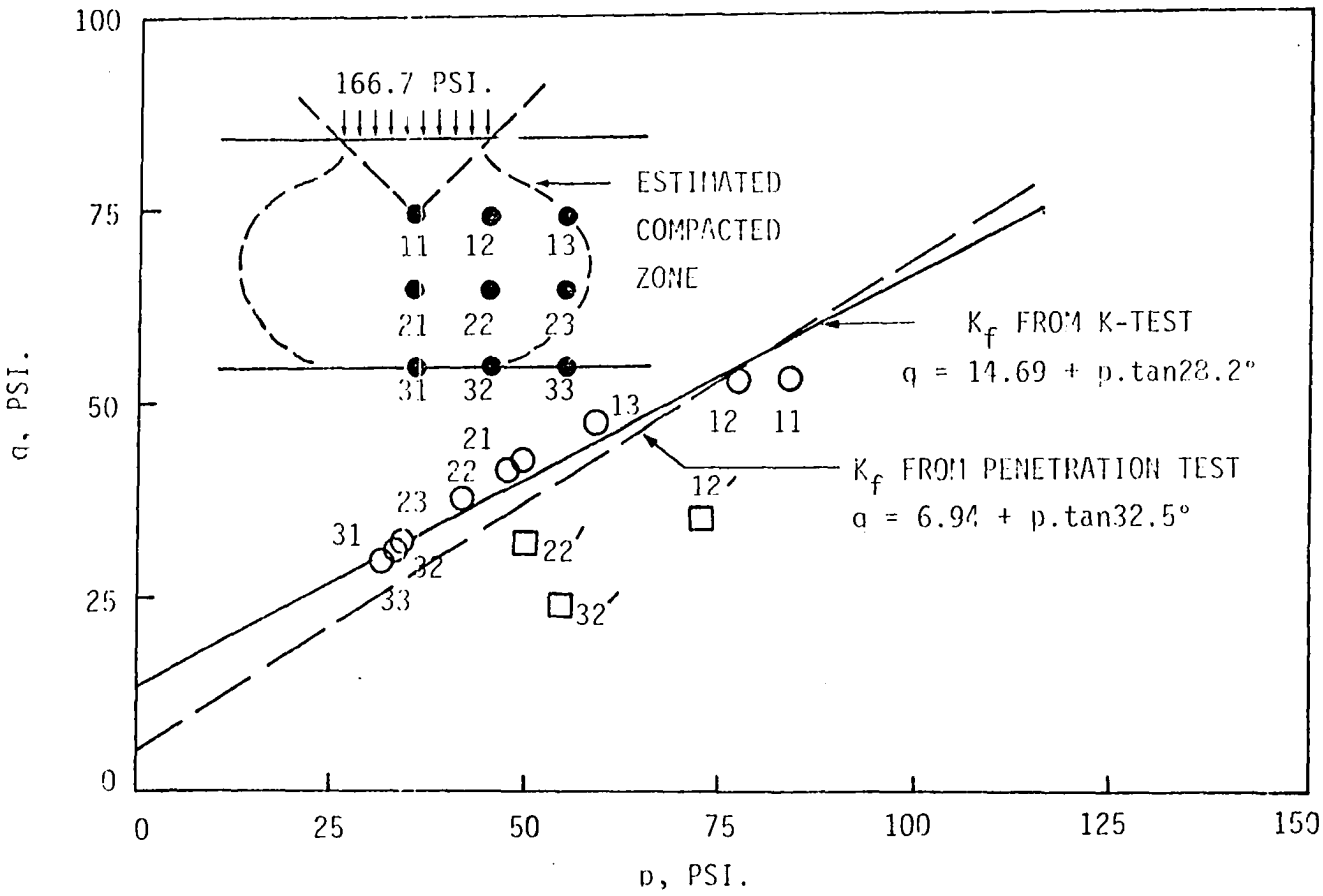

Figure 51. Stress condition under 90° wedge penetration on Shelby soil

elastic theory. On the other hand elastic theory does appear appropriate and has been extensively applied to consolidating soils that gain strength through an increase in density. Elastic assumptions are violated when the soil shears, and elastic theory then is no longer valid. This approach also may be very useful in developing field compaction equipment. For example, the most effective shape for a tamping foot and the best compactive pressure should be selected to maximize the compacted zone and minimize the possibility for creating general shear failure, which weakens the soil and is referred to as overcompaction. The strength properties and size of compacted zone can also be estimated beforehand by the stress path method.

Cylinder The typical penetration curves for cylinder penetration are shown in Figure 52. The theoretical curves using soil properties from the K-Test generally predict higher resisting forces, especially for dry soil. As previously discussed, in dry soil, compaction and elastic compressibility should have more effect than in wet soil. That is, whenever the energy required for compaction is lower than the energy required for shearing the soil will be compressed. On the other hand with wet soil the strength parameters are lower, and pore pressure tends to develop earlier during penetration, lowering the energy required for shearing. This concept leads to yet another approach to compaction vs. shearing, that of minimizing internal energy. The applied external energy is the resisting force

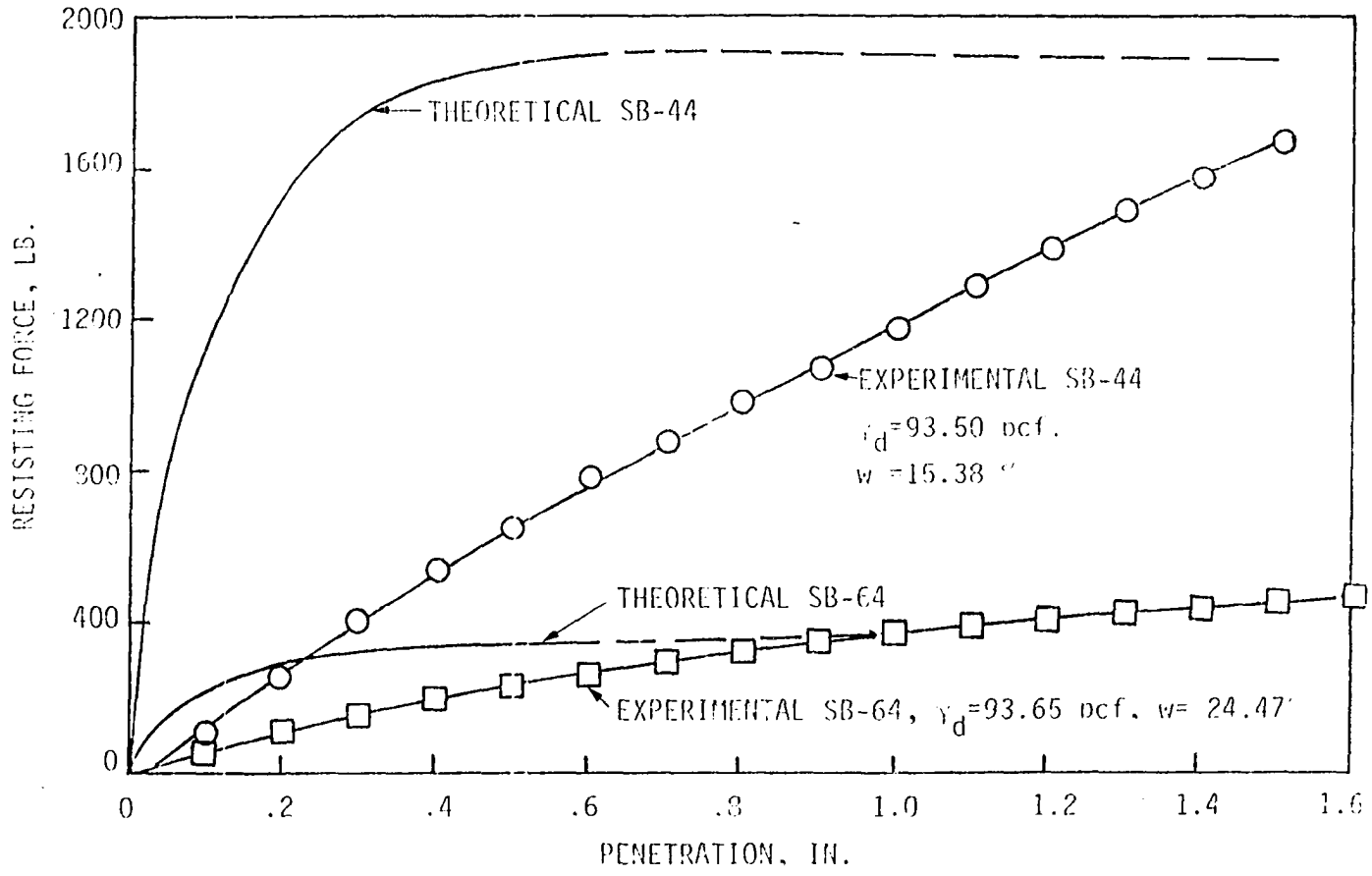

Figure 52. Typical penetration curves for cylinder penetration on Shelby soil

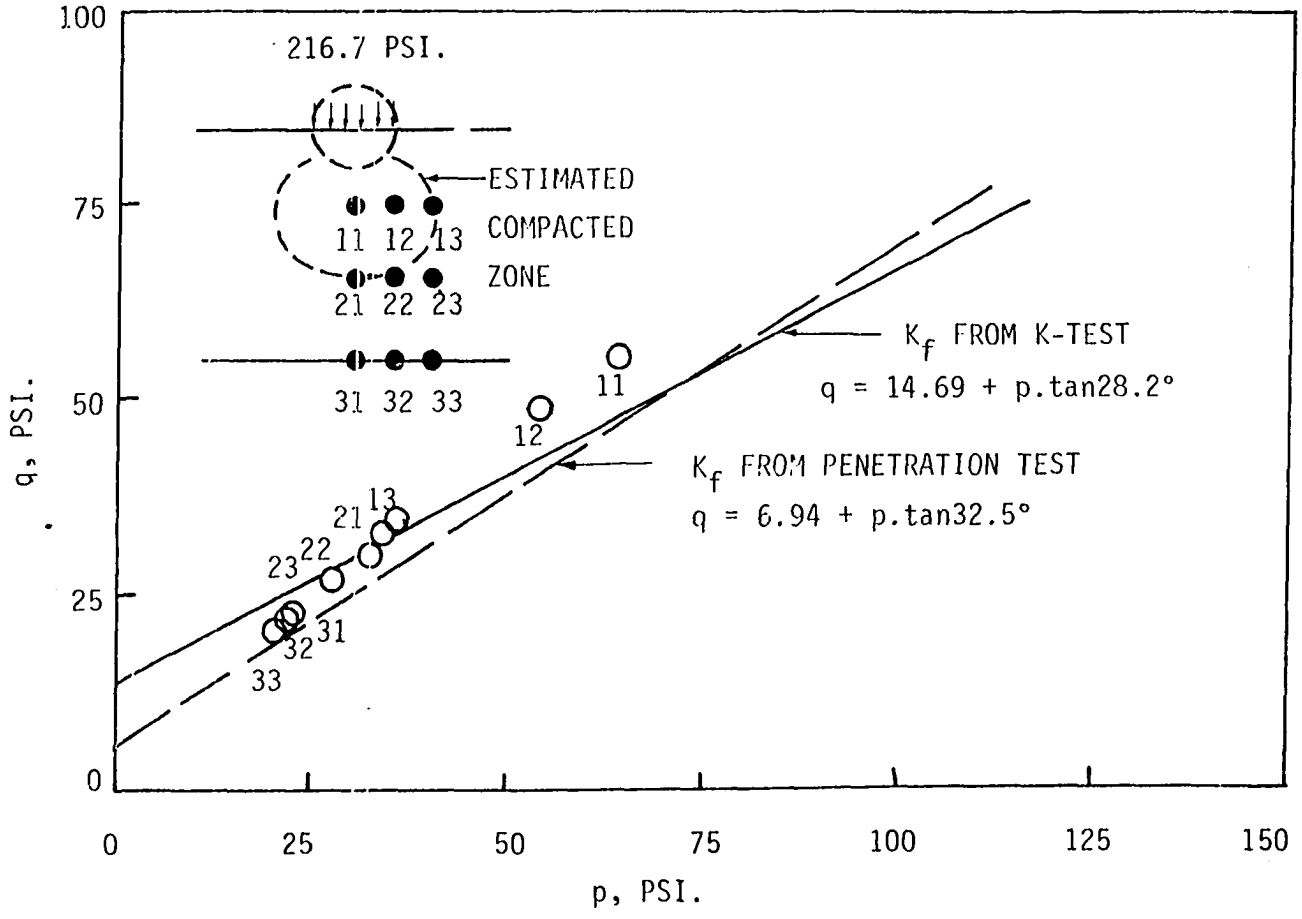

Figure 53. Stress condition under 1.0 in. dia. cylinder on Shelby soil

times the depth of penetration, and should equal the total internal energy within soil mass due to deformation of the soil by both compaction and shearing:

$$F.H = \Sigma\ (\tau.\delta.\Delta V_s + \sigma.p.\ \Delta V_c)$$

where

F = resisting force on penetrometer

H = depth of penetration

τ = shearing stress

δ = shearing strain

σ = normal stress

p = normal strain

V_s = volume of soil within shear zone

V_c = volume of soil within compaction zone.

The most effective technique to solve this energy equation seems to be a numerical method such as the finite element method, which will be discussed in detail later.

Typical stress conditions under a cylinder are shown in Figure 53, by means of the same technique as described for wedge.

Cone The penetration curves for cones were obtained from Proctor samples, and show the same pattern as described for modeling clay. The transformed curves of square root of resisting force versus penetration are straight lines, as illustrated in Figure 54. The slope of the transformed curve is called "cone slope index" and will be used to

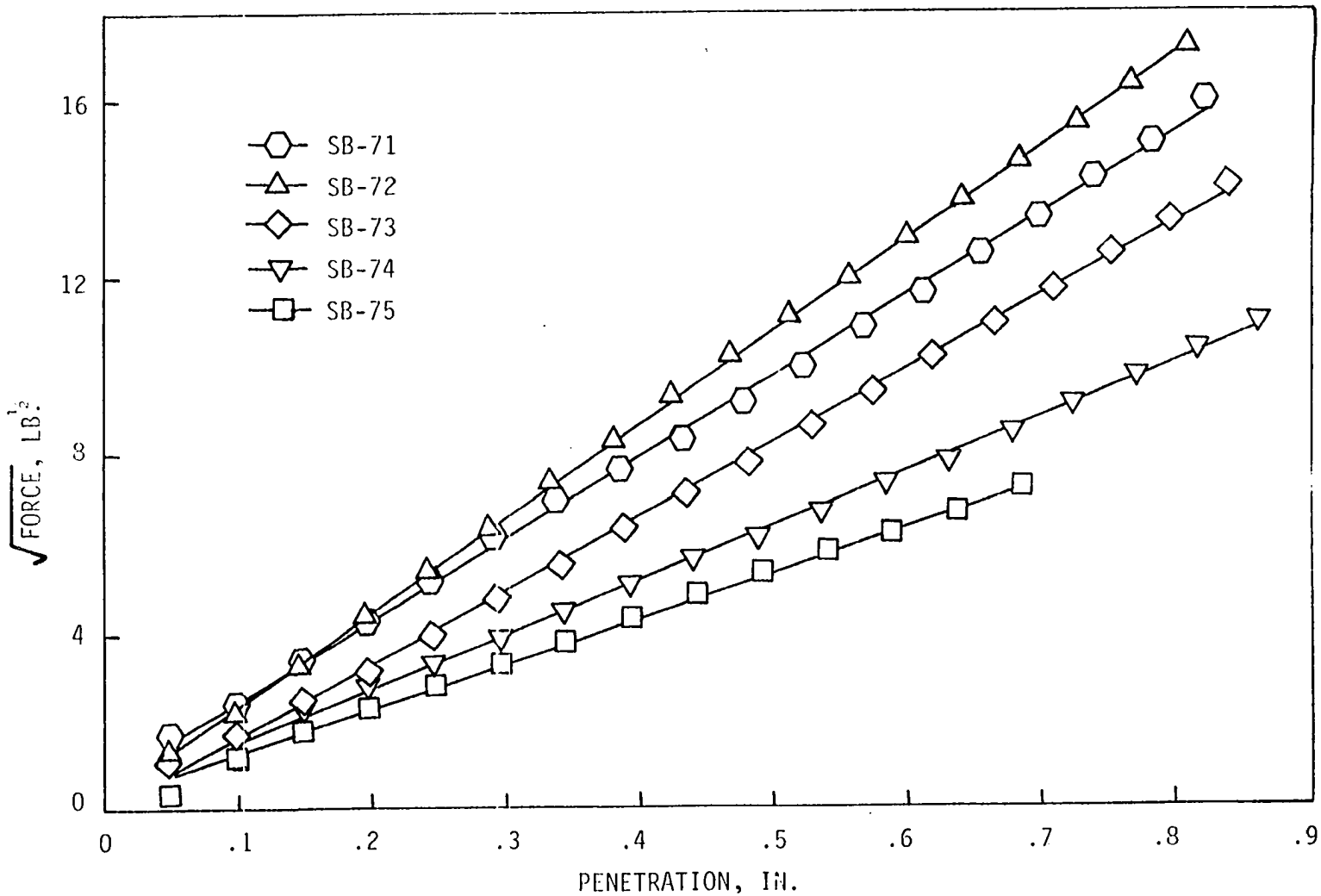

Figure 54. Transformed penetration curves for 60° cone on Shelby soil

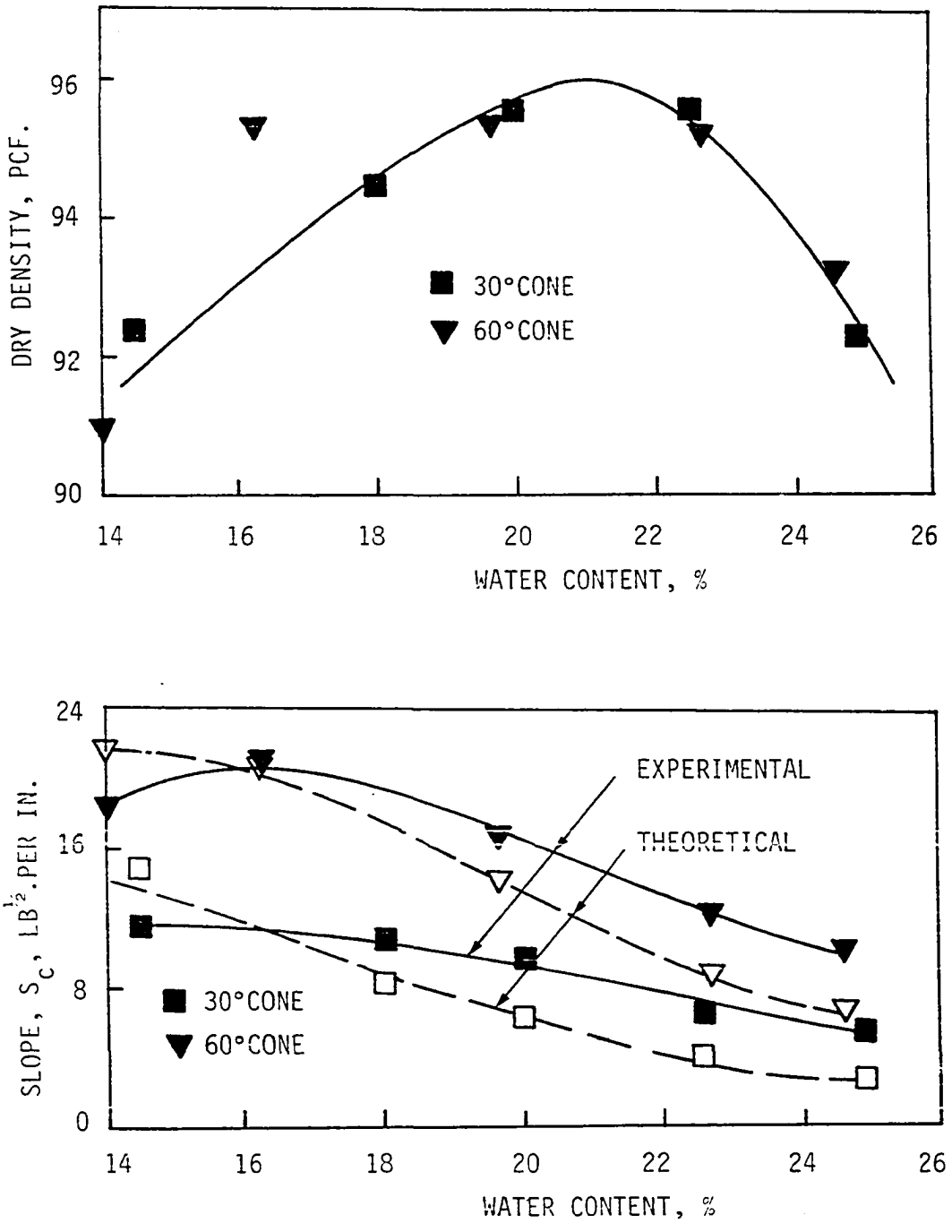

Figure 55. Cone slope indices versus water content on Shelby soil

represent penetration properties of each sample.

Figure 55 show the variations of cone slope indices for 30° and 60° cones, versus water content on Shelby soil. The corresponding theoretical curves were calculated from Equation (4) using the strength properties from K-Test shown on Figure 47. Generally the curves show similar patterns, with relatively higher values from experimental data as water content increased.

Sphere

Figure 56 shows penetration curves of 1 in. diameter sphere on Shelby soil prepared at different water contents. The curves can be represented by straight lines when the penetration is less than 0.3 in., or 30% of sphere diameter. The slope of the curves is plotted versus water content as shown in Figure 57. The theoretical values are the slope of regression line calculated from modified equation (44) and the strength parameters from the K-Test. It can be seen that the experimental data show lower values than the theoretical ones, which is the reverse of the case for cone penetration data, Figure 55. This may be because the shape of the cone induces the soil to shear at the beginning stage of penetration, whereas a sphere induces compaction and keeps the stage of stress in the elastic range longer. From the displacement model test, the shearing mechanism with a sphere will start at a penetration of about 25 to 35 percent of its diameter. However, as the soil approaches a saturated condition, pore pressure starts to develop and the shearing mechanism is induced

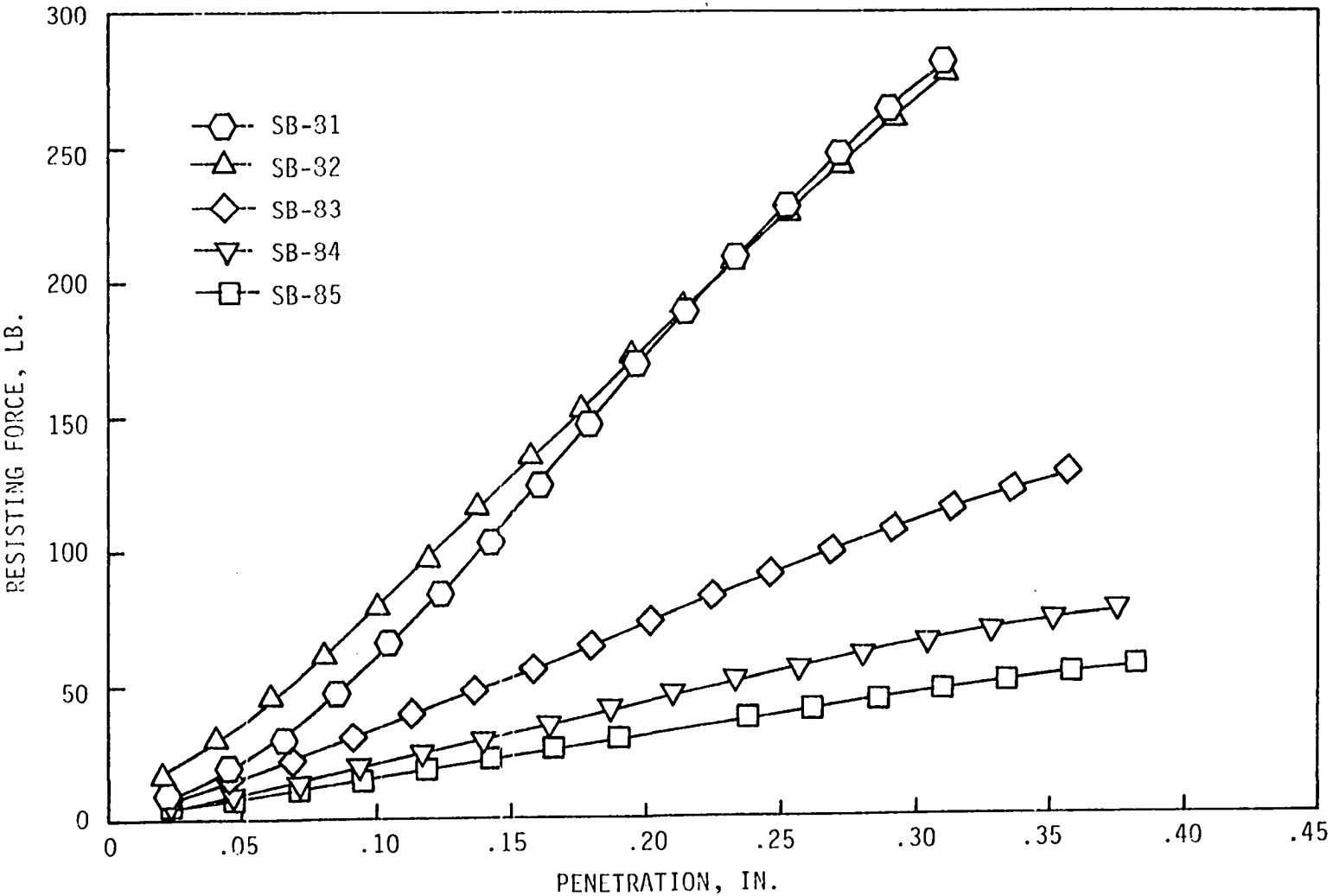

Figure 56. Typical penetration curves for sphere on Shelby soil

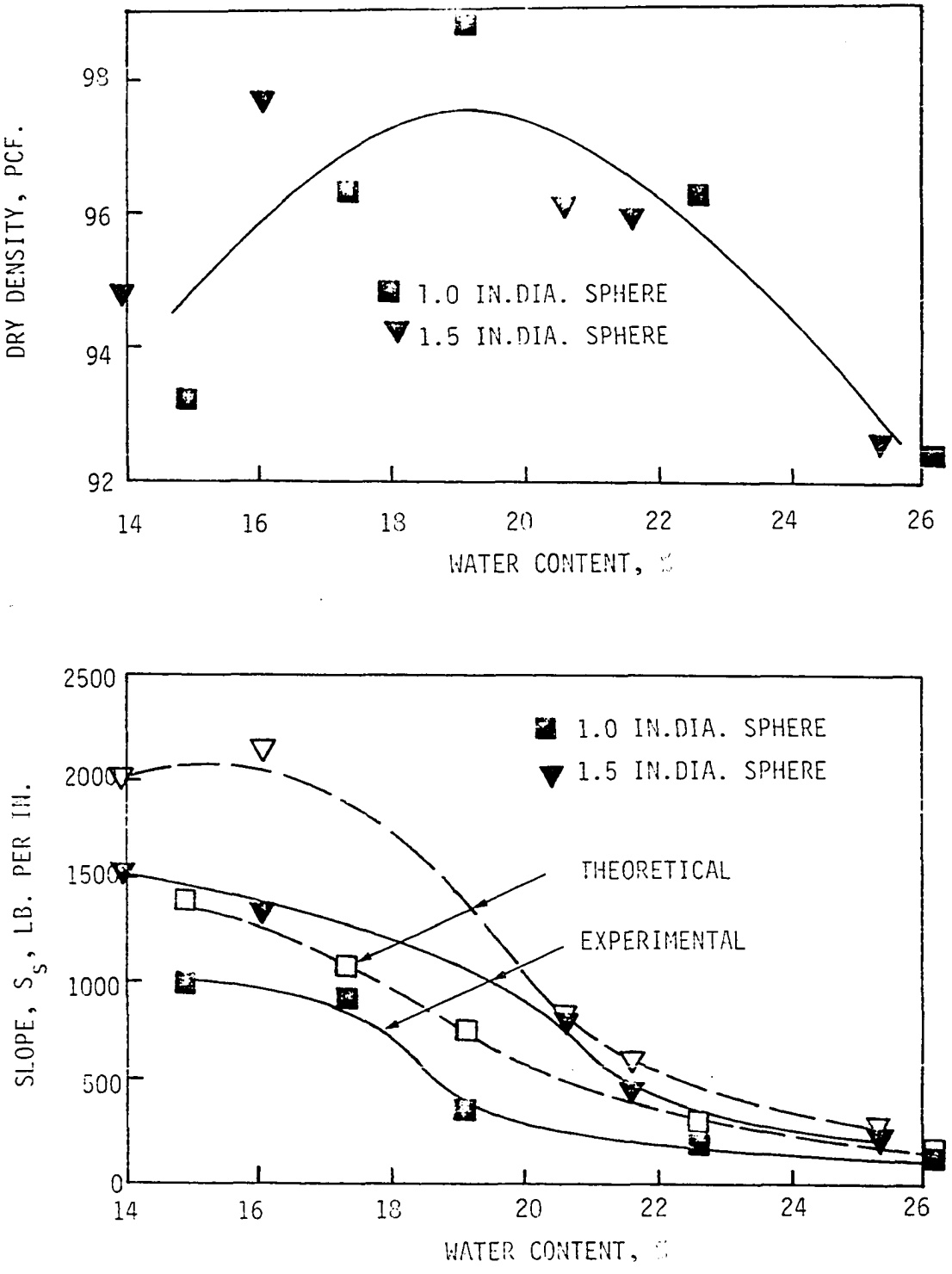

Figure 57. Sphere slope indices versus water content on Shelby soil

at the earlier stage of penetration. Figure 57 shows that theoretical and experimental curves approach each other on the wet side of optimum water content.

Penetration on Sand

Penetration of a purely cohesionless soil is beyond the scope of this study, but some preliminary investigations by displacement model tests were done to support the understanding of silty soil and sandy loam. The theory developed for cohesive soil brings cohesion in as a multiplication factor for all equations; hence for cohesionless soil the theoretical resisting force will become zero. The experiments gave a stick-slip type of resisting force, in that as soon as the sand particles started to shear the resisting force rapidly dropped to zero. The equipment set up for the displacement model test was not capable of recording this type of force, so no force-penetration test data will be presented.

Figures 58 and 59 show the vector fields from the displacement model test on 60° wedge and a 2" diameter cylinder in sand. No compaction occurred since the sand samples were dense as prepared, and only shearing movements were observed. In general, the amount of movement is larger than that of modeling clay or Shelby soil because no volumetric compression occurred--in fact there was volumetric expansion due to dilatancy. The failure boundary is clearly established as we can see on Figure 60. The total movements of penetration

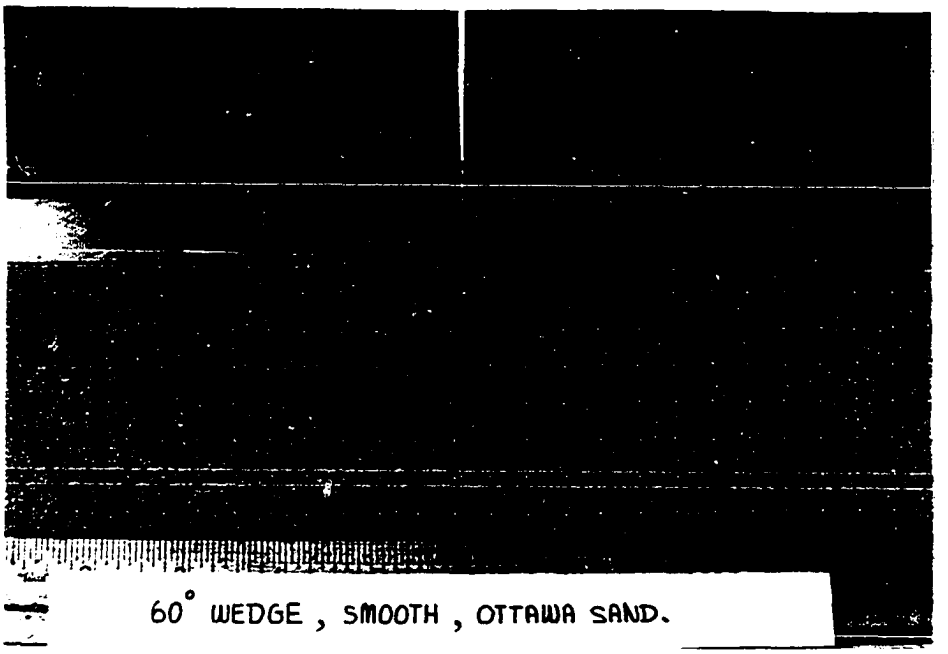

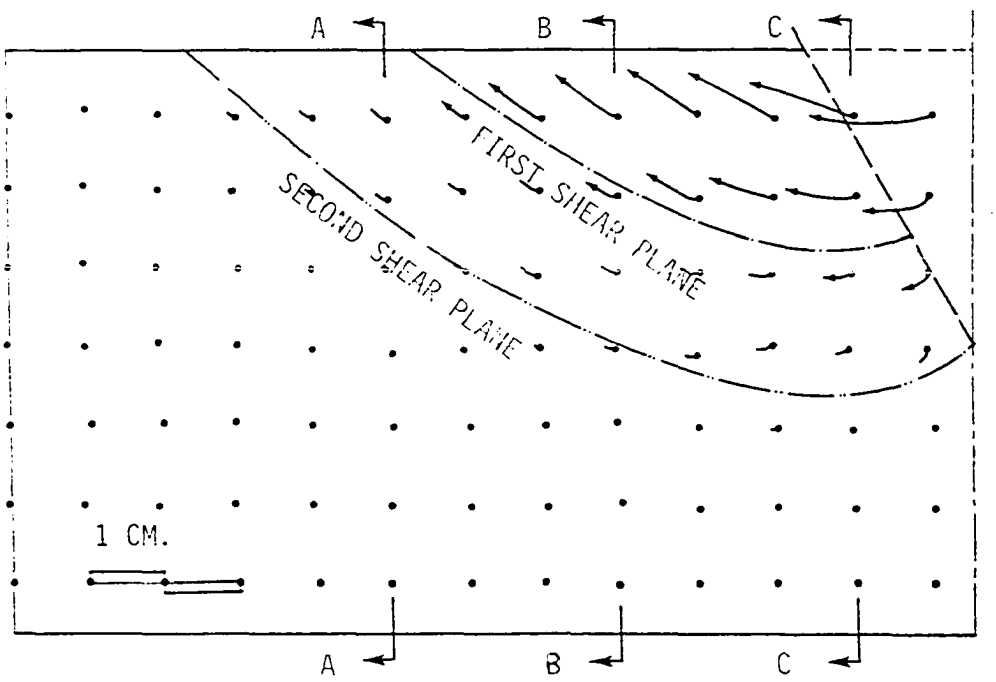

Figure 58. Soil deformation and vector field under 60° wedge penetration on Ottawa sand

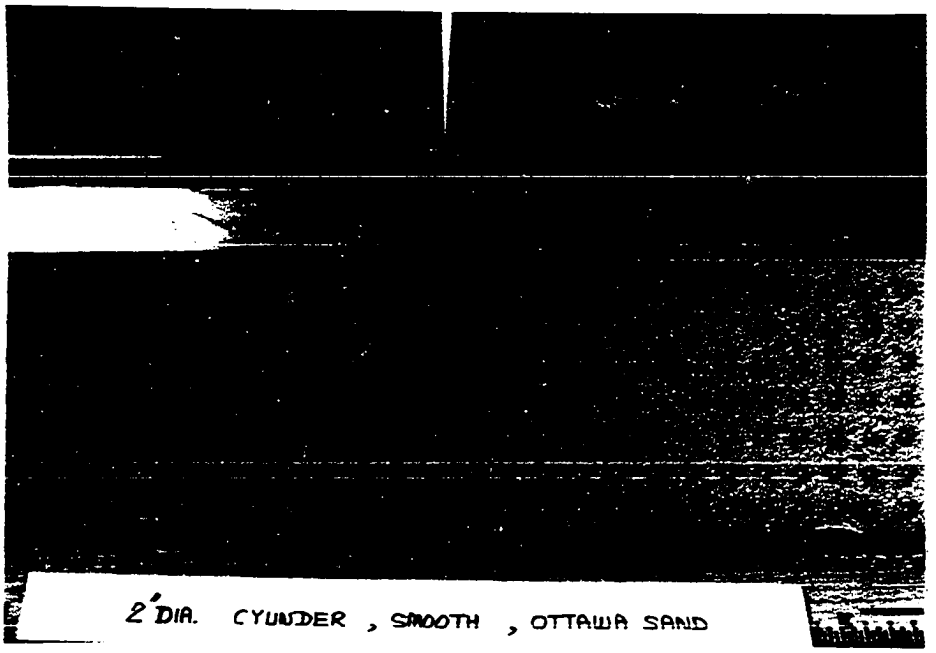

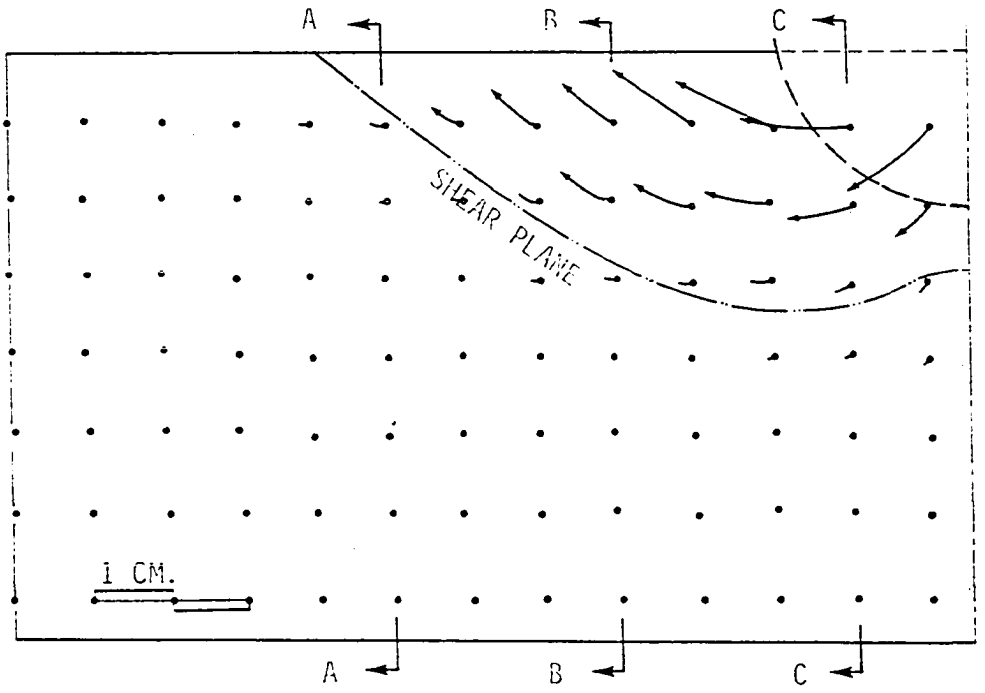

Figure 59. Soil deformation and vector field under 2.0 in. dia. cylinder penetration on Ottawa sand

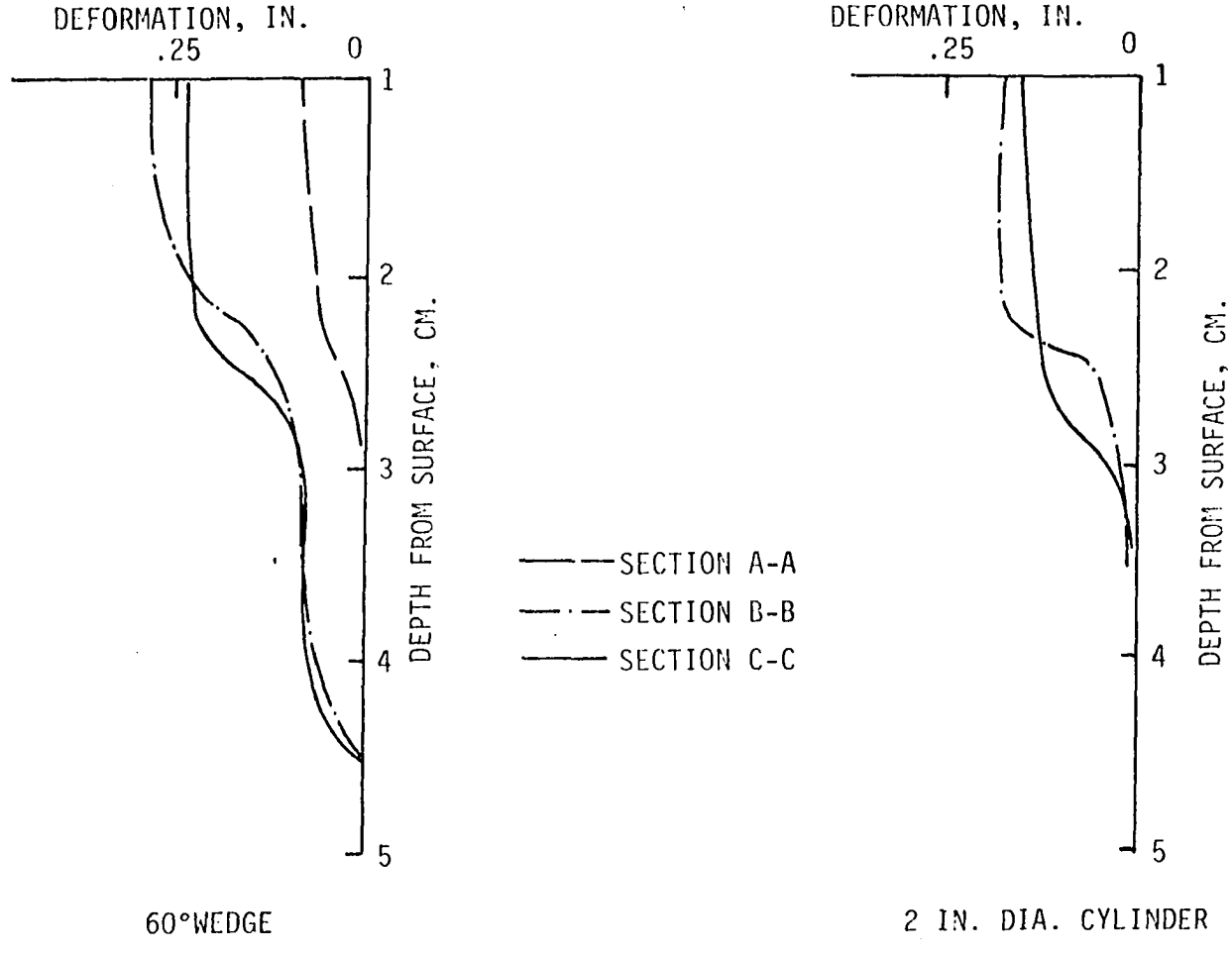

Figure 60. Soil movement along selected planes on Ottawa sand

between 1.2 - 1.6 in. for 60° wedge and .6 - .8 in. for 2" cylinder of the selected vertical planes, show rapid change on slope at the shear boundary. The 60° wedge also shows two zones of shearing movement.

Penetration on Silty Clay Loam

(Monona Soil)

The typical displacement pattern and corresponding vector field for Monona soil are shown on Figure 61. From a limited number of tests performed, the following experimental facts were observed:

1. Monona soil exhibits a relatively small compacted zone compared to Shelby soil.
2. A brittle type of failure occurred with a distinctively clear failure boundary.
3. Non-symmetrical failure occurred, tending to follow the weakest plane along a line of steel balls. The balls which served as grid points are pressed on the front of the sample and, sometimes create localized shearing of the surrounding material.

The force and penetration relationships for a 2 in. dia. cylinder and 60° wedge are shown on Figure 62. The theoretical curves were from modified equation (32) and equation 26, using soil parameters from the K-Test. A rapid drop in resisting force occurs when movement along failure plane starts; then after the soil particles rearrange to their new positions the resisting force is regained.

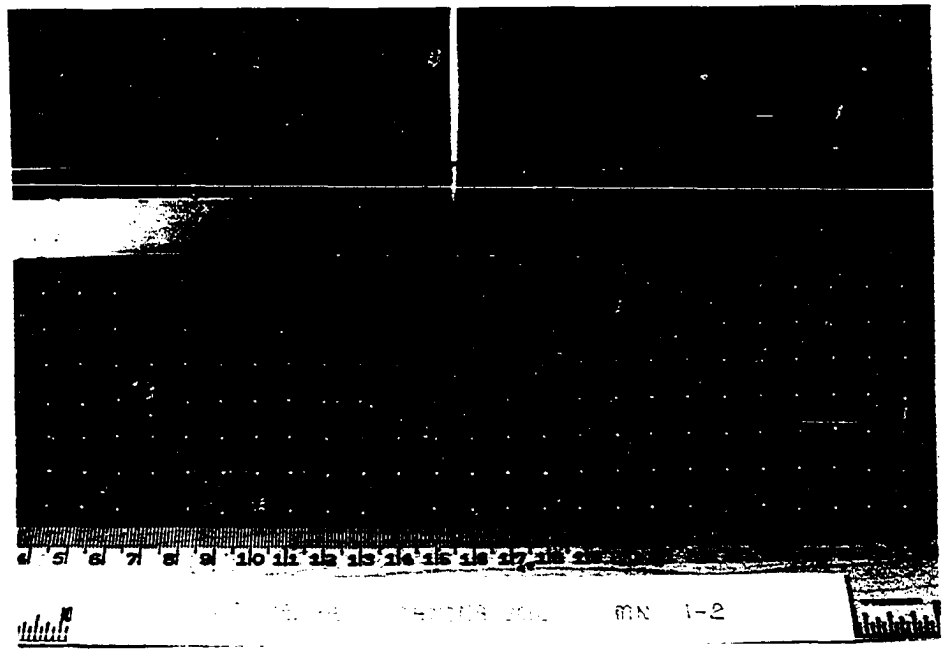

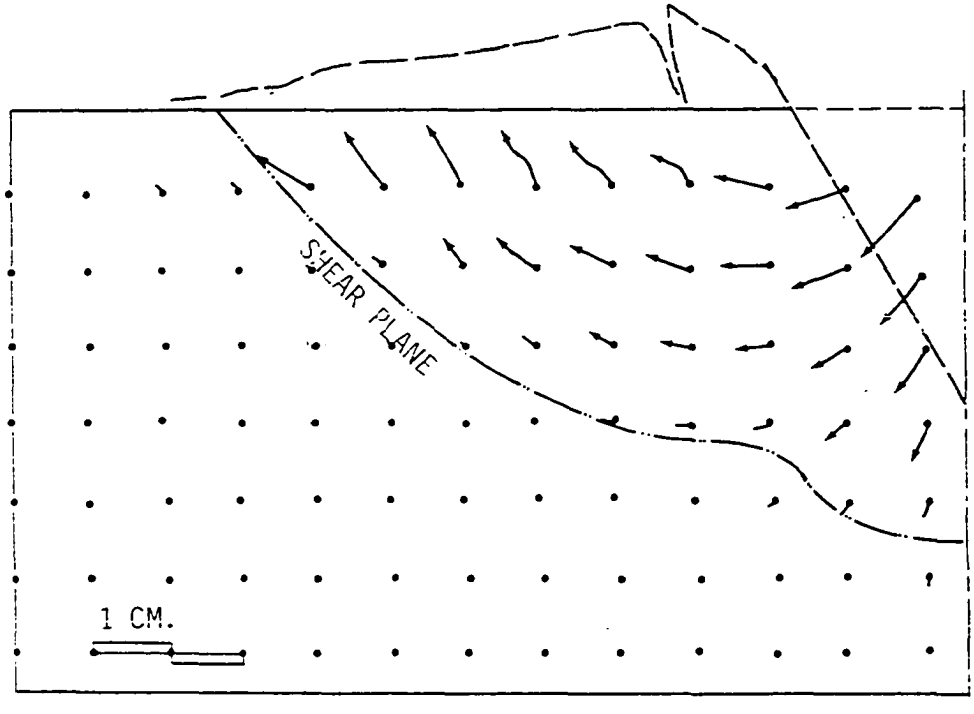

Figure 61. Soil deformation and vector field under 60° wedge penetration on Monona soil

Field Test

The primary objective of the field test was to examine the possibility that penetration tests could be used *in situ* to determine the basic soil parameters c and ϕ.

The field tests were performed on a silty sand and a clay loam. It should be pointed out that the correction of raw data is very important for the results to be of use for calculation of the soil strength parameters. Error normally comes from the initial seating of penetrometers and evenness of the ground surface. The corrections made were first to neglect the first two data points, second to fit the rest of the data by linear regression, and third to correct the intersect of the curve so that it starts from zero origin.

The corrected penetration curves from wedges and a sphere on silty sand are shown in Figure 63. The curves are straight lines with correlation coefficients of 0.9998, 0.9995 and 0.9993 for the 6" diameter sphere, 45° and 30° wedges, respectively. The slope of the penetration curves for 45° and 30° wedge are 2990 and 2022 lb. per in. which used to calculate the soil parameters c and ϕ. The penetration curves for 60° and 30° cones on Figure 64 show the same trends as were observed from modeling clay and Shelby soil. Corrections to the cone penetration data were made on transformed curves of square root resisting force, and the transformed penetration curves for the cones again show straight lines with 0.9996 coefficient of correlation

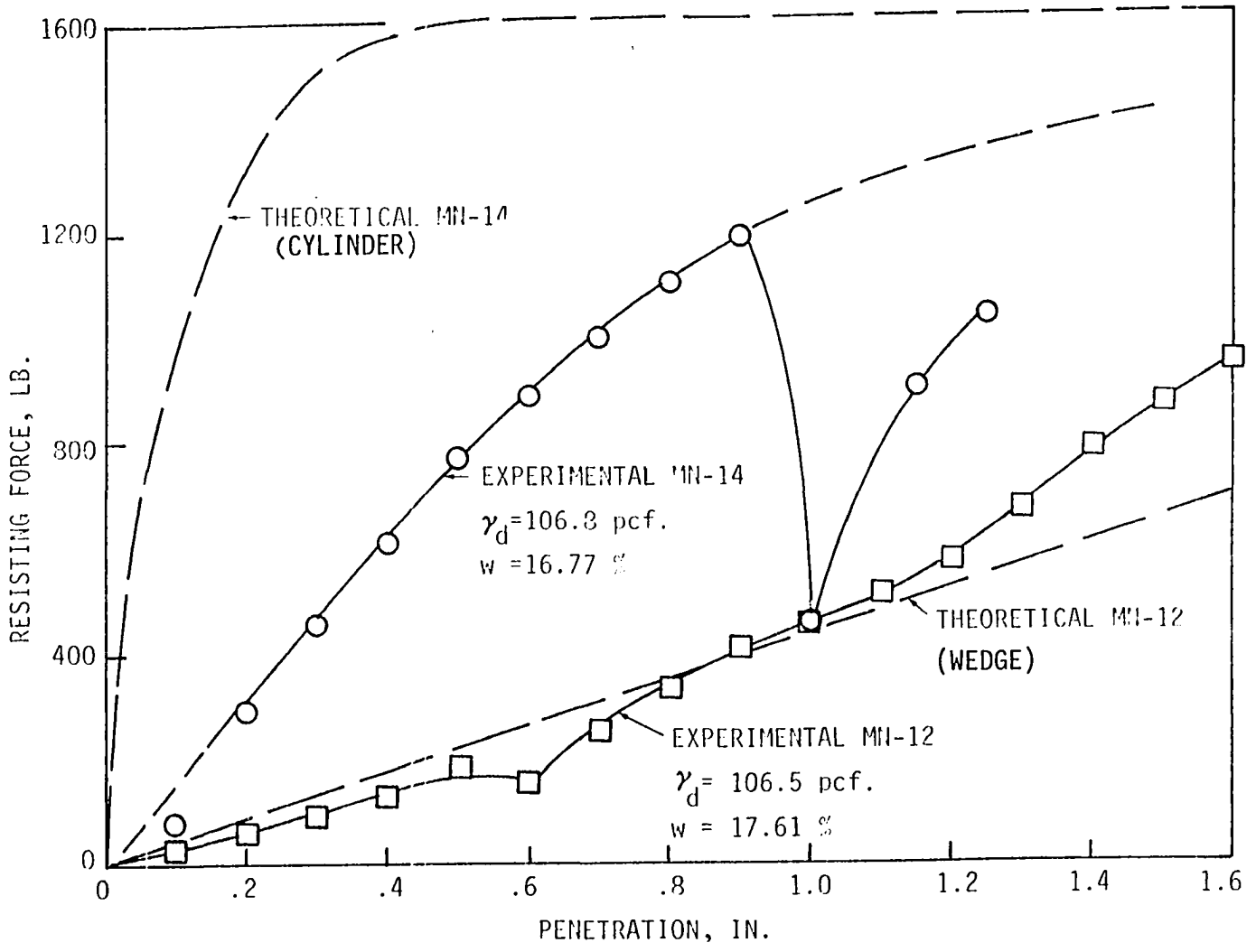

Figure 62. Penetration curves for wedge and cylinder on Monona soil

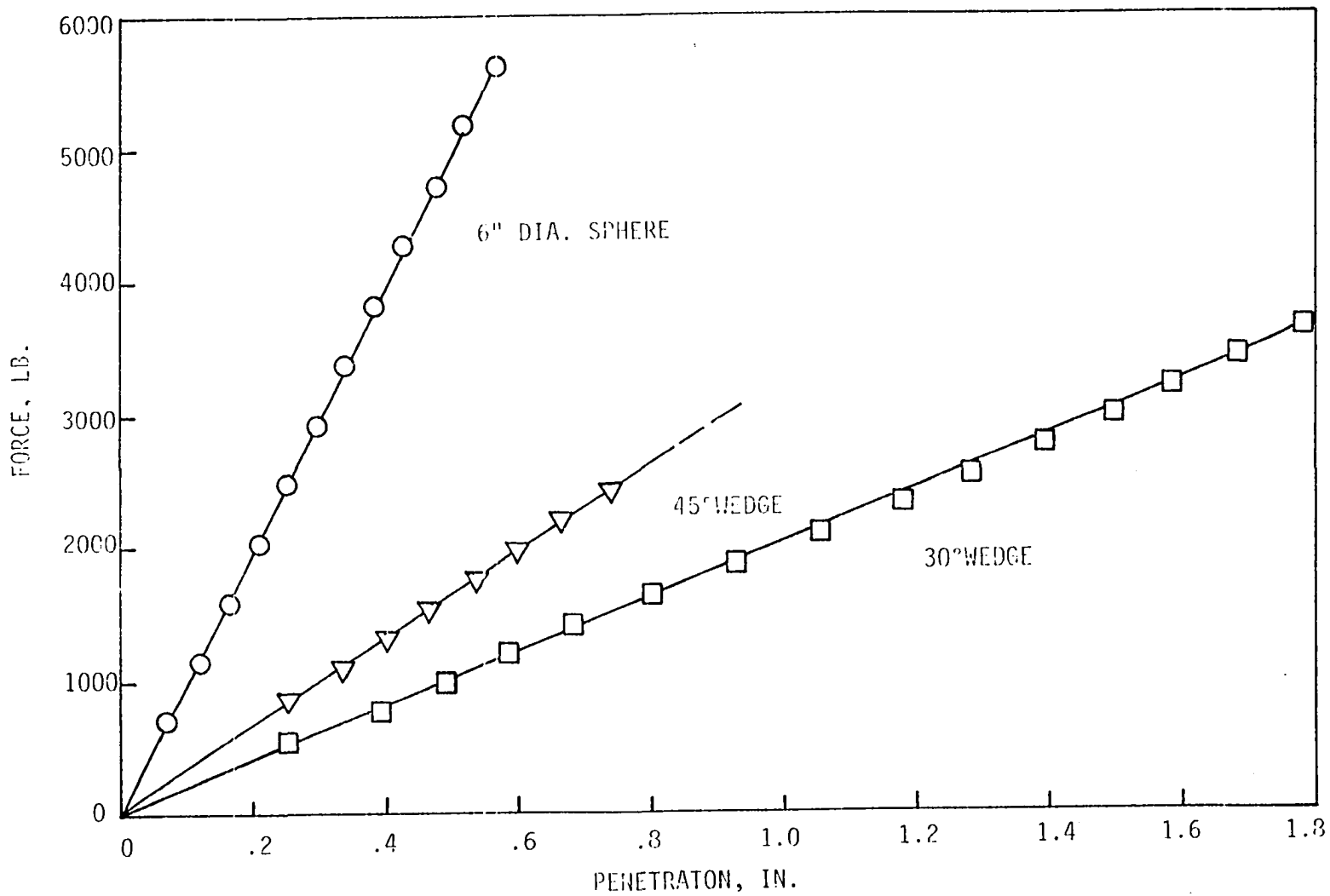

Figure 63. Field penetration curves for sphere and wedge on silty sand

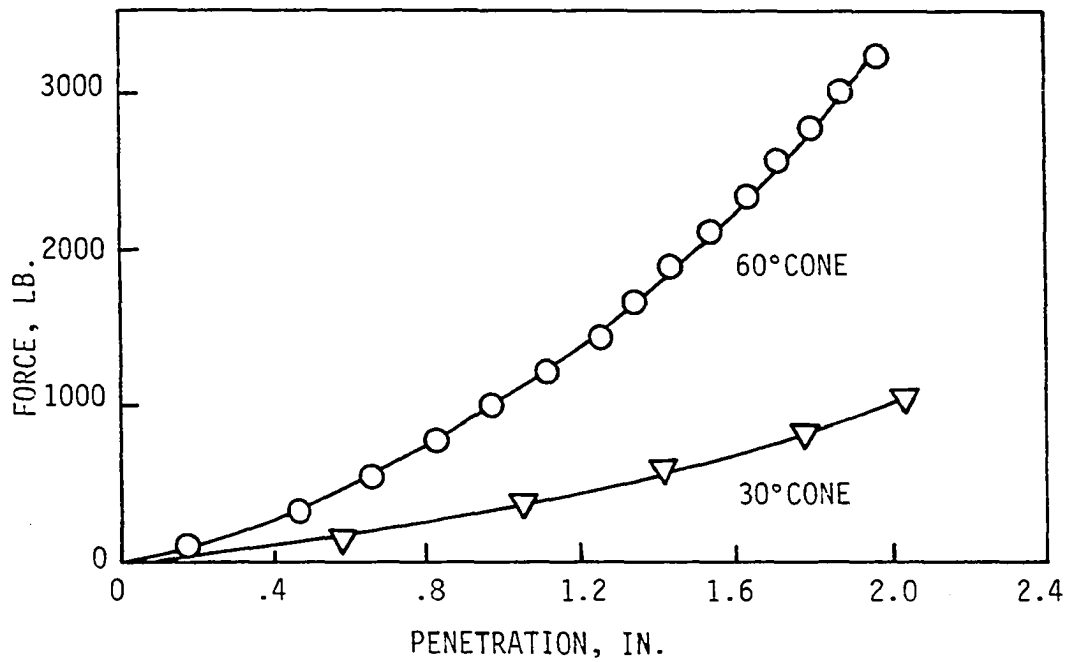

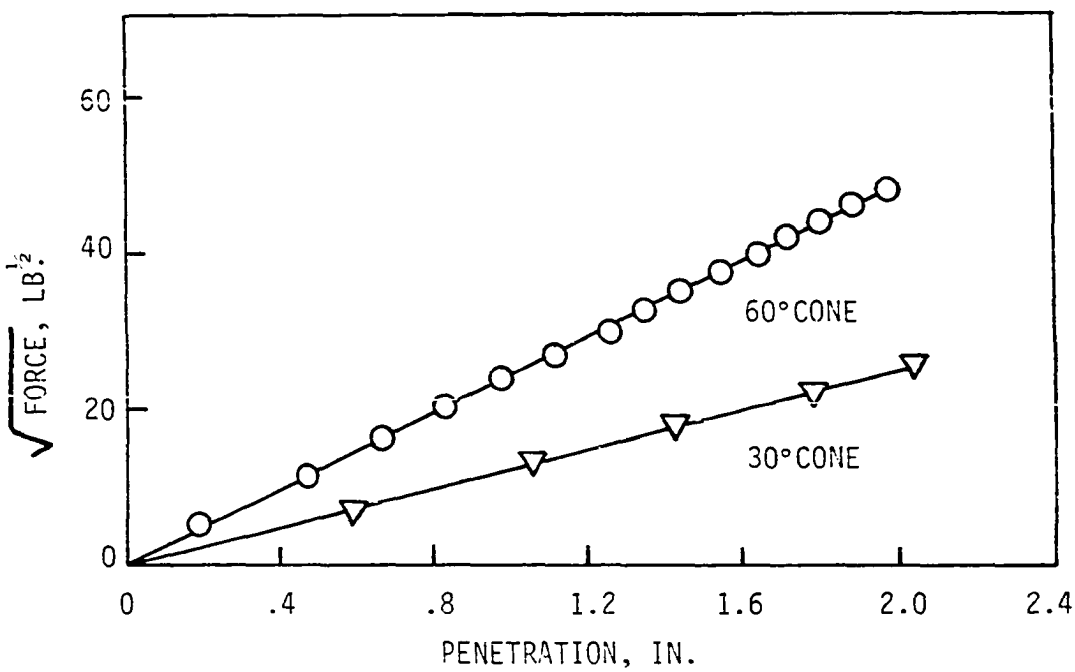

Figure 64. Field penetration curves for cones on silty sand

in both cases. However, the soil parameters could not be evaluated from cones because the data show a negative "λ" value.

Similar penetration curves for 45° and 30° wedges in the Clarion clay loam are shown in Figure 65. The sphere gave a linear curve up to 1.0 in. penetration, then started to flatten.

The soil parameters calculated from 30° and 45° wedges for both soils are presented in Figure 66. Since the values of soil-to-steel friction ϕ_s are unknown, the cohesion and ϕ were plotted against ϕ_s. Lutenegger (23) reported that the value of ϕ_s in relation to the ϕ angle is $\phi_s = 1.04\ \phi - 11.73$ for the Shelby soil and $\phi_s = 0.99\ \phi - 13.35$ for Monona soil. In both cases the linear relation can be simplified to $\phi_s = \phi - K$, where K is a constant. If we assume that silty sand and Clarion soil exhibit a similar relation, straight lines of $\phi_s = \phi$ can be drawn tangent to the curves on Figure 66. The tangential point should be ϕ_s for each soil, and then the soil parameters for the silty sand and the Clarion soil are estimated as follows:

Soil	Cohesion, c, psi	ϕ angle, degree
Clarion	4.5	42°
Silty sand	15.0	32

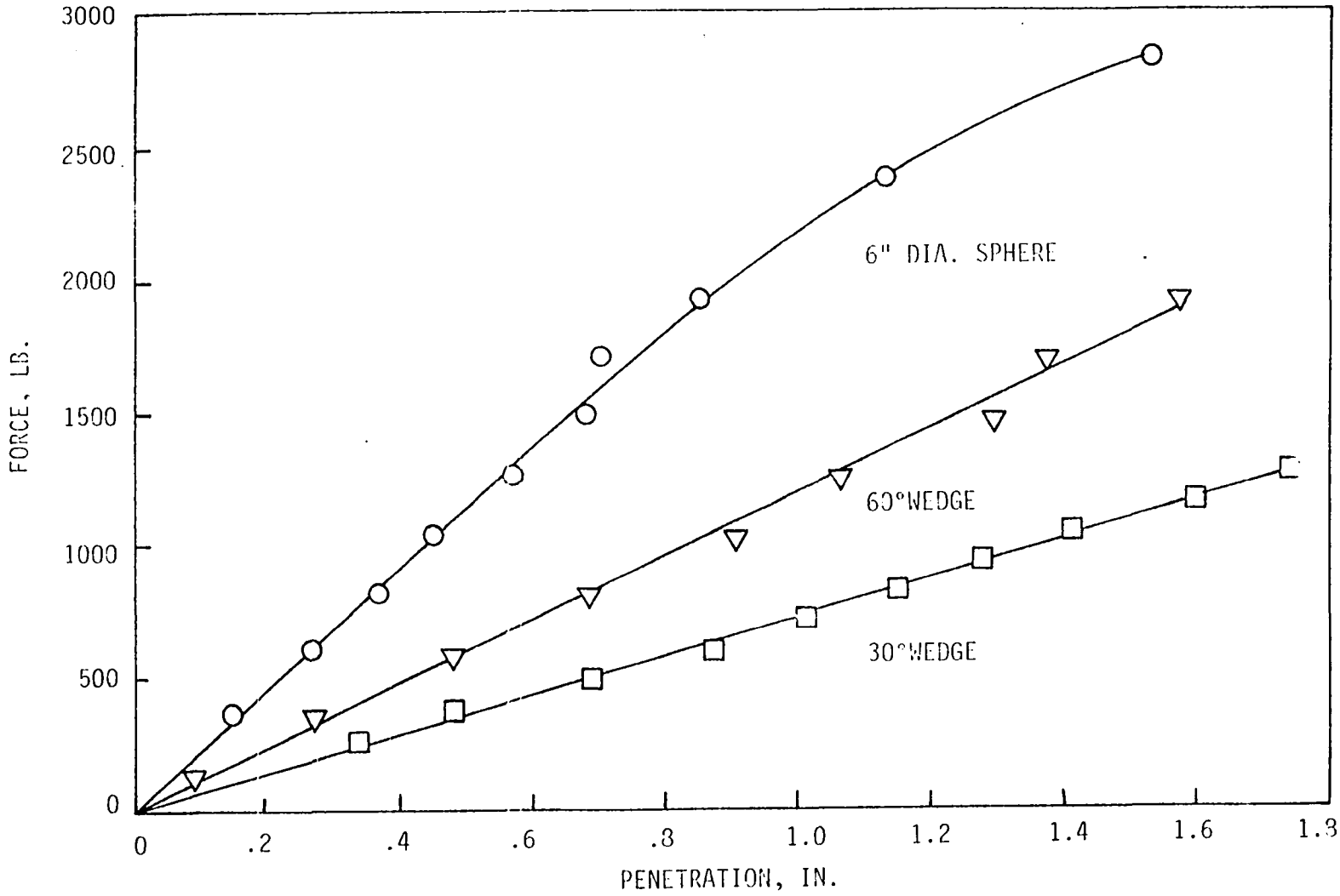

Figure 65. Field penetration curves for wedges and sphere on Clarion soil

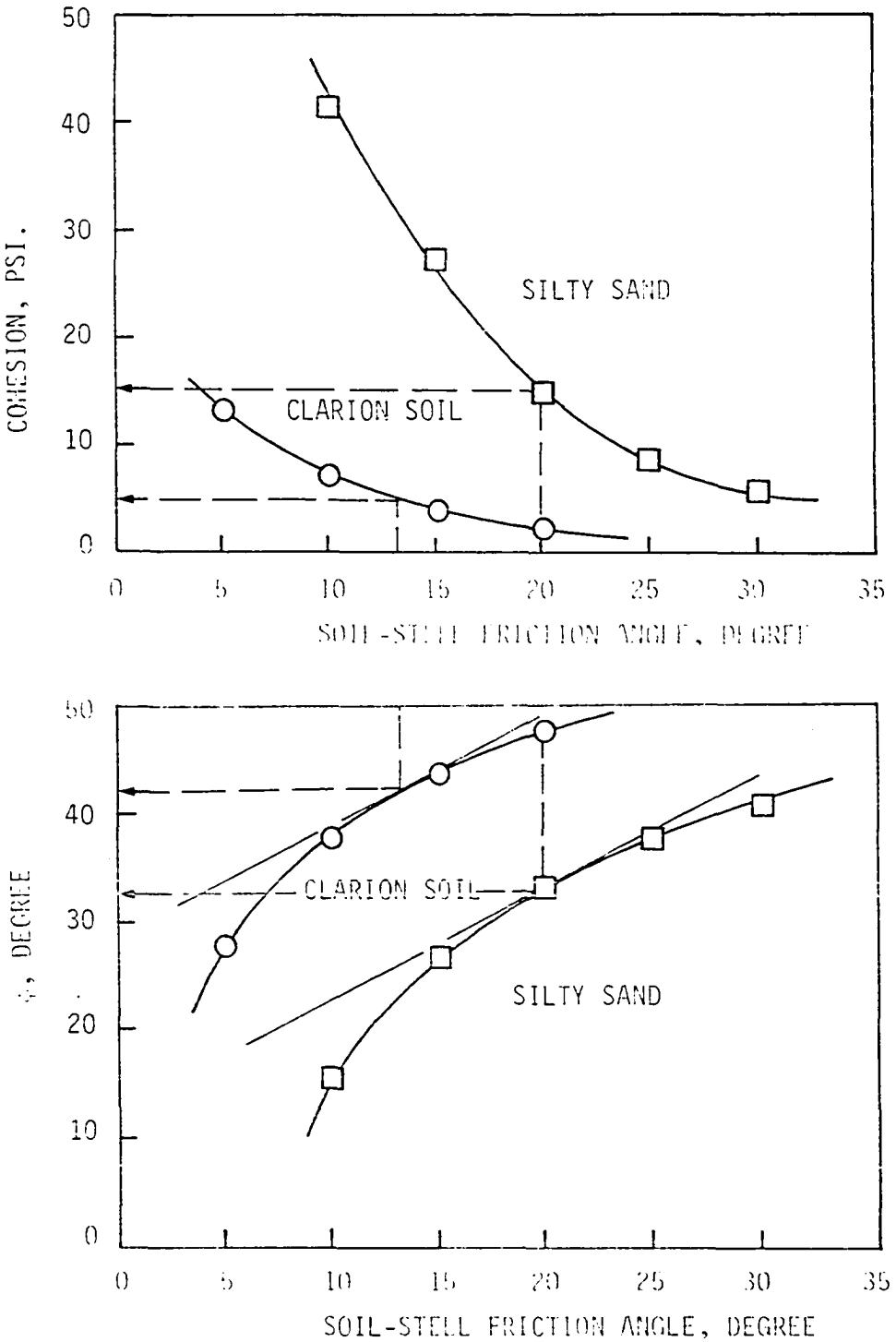

Figure 66. Strength parameters of silty sand and Clarion soil from field wedge penetrations

This procedure is a suggestion since, for a more precise evaluation the values of ϕ_s or the relation of ϕ_s to ϕ should be determined.

Application of Finite Element Method for Soil Penetration

The finite element method is a numerical procedure for solving differential equations of physics and engineering. A continuous quantity, such as temperature, pressure or displacement can be approximated by a discrete model composed of a set of piece-wise continuous functions defined over a finite number of elements. Segerlind (37) gave the general advantages of finite element method as:

1. The material properties in each element on the boundary do not have to be the same.
2. Irregularly shaped boundaries can be approximated easily.
3. The size of the elements can be varied according to the accuracy needed.
4. Discontinuous or mixed boundaries can be handled.

Even though this method was originated in aerospace and structural engineering, the application in rock and soil mechanics has increased in recent years. However, the nature of soils and rocks is more complex and requires different considerations from structural materials. The problems usually encountered in soil problems are non-linearity of stress-strain relation and the geometry due to large displacements, anisotropic properties of soil media, etc.

The finite element method had been used to solve penetration problems on saturated clay by Baligh and Scott (1) and on rock by Wang and Lehnhoff (41), but unsaturated soil that exhibits both compaction and shearing mechanism, is a unique problem. It is worthwhile to discuss the application of finite element for unsaturated soil in terms of advantages and disadvantages compared to conventional elastic and plastic theories.

The following problems are expected to be encountered in application of the finite element method to soil penetration:

1. Non-linear stress-strain relations.

Soil often exhibits non-linear stress-strain relations caused by a number of factors such as stress history and state of strain. Plastic theories usually neglect the elastic range and assume a rigid-plastic type curve with no appreciable amount of deformation occurring before the soil is failed. This assumption is valid in penetration problems dealing with brittle type soil such as Monona, when the geometry of penetrometers introduces shearing at low penetration. In soils such as modeling clay or Shelby soil, the stress-strain relationship shows non-linearity and considerable deformation must occur before the failure state is achieved. The finite element method can monitor the actual relationship by the techniques shown of Figure 67a, b, and c, and re-enter the stress-strain data according to the stage of deformation occurring in the soil. The stiffness matrix which is involved in the finite element formulation then would

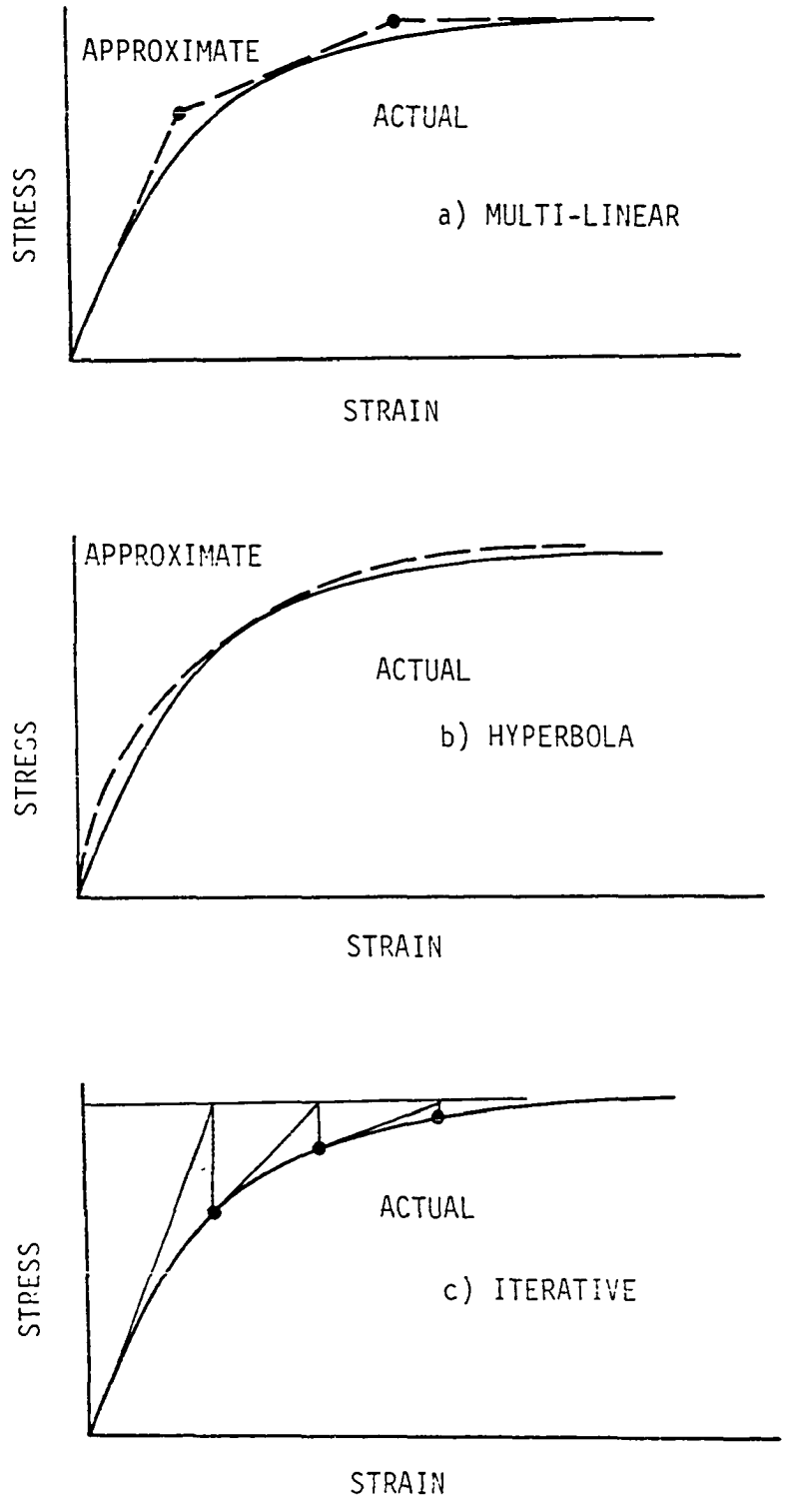

Figure 67. Techniques for approximating a stress-strain relation for soil in the finite element method

be the function of strain level, and an iterative procedure would be needed to model the changing stiffness matrix.

2. Non-linear geometry.

Large displacements usually occur in soil penetration, and the deformed geometry is different from the initial one, as shown on Figure 68. In the finite element method the new positions of model points or elements have to be reassigned according to their most recent positions. In turn the new stiffness matrix which also is the function of the element geometry has to be reformulated for every loading increment. Plastic theory takes into account the change in geometry by assuming a deformed geometry known as a slip-line field, such as Prandtl's slip-lines.

3. Anisotropic soil properties.

Anisotropy in soil may involve sedimentary layering or artificial compaction which causes preferential arrangement of soil particles in a certain direction. Then strength and compressibility may vary according to direction within the soil mass. Similar phenomena occur in fractured rock since in a direction normal to the fracture plane, the tensile strength is zero but the compressive strength still exists. The different soil properties for each principal direction have to be specified for finite element method. For plastic theory there is presently no known solution.

4. Change in strength and compressibility due to compaction.

As mentioned before, during penetration, both shearing and

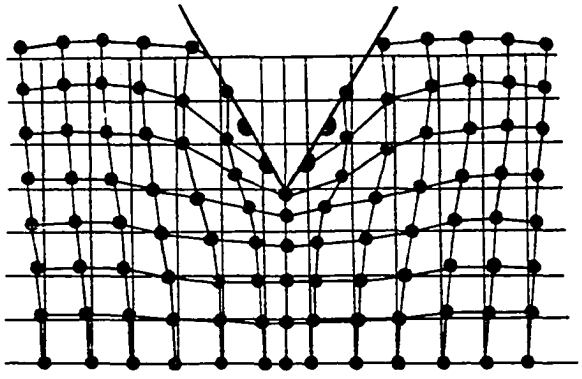

a) 60°WEDGE

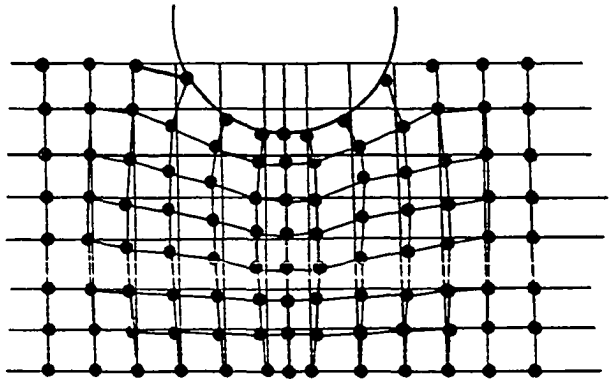

b) 2 IN.DIA. CYLINDER

Figure 68. Deformations of the grid elements on penetration test

compaction occurred. Compaction is expected to increase soil strength and decrease compressibility. The solution based on plastic theory did not directly consider the compaction effect, but the empirical modification can be done by establishing new strength parameters. The modified parameters can be used to calculate resisting force for the next penetration increment.

The finite element method seems to present a better way to simulate the compaction mechanism. The strength, stress-strain properties and volumetric compressibility of the soil at different densities can be evaluated by conventional triaxial or consolidation tests. The solution from finite elements considers stress-strain properties and will give the stresses and deformation of each element; then an extra step of modification of the dimension of each finite element for compressibility of the soil at the corresponding stage of stresses needs to be done. The new soil densities than can be calculated according to new volumes of each element. With the next loading increment the new set of strength, stress-strain properties and compressibility would have to be entered according to the existing density. This of course would be highly laborious and the solution would be case-specific. It therefore is doubtful whether the procedure could be made practicable for general reduction of penetration data, and it would be of primary value as a key to further understanding of the penetration mechanisms.

SUMMARY AND CONCLUSIONS

The following conclusions can be drawn based from the analyses and the experimental results:

1. The resisting force (penetration force) to a plane strain wedge-shaped penetrometer is derived as a function of soil basic strength parameters (c, ϕ and ϕ_s), the angle of the wedge, and depth of penetration on the basis of the following assumptions;

   a) The failure condition within the soil media is governed by the Mohr-Coulomb failure criteria.

   b) Soil is rigid-plastic material.

   c) The slip-line pattern of failure soil consists of a soil driving wedge, a log-spiral transition zone, and a soil passive wedge, as originally proposed by Prandtl.

   d) The size of the soil driving wedge is proportional to the ratio of ϕ_s over ϕ.

2. An iterative method is used to adjust the basic equation of wedge penetration so that the ratio of shearing stress over normal stress on the wedge surface is equal to the tangent of the corresponding ϕ_s.

3. The results obtained from the iterative method were then simplified to linear approximations such that derivations of theoretical resisting forces for other more complicated shapes became possible. Theoretical expressions for penetration resistance of long cylinders, rounded-tip wedges, blunt wedges, cones and spheres are presented.

4. A method for determining soil strength parameters c and ϕ from a set of wedge or cone penetrations is proposed if the friction between soil and steel is a known quantity. The experiments show c and ϕ of modeling clay from 30°-60°, 60°-90°, 30°-90° wedges and 30°-60° cone penetrations are consistent with triaxial data. But for Shelby soil, compaction introduced an additional undefined variable that made it difficult to obtain viable results. However, data from field tests of cones and wedges on silty sand and Clarion soil did give reasonable c and ϕ values.

5. The experimental deformation patterns on saturated cohesive soil (modeling clay) agree with Prandtl's slip-line field for wedge penetration. For a cylindrical shape, a pseudo-wedge of soil is formed and moves ahead in effect as part of the penetrometer. The theoretical expression was modified for a cylinder with a soil wedge and gave closer agreement with the experimental results.

6. Deformations of unsaturated cohesive soil (Shelby soil) indicate that in addition to shearing, compaction occurred. The size of the shearing and compaction zones depends on the shape and geometry of the penetrometer, saturation of soil media, and depth of penetration. The relative percentages of shearing and compacting mechanisms by area are plotted against geometry of penetrometer for different depth of penetration and percent of saturation for Shelby soil, Figure 69.

7. Compaction during penetration increased the soil density

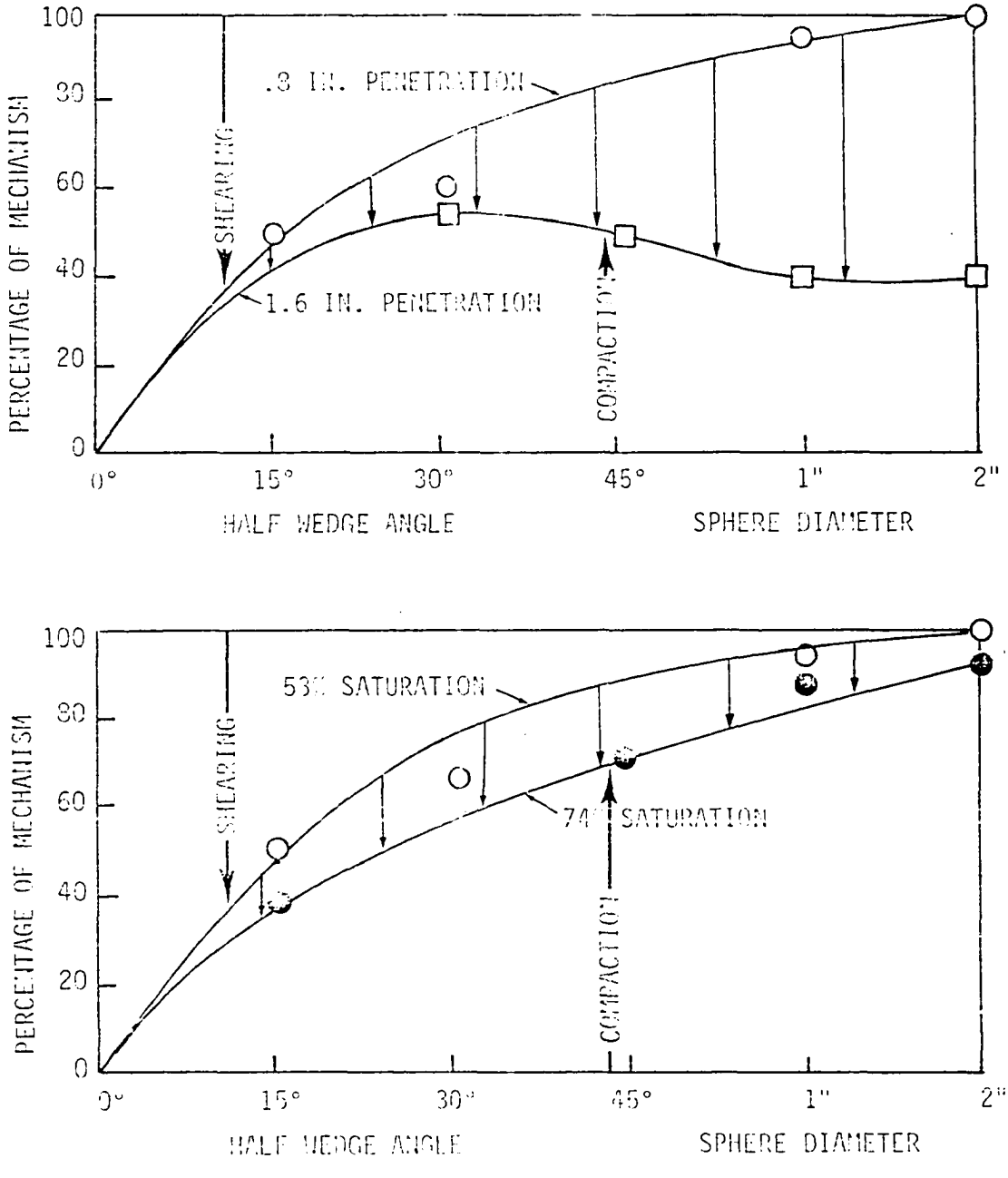

Figure 69. Relation of deformation mechanism and penetrometer shape, soil saturation, and degree of penetration

and in turn increased the soil strength. The elastic solution and stress path method can be used to check and estimate the changes in strength parameters.

8. The deformations observed for dense sand were purely shearing type with clearly distinct failure planes. The shearing is stick-slip type, as the movement of sand particles on the shear plane allowed the resisting force to go to zero, then regain as a deeper failure plane developed.

9. The silty clay loam (Monona Soil) shows a brittle type of failure similar to sand, and when the relative movement along the failure plane starts, the resisting force drops to a small amount and then regains as the particles rearrange to their new position. The failure creates separated pieces of soil rather than one shear plane.

10. The field tests for wedge, cone and sphere penetrations give the same shapes of force-penetration curves as predicted by the theory. The basic strength parameters evaluated from wedge penetrations are in the reasonable range.

SUGGESTION FOR FURTHER RESEARCH

1. Study the effect of soil-to-steel friction of the penetrometer surface on deformation patterns. The displacement model tests for perfectly rough, smooth and semi-rough surfaces can be done to verify the available theoretical expressions. A saturated soil such as modelling clay is suggested for shearing in lieu of compaction.

2. Use finite element method as the tool to study the combined compaction and shearing mechanisms in unsaturated soil.

3. Study field uses of cone and wedge penetrations on fully controlled sites of known soil parameters.

4. Study the penetration on layered soil in a displacement model test. The theoretical expressions can be modified according to the experimental results.

BIBLIOGRAPHY

1. Baligh, M. M. and R. F. Scott. "Analysis of Wedge Penetration in Clay." Geotechnique 26, No. 1, (1976), 185-208.

2. Baligh, M. M. and R. F. Scott. "Quasi-Static Deep Penetration in Clays." J. Geo. Eng. Div. Proc. ASCE 101, No. GT11, (Nov. 1975), 1119-1133.

3. Bathe, K. J., E. L. Wilson and R. H. Iding. "NONSAP - A Structural Analysis Program for Static and Dynamic Response of Nonlinear Systems." SESM Report 74-3, Department of Civil Engineering, University of California, Berkeley, 1974.

4. Begemann, H. K. S. "Improved Method of Determining Resistance to Adhesion by Sounding Through a Loose Sleeve." Proc. 3rd Inter. Conf. Soil Mech. Found. Eng., Zurich, 1953, Vol. I.

5. Boyd, K. "An Analysis of Wheel Load Limits as Related to Design." Highway Research Board Proceedings 22, (1942), 185-198.

6. Butt, G. S. "Soil Bearing Tests Using a Spherical Penetration Device." Unpublished Ph.D. Thesis, Iowa State University, Ames, Iowa, 1967.

7. Butterfield, R. and K. Z. Andrawes. "An Investigation of a Plane Strain Continuous Penetration Problem." Geotechnique 22, No. 4, (1972), 595-617.

8. Butterfield, R., R. M. Harkness and K. Z. Andrawes. "A Stereo Protogrammetric Method for Measuring Displacement Fields." Geotechnique 20, No. 3, (1970), 308-314.

9. Cheatham, J. B., Jr. "An Analytical Study of Rock Penetration by a Single Bit Tooth." Proc. Eighth Annual Drill and Blast Symp., University of Minnesota, No. 2, (1958), A1-A22.

10. Cheatham, J. B., Jr. "Rock-Bit Tooth Friction Analysis." Society of Petroleum Engineers Journal, 3, No. 4, (Dec. 1963), 327-332.

11. Chen, W. F. Limit Analysis and Soil Plasticity. Amsterdam: Elsevier Scientific Publishing Company, 1975.

12. Desai, C. S. and Abel, J. F., Introduction to the Finite Element Method. New York: Van Nostrand Reinhold, 1972.

13. Dexter, A. R. and D. W. Tanner. "The Force on Spheres Penetrating Soil." Journal of Terramechanics, 9, No. 4, (1972), 31-39.

14. Fox, N. S., R. D. Barkdale, R. L. Handy and G. D. Trott. "Measuring and Testing Techniques for Determination of the In-situ States of Stress in Soils." Interim Report No. DOT-FH-11-9172 for U.S. Dept. of Trans., Federal Highway Administration, Washington, D.C., July 1977.

15. Garber, M. and R. Baker. "Bearing Capacity by Variational Method." J. Geo. Eng. Div. Proc. ASCE 103, No. GT11, (Nov. 1977), 1209-1225.

16. Gnirk, P. F. and J. B. Cheatham Jr. "Indentation Experiments on Dry Rocks Under Pressure." Journal of Petroleum Technology, 15, (Sept. 1963), 1031-1039.

17. Godskenson, O. "The Spring Scale Cone: A Pocket Apparatus for Determining the Firmness of Clay." Proc. Inter. Conf. Soil Mech., Harvard, 2, 1936, 38-40.

18. Handy, R. L., J. M. Pitt, L. E. Engle and D. E. Klockow. "Rock Borehole Shear Test." Preprint for 17th Symp. on Rock Mechanics, E.R.I., Iowa State University, Ames, Iowa, Aug. 1976.

19. Higdon, A., E. H. Ohlsen, W. B. Stiles, J. A. Weese and W. F. Riley. Mechanics of Materials. 3rd Edition, New York: John Wiley and Sons, Inc., 1976.

20. Hill, R. The Mathematical Theory of Plasticity. Oxford: Clarendon Press, 1950.

21. Lambe, T. W. "The Engineering Behavior of Compacted Clay." J. Soil Mech. and Found. Div. ASCE 84, No. SM2, May 1958.

22. Lambe, T. W. and R. V. Whitman. Soil Mechanics. New York: John Wiley and Sons, Inc., 1969.

23. Lutenegger, A. J. "The Iowa Continuous K-Test: A laboratory test for measuring lateral stresses in soils induced by vertical applied loads." Unpublished M.S. Thesis, Iowa State University, Ames, Iowa, 1975.

24. Meyerhof, G. G. "Influence of Roughness of Base and Ground-water Conditions on the Ultimate Bearing Capacity of Foundation." Geotechnique 5, No. 3, (1955), 227-242.

25. Meyerhof, G. G. "Shallow Foundations." J. Soil Mech. and Found. Div. ASCE 91, No. SM2 (March, 1965), 21-31.

26. Meyerhof, G. G. "The Ultimate Bearing Capacity of Foundation." Geotechnique 2, (1950-1951), 301-332.

27. Meyerhof, G. G. "The Ultimate Bearing Capacity of Wedge-Shaped Foundations." Proc. 5th International Conf. on Soil Mechanics and Foundation Eng., Paris, II, (1961), 105-110.

28. Miller, T. W. and J. B. Cheatham Jr. "Analysis of the Indentation of a Compacting Material by a Perfectly Rough Wedge." Int. J. Rock Mech. Min. Sci. 9, 1972, 475-492.

29. Mohr, H. A. "Exploration of Soil Conditions and Sampling Operations." Soil Mechanics Series No. 21, Graduate School of Engineering, Harvard University, Cambridge, Mass., 1943.

30. Porter, O. J. "The Preparation of Subgrades." Highway Research Board Proceedings 18, 2, (1938), 324-331.

31. Prandtl, L. "Uber die Eindringungsfestigkeit (Harte) plastischer Baustoffe und die Festigkeit von Schneider." Eindringungsfestigkeit und Festigkeit von Schneider, I, (1921), 15-21.

32. Proctor, R. R. "Discription of Field and Laboratory Methods." Engineering News-Record, 111, No. 10, (Sept. 1933), 286-289.

33. Proctor, R. R. "Fundamental Principles of Soil Compaction." Engineering News Record, 111, No. 9, (Aug. 1933), 245-248.

34. Richardson, R. C. D., "The Wear of Metallic Materials by Soil-Practical Phenomena." J. Agric. Eng. Res. 12 (1), (1967), 22-39.

35. Sanglerat, G. The Penetrometer and Soil Exploration. Amsterdam: Elsevier Publishing Company, 1972.

36. Seed, H. B. and Chen, C. K. "Structure and Strength Characteristics of Compacted Clays." J. Soil Mech. and Found. Div. ASCE 85, No. SM5, (Oct. 1959), 87-128.

37. Segerlind, L. J. Applied Finite Element Analysis. New York: John Wiley and Sons, Inc., 1976.

38. Spangler, M. G. and R. L. Handy. Soil Engineering. 3rd Edition, New York: Intext Educational Publishers, 1973.

39. Terzaghi, K. Theoretical Soil Mechanics. New York: John Wiley and Sons, Inc., 1943.

40. Tuma, J. J. Engineering Mathematics Handbook. New York: McGraw-Hill Book Company, 1970.

41. Wang, J. K., T. F. Lehnhoff. "Bit Penetration into Rock - A Finite Element Study." Int. J. Rock Mech. Min. Sci. and Geomech. Abstr., 13, (1976), 11-16.

42. Winterkorn, H. F. and H. Y. Fang. Foundation Engineering Handbook, New York: Van Nostrand Reinhold, 1975.

43. Withiam, J. L. and F. H. Kulhawy. "Undrained Volume Changes in Compacted Cohesive Soil." J. Geo. Eng. Div. Proc. ASCE 102, No. GT10, (Oct. 1976), 1029-1039.

44. Yong, R. N. and C. K. Chen. "Cone Penetration of Granular and Cohesive Soils." J. Eng. Mech. Div. Proc. ASCE 102, No. EM2 (1976), 345-363.

45. Yong, R. N., C. K. Chen and R. Sylvester-Williams. "A Study of the Mechanics of Cone Indentation and its Relation to Soil-Wheel Interaction." Journal of Terramechanics, 9, No. 1 (1972), 19-36.

ACKNOWLEDGMENTS

The author gratefully acknowledges the support given by the Thai government and the Engineering Research Institute, Iowa State University, during the study and research.

A sincere thanks is given to Dr. R. L. Handy for his endless support, encouragement and guidance, not only during the research, but throughout the period that the author studied in the United States.

Thanks are also extended to Professor J. M. Hoover, Dr. W. H. Scholtes, Dr. W. W. Sanders and Dr. T. Demirel, the author's graduate committee, for their guidance.

The author wishes to express his appreciation for the patience and encouragement of his parents, Mr. Viehian and Mrs. Aree Mairaing, his wife, Sompit, which made the completion of this study possible.

Special thanks go to Kathy Crouch for her fine work in typing this thesis.

APPENDIX A: RESISTING FORCE ON LONG CYLINDER

The equation (31) leads to

$$F = 2c\ R.\sigma_{\omega o}\left[\int_{\beta}^{\frac{\pi}{2}} e^{\frac{2.3\theta}{\lambda}}.\sin\theta\ d\theta + \tan\phi_s\int_{\beta}^{\frac{\pi}{2}} e^{\frac{2.3}{\lambda}}.\cos\theta\ d\theta\right] \tag{A1}$$

and separately the integrations are

$$\int_{\beta}^{\frac{\pi}{2}} e^{\frac{2.3\theta}{\lambda}}.\sin\theta\ d\theta = \left[\frac{e^{\frac{2.3\theta}{\lambda}}.(\frac{2.3}{\lambda}\sin\theta - \cos\theta)}{(\frac{2.3}{\lambda})^2 + 1}\right]_{\beta}^{\frac{\pi}{2}}$$

$$= \frac{\left[e^{\frac{2.3\pi}{2\lambda}}.(\frac{2.3}{\lambda}) - e^{\frac{2.3\beta}{\lambda}}.(\frac{2.3}{\lambda}\sin\beta - \cos\beta)\right]}{(\frac{2.3}{\lambda})^2 + 1} \tag{A2}$$

$$\int_{\beta}^{\frac{\pi}{2}} e^{\frac{2.3\theta}{\lambda}}\cos\theta\ d\theta = \left[\frac{e^{\frac{2.3\theta}{\lambda}}.(\frac{2.3}{\lambda}\cos\theta + \sin\theta)}{(\frac{2.3}{\lambda})^2 + 1}\right]_{\beta}^{\frac{\pi}{2}}$$

$$= \frac{\left[e^{\frac{2.3\pi}{2\lambda}} - e^{\frac{2.3\beta}{\lambda}}.(\frac{2.3}{\lambda}\cos\beta + \sin\beta)\right]}{(\frac{2.3}{\lambda})^2 + 1} \tag{A3}$$

Substituting equation (A2) and (A3) into (A1) gives

$$F = 2cR\sigma_{\omega o}\left[\frac{(\frac{2.3}{\lambda} + \tan\phi_s)(e^{\frac{2.3\pi}{2\lambda}} - \sin\beta . e^{\frac{2.3\beta}{\lambda}})}{(\frac{2.3}{\lambda})^2 + 1} + \frac{\cos\beta . (1 - \frac{2.3}{\lambda}\tan\phi_s) . e^{\frac{2.3\beta}{\lambda}}}{}\right]$$

$$= 2cRe^{K1}\left[\frac{1}{K3^2 + 1}\right]\left[(K3 + \tan\phi_s).(e^{K2} - \sin\beta) + \cos\beta\ (1 - K3\tan\phi_s)\right] \qquad (A4)$$

where

$$K1 = 2.3\ (\frac{\beta}{\lambda} + \log\sigma_{\omega o})$$

$$K2 = \frac{2.3}{\lambda}\ (\frac{\pi}{2} - \beta)$$

$$K3 = \frac{2.3}{\lambda}$$

APPENDIX B: RESISTING FORCE ON ROUNDED TIP WEDGE

The total resisting force on a rounded tip wedge from equation (36) is

$$F_T = F_R + F_W \tag{B1}$$

where

$$F_R = \frac{2c.R.e^{K1}}{(K3^2 + 1)} \left[(K3 + \tan\phi_s)(e^{K2} - \sin\beta) + \cos\beta\ (1 - K3.\tan\phi_s) \right] \tag{B2}$$

when

$$K1 = 2.3\ (\beta/\lambda + \log \sigma_{\omega O})$$

$$K3 = \frac{2.3}{\lambda}\ (\frac{\pi}{2} - \beta)$$

$$K3 = \frac{2.3}{\lambda}$$

and

$$F_W = 2c.H_W\ (\tan\beta + \tan\phi_s)\ e^{2.3(\beta/\lambda + \log \sigma_{\omega O})} \tag{B3}$$

APPENDIX C: RESISTING FORCE ON BLUNT WEDGE

The total resisting force on a blunt from equation (38) is

$$F_T = F_B + F_W \tag{C1}$$

where

$$F_B = 2c.H_o \sin \beta.e^{2.3(90/\lambda + \log \sigma_{\omega o})} \tag{C2}$$

$$F_W = 2c.H \ (\tan\beta + \tan \phi_s).e^{2.3(\beta/\lambda + \log \sigma_{\omega o})} \tag{C3}$$

APPENDIX D: RESISTING FORCE ON SPHERE

The equation (43) can be written as

$$F = 2cR^2 e^{K1} \int_0^{2\pi} \left[\int_\beta^{\frac{\pi}{2}} e^{\frac{2.3\theta}{\lambda}} .\sin\theta.\cos\theta.d\theta + \tan\phi_s \int_\beta^{\frac{\pi}{2}} e^{\frac{2.3\theta}{\lambda}} \cos^2\theta \, d\theta \right] d\rho \qquad (D1)$$

The integration of the terms in the parentheses gives

$$\int_\beta^{\frac{\pi}{2}} e^{\frac{2.3}{\lambda}} .\sin\theta.\cos\theta \, d\theta = \left[\frac{e^{\frac{2.3}{\lambda}} \left(\frac{2.3}{\lambda} \sin 2\theta - 2 \cos 2\theta\right)}{2\left[\left(\frac{2.3}{\lambda}\right)^2 + 4\right]} \right]_\beta^{\frac{\pi}{2}}$$

$$= \frac{e^{\frac{2.3\pi}{2\lambda}} - e^{\frac{2.3\beta}{\lambda}} \left(\frac{2.3}{2\lambda} \sin 2\beta - \cos 2\beta\right)}{\left[\left(\frac{2.3}{\lambda}\right)^2 + 4\right]} \qquad (D2)$$

$$\int_\beta^{\frac{\pi}{2}} e^{\frac{2.3\theta}{\lambda}} \cos^2\theta.d\theta = \left[\frac{e^{\frac{2.3}{\lambda}} \left(\frac{2.3}{\lambda} \cos\theta + 2 \sin\theta\right).\cos\theta}{\left[\left(\frac{2.3}{\lambda}\right)^2 + 4\right]} + \frac{2\lambda}{2.3} .e^{\frac{2.3\theta}{\lambda}} \right]_\beta^{\frac{\pi}{2}}$$

$$= \frac{(\frac{2\lambda}{2.3})e^{\frac{2.3\pi}{2\lambda}} - e^{\frac{2.3\beta}{\lambda}}\left(\frac{2.3}{\lambda}\cos^2\beta + 2\cos\beta\sin\beta + \frac{2\lambda}{2.3}\right)}{\left[\left(\frac{2.3}{\lambda}\right)^2 + 4\right]} \qquad \text{(D3)}$$

Substitute equation (B2) and (B3) in (B1) and rearrange the terms to yield the following equation.

$$F = \frac{2cR^2.e^{K4}}{(K3^2 + 4)}\left[(1 + \frac{2}{K3}\tan\phi_s)\, e^{\frac{\pi}{2}} - \left\{\sin 2\beta\,(\frac{K3}{2} + \tan\phi_s)\right.\right.$$

$$\left.\left. - \cos 2\beta\,(1 - \frac{K3}{2}\tan\phi_s) + (\frac{K3}{2} + \frac{2}{K3})\tan\phi_s\right\} e^{\beta}\right]\int_0^{2\pi} d\rho \qquad \text{(D4)}$$

The term $\int_0^{2\pi} d\rho = 2\pi$

$$K3 = \frac{2.3}{\lambda}$$

$$K4 = 2.3\,(\frac{1+\beta}{\lambda} + \log\sigma_{\omega o})$$

APPENDIX E: RESISTING FORCE ON MODIFIED LONG CYLINDER

Included in this appendix is the derivation of resisting force on a cylinder based on the following assumptions.

1. A soil wedge of $\frac{\pi}{2} - \phi$ apical angle moves along with the cylinder during penetration as shown on Figure 70a. The soil wedge acts as a perfectly rough wedge, since the contact surfaces of the wedge are soil-to-soil interfaces.

2. At a certain depth of penetration when the soil wedge tangent to the curvature of the cylinder is at the ground level, the soil wedge is fully developed as in Figure 70b.

3. For deeper penetration, the combined action of the full wedge and part of cylinder occurs as on Figure 70c.

a) Wedge action ($H_a < H_{ac}$)

H = actual penetration of cylinder

a = half angle of soil pseudo-wedge = $\frac{\pi}{4} - \frac{\phi}{2}$

R = radius of cylinder

H_a = apparent penetration of pseudo-wedge

then

$$\eta = \cos^{-1}\left(\frac{R-H}{R}\right) \tag{E1}$$

$$H_a = \frac{R \sin \eta}{\tan \beta_a} \tag{E2}$$

The resisting force is equal to equation (26) when $H = H_a$, $\beta = \beta_a$, $\phi_s = \phi$ and the values λ and $\sigma_{\omega o}$ are the values for perfectly rough surface ($\phi_s = \phi$):

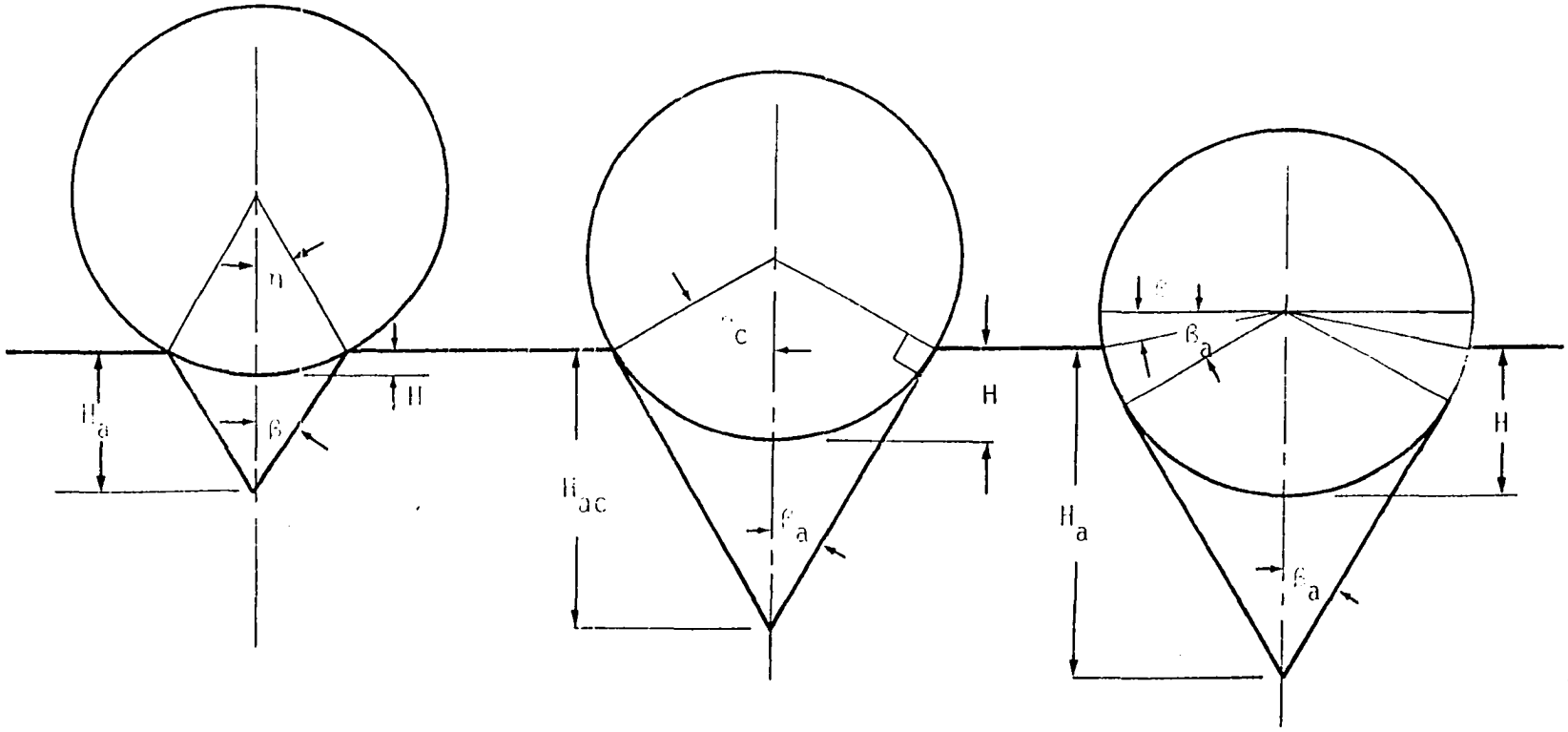

a) WEDGE ACTION ($H_a < H_{ac}$)

b) FULLY WEDGE ACTION ($H_a = H_{ac}$)

c) COMBINED WEDGE-CYLINDER ACTION ($H_a > H_{ac}$)

Figure 70. Calculation of modified cylinder penetration

$$F = 2c\,\sigma_{\omega o}.H_a\,(\tan\beta_a + \tan\phi).e^{2.3\,\frac{\beta_a}{\lambda}} \qquad \text{(E3)}$$

b) Full wedge action ($H_a = H_{ac}$)

$$\zeta = \frac{\pi}{4} + \frac{\phi}{2}$$

$$H_a = H_{ac} = R\,\frac{\sin\left(\frac{\pi}{4} + \frac{\phi}{2}\right)}{\tan\beta_a} \qquad \text{(E4)}$$

The resisting force is similar to equation (E3), except

$$H_a = H_{ac}.$$

e) Combined wedge and cylinder action ($H_a < H_{ac}$)

The total resisting force is the sum of resisting force on the full wedge and part of cylinder surface from A to B, which is

$$F = F_w + F_c \qquad \text{(E5)}$$

when

$$F_w = 2c\sigma_{\omega o}.\,H_{ac}\,(\tan\beta_a + \tan\phi)\,.e^{2.3\,\frac{\beta_a}{\lambda}} \qquad \text{(E6)}$$

and F_c can be derived from equation (31) as

$$F_c = 2c\sigma_{\omega o} \cdot R \qquad e^{2.3\frac{\theta}{\lambda}} (\sin\theta + \cos\theta.\tan\phi_s) \cdot d\theta \qquad \text{(E7)}$$

The separation of the integral terms is

$$\int_{\beta}^{\beta_a} e.^{\frac{2.3\theta}{\lambda}} \sin\theta.d\theta = \left[\frac{1}{(\frac{2.3}{\lambda})^2 + 1}\right]\left[e^{\frac{2.3\beta_a}{\lambda}} (\frac{2.3}{\lambda}\sin\beta_a - \cos\beta_a)\right.$$

$$\left. - e^{\frac{2.3\beta}{\lambda}} (\frac{2.3}{\lambda}\sin\beta - \cos\beta)\right] \qquad \text{(E8)}$$

$$\int_{\beta}^{\beta_a} e.^{\frac{2.3\theta}{\lambda}} \cos\theta d\theta = \left[\frac{1}{(\frac{2.3}{\lambda})^2 + 1}\right]\left[e^{\frac{2.3\beta_a}{\lambda}} (\frac{2.3}{\lambda}\cos\beta_a + \sin\beta_a)\right.$$

$$\left. - e^{\frac{2.3\beta}{\lambda}} (\frac{2.3}{\lambda}\cos\beta + \sin\beta)\right] \qquad \text{(E9)}$$

Substitution of equations (E8) and (E9) into (E7), gives

$$F_c = \frac{2c.R.\sigma_{\omega o}}{\left(\frac{2.3}{\lambda}\right)^2 + 1}\left[e^{\frac{2.3\beta_a}{\lambda}}\left[\sin\beta_a\left(\frac{2.3}{\lambda} + \tan\phi_s\right) + \cos\beta_a\left(\frac{2.3}{\lambda}\tan\phi_s - 1\right)\right] - e^{\frac{2.3\beta}{\lambda}}\left[\sin\beta\left(\frac{2.3}{\lambda} + \tan\phi_s\right) + \cos\beta\left(\frac{2.3}{\lambda}\tan\phi_s - 1\right)\right]\right] \qquad \text{(E10)}$$

APPENDIX F: RESISTING FORCE ON MODIFIED SPHERE

The resisting force on modified sphere is derived from the same geometrical assumptions as APPENDIX C.

a) Cone action ($H_a < H_{ac}$)

H = actual penetration of sphere

H_a = apparent penetration of pseudo-cone

β_a = half angle of soil pseudo-cone = $\frac{\pi}{4} - \frac{\phi}{2}$

R = radius of sphere

Resisting force is equal to equation (41),

$$F = \pi c e^{Kl} (\tan\beta_a + \tan\phi) \tan\beta_a . H_a^2 \qquad (F1)$$

where

$$Kl = 2.3 \left(\frac{\beta_a}{\lambda} - \log \sigma_{\omega o}\right)$$

λ, $\sigma_{\omega o}$ = values from Figure 10 and 11 for perfectly rough surface.

b) Full cone action ($H_a = H_{ac}$)

The resisting force is

$$F = \pi c e^{Kl} (\tan\beta_a + \tan\phi) \tan\beta_a . H_{ac}^2 \qquad (F2)$$

where

$$H_{ac} = \frac{R \sin\left(\frac{\pi}{4} + \frac{\phi}{2}\right)}{\tan\beta_a}$$

c) Combined cone and sphere ($H_a > H_{ac}$)

The total resisting force is

$$F = F_c + F_s \tag{F3}$$

where

F_c = force on full cone and equal to equation (F2)

and

F_s = force on part of sphere which can be derived from equation (43) as

$$F_s = 2cR^2 e^{Kl} \int_0^{2\pi} \left[\int_\beta^{\beta a} e^{\frac{2.3\theta}{\lambda}} \cdot \sin\theta \cos\theta . d\theta + \tan\phi_s \int_\beta^{\beta a} e^{\frac{2.3\theta}{\lambda}} \cos^2\theta \, d\theta \right] d\rho \tag{F4}$$

The separation of integral terms is

$$\int_\beta^{\beta_a} e^{\frac{2.3\theta}{\lambda}} \cdot \sin\theta.\cos\theta.d\theta = \frac{1}{2\left[\left(\frac{2.3}{\lambda}\right)^2 + 4\right]} \cdot \left[e^{\frac{2.3\beta_a}{\lambda}} \left(\frac{2.3}{\lambda} \sin 2\beta_a - 2\cos 2\beta_a\right) - e^{\frac{2.3\beta}{\lambda}} \left(\frac{2.3}{\lambda} \sin 2\beta - 2\cos 2\beta\right) \right] \tag{F5}$$

$$\int_{\beta}^{\beta_a} e^{\frac{2.3\theta}{\lambda}} .\cos^2\theta d\theta = \frac{1}{\left[\left(\frac{2.3}{\lambda}\right)^2 + 4\right]} \cdot \left[e^{\frac{2.3\beta_a}{\lambda}} \left(\frac{2.3}{\lambda} \cos\beta_a + 2 \sin\beta_a\right) \cos\beta_a + \frac{2\lambda}{2.3} .e^{\frac{2.3\beta_a}{\lambda}} - e^{\frac{2.3\beta}{\lambda}} \left(\frac{2.3}{\lambda} \cos\beta + 2 \sin\beta\right) \cos\beta + \frac{2\lambda}{2.3} .e^{\frac{2.3\beta}{\lambda}} \right] \quad \text{(F6)}$$

Substituting equation (F5) and (F6) into (F4) yields

$$F_s = \frac{4\pi c R^2 e K1}{\left[\left(\frac{2.3}{\lambda}\right)^2 + 4\right]} \left[e^{\frac{2.3\beta_a}{\lambda}} \sin 2\beta_a \left(\frac{2.3}{\lambda} + \tan\phi_s\right) + \cos^2\beta_a \left(\frac{2.3}{\lambda} \tan\phi_s - 4\right) + 2 \right] - \left[e^{\frac{2.3\beta}{\lambda}} \left[\sin 2\beta \left(\frac{2.3}{\lambda} + \tan\phi_s\right) + \cos^2\beta \left(\frac{2.3}{\lambda} \tan\phi_s - 4\right) + 2 \right] \right] \quad \text{(F7)}$$

APPENDIX G: SAMPLE CALCULATION OF SOIL STRENGTH PARAMETERS FROM WEDGE AND CONE PENETRATIONS

a) Wedge data

The experimental data from penetrations of 90° and 60° wedge in modeling clay at 0.6 in. penetration are;

penetrating force on 90° wedge = 44.7 lb. per in.

penetrating force on 60° wedge = 21.7 lb. per in.

soil-steel friction angle = 10.5°

1. Calculate λ from equation (47)

$$\lambda = \frac{2.3\ (45 - 30)}{\ln\left[\frac{(\tan 30 + \tan 10.5).\ 44.7}{(\tan 45 + \tan 10.5).\ 21.7}\right]}$$

$$\lambda = 122.1°$$

2. Read off ϕ from Figure 12 for $\lambda = 122.1°$ and $\phi_s = 10.5°$

$$\phi = 24.4°$$

3. Read off $\sigma_{\omega o}$ from Figure 11 for $\phi_s = 10.5°$ and $\phi = 24.4°$

$$\sigma_{\omega o} = 4.60 \text{ psi}$$

4. Substitute $\phi_s = 10.5°$, $\lambda = 122.1°$, $\sigma_{\omega o} = 4.60$ psi in equation (45) and solve for c as;

$$c = \frac{44.7}{2x4.6x.6\ (\tan 45 + \tan 10.5).e^{2.3x45/122.1}}$$

$c = 2.93$ psi

b) Cone

According to the experimental data of Figure 34, the slopes of square root force vs. penetration for 60° and 30° cones are as follows;

cone slope index for 60° cone = 7.70 lb $\frac{1}{2}$ per in.

cone slope index for 30° cone = 3.59 lb $\frac{1}{2}$ per in.

The soil-steel friction angle is 10.5°.

1. Calculate λ from equation (48)

F_1 for 60° cone = $(7.70)^2$ = 59.29 lb.

F_2 for 30° cone = $(3.57)^2$ = 12.74 lb.

then

$$\lambda = \frac{2.3\ (30-15)}{\ln \left[\frac{\tan 15\ (\tan 15 + \tan 10.5)\ \times\ 59.29}{\tan 30\ (\tan 30 + \tan 10.5)\ \times\ 12.74}\right]}$$

$\lambda = 138.2°$

2. Read off ϕ from Figure 12 for $\lambda = 144.9°$ and $\phi_s = 10.5°$

$\phi = 20.5°$

3. Read off $\sigma_{\omega o}$ from Figure 11 for $\phi_s = 10.5°$ and $\phi = 20.5°$

$\sigma_{\omega o} = 4.25$ psi

4. Substitute $\phi_s = 10.5°$, $\lambda = 138.2°$, $\sigma_{\omega o} = 4.25$ psi in equation (41) and solve for c as;

$$c = \frac{59.29}{\pi \times 4.25\ (\tan 30 + \tan 10.5)\ \tan 30 \times e^{2.3 \times 30/138.2}}$$

$c = 3.59$ psi.